Organic Room-Temperature Phosphorescence Materials: from Fundamental Triplet Exciton Modulations to Novel Applications in Biosensing and Bioimaging

by

Yingying Zeng

A dissertation submitted in partial fulfillment
of the requirements for the degree of
Doctor of Philosophy
(Macromolecular Science and Engineering)
in the University of Michigan
2021

Doctoral Committee:

Professor Jinsang Kim, Chair
Professor Joerg Lahann,
Professor Adam Matzger
Assistant Professor Yannis M. Paulus

Yingying Zeng

yyzeng@umich.edu

ORCID iD: 0000-0003-1268-1870

Dedication

This dissertation is dedicated to the giants upon whose shoulders I have stood to push the light of science a little further against darkness.

Acknowledgements

First and foremost, I would like to thank my thesis advisor Professor Jinsang Kim who has been an incredible mentor to me throughout my graduate study at the University of Michigan. I am grateful for the intellectual freedom and autonomy he provided to help me grow as an independent scientist committed to conducting original research. I respect his passion for science and dedication to education a great deal. I would also like to express my sincere gratitude to my dissertation committee members Professor Joerg Lahann, Professor Adam Matzger, and Professor Yannis Paulus for their insightful discussion and invaluable advice for my dissertation projects.

I must thank my research collaborators Dr. Do Hyun Kang, Dr.Van Phuc Nguyen, and Dr. Jialiu Ma for their commitment and contribution to some of the work presented in this dissertation. They have enriched my knowledge base for the research topics we collaborated on and beyond.

My heartfelt appreciation also goes to Dr. Yasmine Doleyres, Professor Stephany Tzeng, and Dr. Xian Xu whose mentorship and friendship have motivated me through tough times.

Throughout my thesis research in the Kim lab, I have had distinct pleasure to work with a group of brilliant and motivated researchers. A big thank you to all the past and present labmates.

Additionally, I would like to show my appreciation to the supportive staff members at Biointerfaces Institute and Macromolecular Science and Engineering program coordinators Adam Mael and Julie Pollak.

Finally, I would like to thank Rackham Graduate School, College of Engineering, and Macro program for supporting me financially through Rackham International Student Fellowship, Barbour Scholarship, and Graduate Student Emergency Fund.

Table of Contents

List of Tables

List of Figures

Abstract

Metal-free purely organic phosphors are an emerging class of room-temperature phosphorescence (RTP) materials and have attracted great attention over the past decade, owning to their potentials in a variety of advanced photofunctional applications, including organic light emitting diodes (OLEDs), chemical sensing, bioimaging, phototheranostics, and digital security. Organic phosphorescence refers to photons emitted from triplet excited states (excitons), which is associated with spin-forbidden transitions. The weak spin-orbit coupling (SOC) due to the lack of heavy atoms in purely organic materials leads to long-lived triplet excitons that are highly susceptible to oxygen quenching and molecular vibration deactivation. Therefore, organic phosphorescence is typically only observed at cryogenic temperatures and under inert conditions. This presents both opportunities and challenges in triplet exciton utilization at room temperature.

The first part of this dissertation highlights the technologies we have developed leveraging the unique oxygen quenching aspect of organic RTP for *in vivo* tissue hypoxia imaging and *in vitro* phosphorimetric biodetection. Ischemia-induced hypoxia is a common complication associated with numerous retinopathies affecting more than 160 million people worldwide. Early detection and long-term visualization of retinal tissue hypoxia is essential to understand the pathophysiology and treatment of ischemic retinopathies, however, no effective solution exists to this problem. We have demonstrated a versatile lipid-polymer hybrid organic RTP nanoparticle (NP) platform that optically visualizes chorioretinal tissue hypoxia in real-time and with high signal-to-noise ratio. This represents the first non-destructive detection method. Additionally, we have extended the application of these organic RTP NPs to a highly sensitive phosphorimetric assay through the

integration with a signal-amplifying enzymatic oxygen scavenging reaction and a sandwich-DNA hybridization assay on 96-well plates. The phosphorimetric sensor demonstrates sequence-specific detection of a cell-free cancer biomarker with a 0.5 pM detection limit. By re-programming the detection probe, our methodology can be adapted to a broad range of biosensor applications for biomarkers of great clinical importance yet difficult to detect due to their low abundance *in vivo*.

In the second and third parts of this dissertation, we focus on fundamental studies of photophysical characteristics of triplet excitons and provide deeper insight into material design strategies for modulating triplet energy and accelerating light extraction more efficiently. Despite the controversial opinions on the matter of spin angular momentum conservation during energy transfer, we have shown efficient intermolecular triplet-to-singlet energy transfer (T-S ET) in purely organic luminescent materials through a pseudo-Förster resonance energy transfer pathway. The T-S ET process quenches the organic RTP emission from donor triplet excitons and sensitizes acceptor singlet excitons, which ultimately induces ambient delayed fluorescence, with the ET efficiency as high as 75.5%. Finally, we aim to address the weak SOC and molecular vibration issues simultaneously in a single material system—metal-organic framework (MOF). Organic phosphors are incorporated into highly ordered and rigid MOFs via coordination bonding to zirconium (Zr)- and hafnium (Hf)-metal clusters. The obtained MOFs are isostructural to UiO-67, and exhibit strong long-lived RTP and stable high-temperature phosphorescence (HTP) that persists up to 400K. The heavier UiO-67 (Hf) framework is found to be more effective than its Zr counterpart at suppressing molecular motions and facilitating phosphorescence emission. This work has identified critical material design parameters and structural basis for organic phosphorescence of high brightness and desirable stability, hence holds the promise to solve the long-standing efficiency roll-off issue in phosphorescence OLEDs.

Overall, this dissertation work serves to advance the fundamental understanding of triplet exciton behaviors and the technological innovation in their utilizations.

Chapter 1

Introduction

1.1 Organic Photoluminescence Transitions and Phosphorescence

Organic luminescence relates closely to the nature of the excited state (i.e., exciton) deactivation. According to the spin multiplicity of the excited state, organic luminescence can be classified into two basic forms: fluorescence and phosphorescence. Fluorescence refers to photon emission from radiative decay between two energy states of the same spin multiplicity (singlet exciton), whereas phosphorescence originates from the radiative decay between two states with different multiplicity (triplet exciton). In molecular spectroscopy, a Jablonski energy diagram[1] is widely used to illustrate a molecule's electronic states and all possible photophysical transitions between them (Figure 1.1). Generally, the ground state of organic materials is singlet (S_0), except for molecular oxygen with a triplet ground state.[2] Upon photoexcitation (absorption), the electrons in the molecule will be excited to high singlet excited states (S_n, $n \geq 1$) from S_0 following Franck-Condon principle. The high-lying S_n then immediately relaxes to the lowest single excited state (S_1) via rapid internal conversion (IC) according to Kasha's rule. From S_1, the electron can relax back to S_0 by emitting fluorescence, or transition to triplet excited states (T_n) via intersystem crossing (ISC) when such process is allowed and efficient enough. Through rapid IC from T_n, the lowest triplet excited state (T_1) will be generated, and its subsequent radiative decay to S_0 produces phosphorescence.

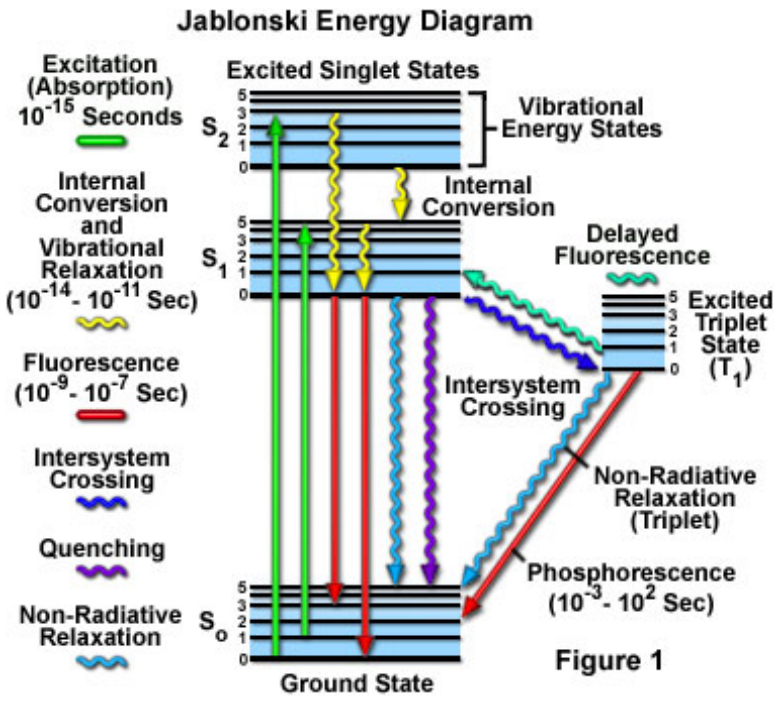

Figure 1.1 | Jablonski energy diagram illustrating transitions between electronic states for the quantum mechanical processes of fluorescence and phosphorescence. Non-radiative transitions are marked with squiggly arrows and radiative transitions by straight arrows. The vibrational ground states of each electronic state are indicated with thick lines and the higher ones with thinner lines. Adapted from reference 1.

It is important to note that there are various non-radiative relaxations that compete with fluorescence and phosphorescence emissions. One pathway can become dominant among others and manifests the net luminescent properties of the material. Therefore, it is crucial to understand the underlying quantum mechanics principles that govern these pathways so that the desired ones can be amplified through careful molecular design.

Fluorescence is a fast luminescence with a short lifetime on the order of ~10 ns due to the allowed transition from S_1 to S_0. By contrast, phosphorescence has much longer lifetime, typically in the milliseconds to seconds regime, in that it is associated with "forbidden" transitions in quantum mechanics: ISC from $S_1 \rightarrow T_1$ and radiative decay from $T_1 \rightarrow S_0$. To obtain bright phosphorescence at room temperature, both of the two key steps must be promoted.

1.2 Intersystem Crossing and Spin-Orbit Coupling[3]

ISC is an isoenergetic radiationless transition between singlet and triplet states, which requires flipping electron spin, and is forbidden by rules of angular momentum conservation. Consequently, ISC generally occurs on very long-time scales and is kinetically unfavorable among other fast photophysical transitions such as fluorescence and non-radiative relaxation.

Spin-orbit coupling (SOC) describes a weak magnetic interaction between the electron spin and the magnetic field induced by electrons orbiting around the nucleus. Strong SOC can facilitate the flip of electron spin and transitions between electronic states of different spin multiplicity become allowed. From the Jablonski diagram, to achieve phosphorescence with high quantum efficiency, the triplet excited state needs to be efficiently populated through ISC followed by radiative decay back to the singlet ground state. Both processes involve the change of electron spin. Therefore, enhancing SOC is one of the most critical strategies to be implemented in material design for strong phosphorescence. There are two key mechanisms to promote SOC in organic molecules: El-Sayed rule and heavy atom effect.

1.2.1 El-Sayed rule

El-Sayed rule[4] indicates that the rate of ISC is relatively fast if the transition involves a change in the orbital type. For example, a $^1(n,\pi^*)$ (singlet state) is allowed to transition to a $^3(\pi, \pi^*)$ (triplet state), but not to a $^3(n, \pi^*)$ state and vice versa (Figure 1.2a,b).[5,6] From the molecular structure perspective, ISC is expected to be remarkably fast in molecules with low-lying $^1n\pi^*$ states, where n represents the non-bonding electrons of N or O atom. In many N-heterocyclic aromatic hydrocarbons and carbonyl compounds, the $^1n\pi^*$ and $^3\pi\pi^*$ states are located in the same energy region, i.e., small ΔE_{st}, which is also favorable for high ISC rate (Figure 1.2c). Take

benzaldehyde for an instance, almost all of its $^1n\pi^*$ transit to triplet state and no fluorescence can be observed from isolated molecule. By contrast, ISC is generally inefficient in the $^1\pi\pi^*$ state (S_1) of aromatic hydrocarbons with no lone pair electrons.

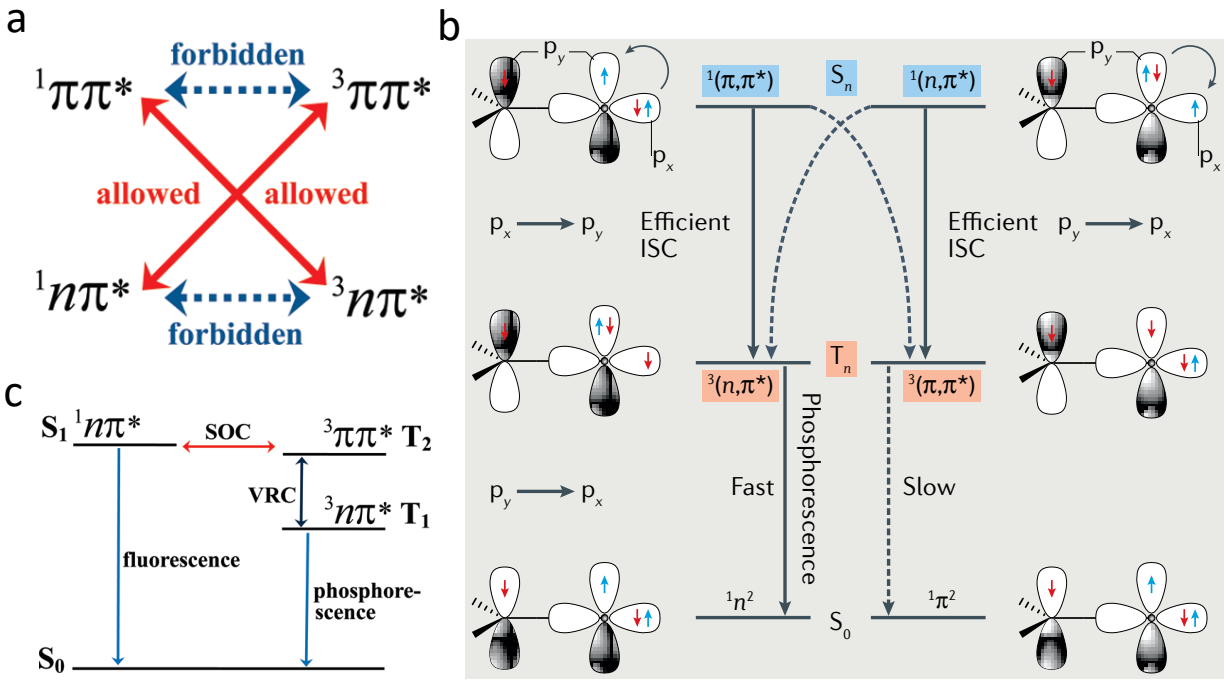

Figure 1.2 | El-Sayed rule for spin-orbit coupling. a,b, Effective ISC only occurs in transitions from $^1(n,\pi^*)$ to $^3(\pi,\pi^*)$ and $^1(\pi,\pi^*)$ to $^3(n,\pi^*)$, in which the molecular transition orbitals p_x and p_y effectively overlap under SOC. By contrast, the ISC from $^1(\pi,\pi^*)$ to $^3(\pi,\pi^*)$ or from $^1(n,\pi^*)$ to $^3(n,\pi^*)$ is not favored because the SOC is inefficient, with poor orbital overlap. **c**, Coupling scheme for ISC in the nπ* singlet state. Adapted from reference 5 and 6.

1.2.2 Heavy atom effect

SOC arises from the special theory of relativity. Electrons orbiting around a heavy nucleus can generate strong magnetic fields because the 1s electrons in elements of high atomic numbers can orbit nearly as fast as the speed of light. Simply put, heavy atoms can lead to SOC enhancement. Traditionally, heavy metals such as Iridium (Ir) and Platinum (Pt) in organometallic complexes are highly effective in enhancing SOC and promoting ISC, with phosphorescence

lifetimes in the lower end of microsecond regime.[3,7-9] Halogens such as bromine (Br) and iodine (I), and chalcogens such as selenium (Se) are well-known heavy atoms in bright organic phosphorescent molecules with lifetimes in the millisecond regime.[10-16] Heavy atom effect can be internal or external depending on whether the heavy atom is a part of the emitting center of the luminescent molecule.

1.3 Non-Radiative Deactivation by Molecular Motions

As discussed in section 1.1, organic phosphorescence is associated with "forbidden" processes in quantum mechanics and is a slow luminescence with relatively long lifetime in the range of 10^{-3} to 10^{2} s. Due to such slow, kinetically unfavored radiative transitions, other non-radiative deactivations may dominate the main relaxation processes of triplet excitons, leading to low phosphorescence quantum yield at room temperature.

The two major non-radiative relaxation pathways must be taken into account during molecular design is intramolecular vibration and intermolecular collisional quenching.[17,18] Both of them are significantly influenced by the rigidity of the components in the organic phosphorescent material system. Hirata *et al.* systematically studied the relationship between molecular structure of organic phosphor and intramolecular vibrational decay of triplet exciton (Figure 1.3).[17] Heavier substituents around the aromatic core (deuteration) reduces the vibration frequency f_v, resulting in more efficient persistent room-temperature phosphorescence (RTP).

Kwon *et al.* investigated in great detail the correlation between the nonradiative relaxation pathways and the rigidity of the organic phosphor as well as its proximate environment.[18] They reported a general design principle that involves covalently crosslinking between metal-free organic phosphors and polymer matrices to effectively suppress molecular motions and achieve

highly efficient RTP (Figure 1.4). The phosphorescence efficiency (Φ_p) of such system was 2~5 folds higher than that of phosphor-doped polymer films without covalent linkages.

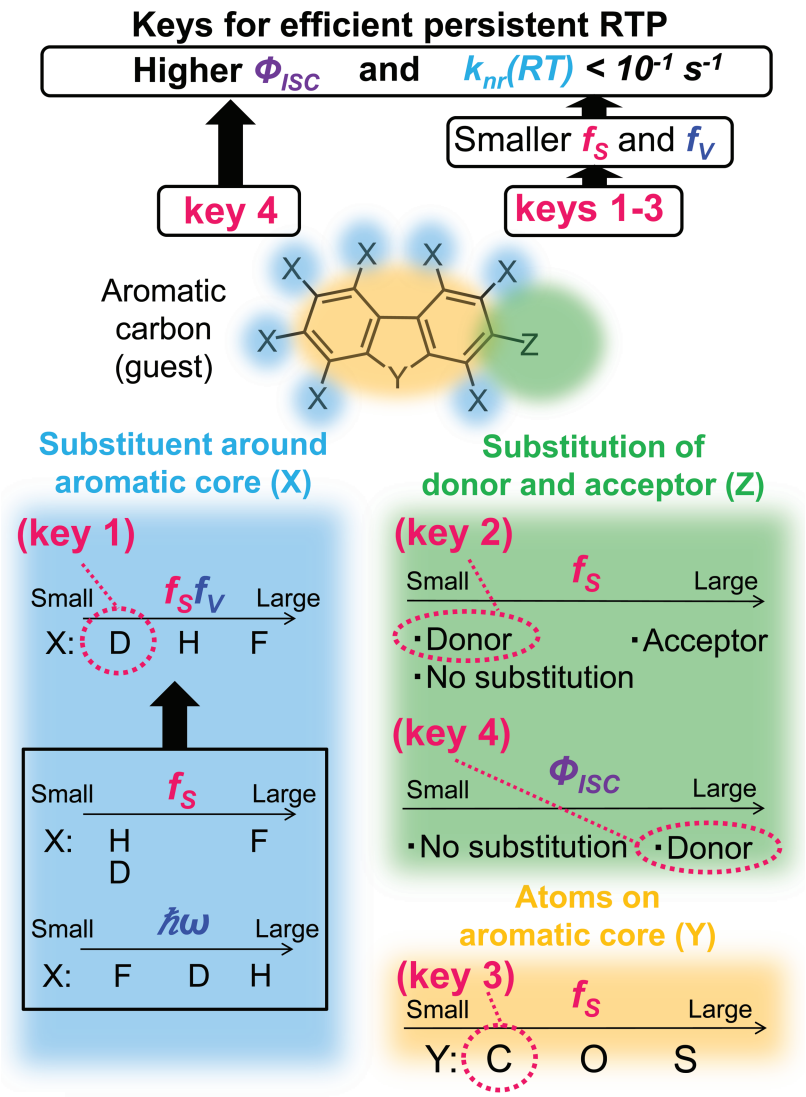

Figure 1.3 | Molecular design of an organic molecule for efficient persistent room-temperature phosphorescence. Keys 1 to 4 are the design elements lead to efficient persistent room-temperature phosphorescence. *f*s stands for spin configuration change and is unity for the transition between states with the same multiplicity. f_v is the vibration frequency. Adapter from reference 17.

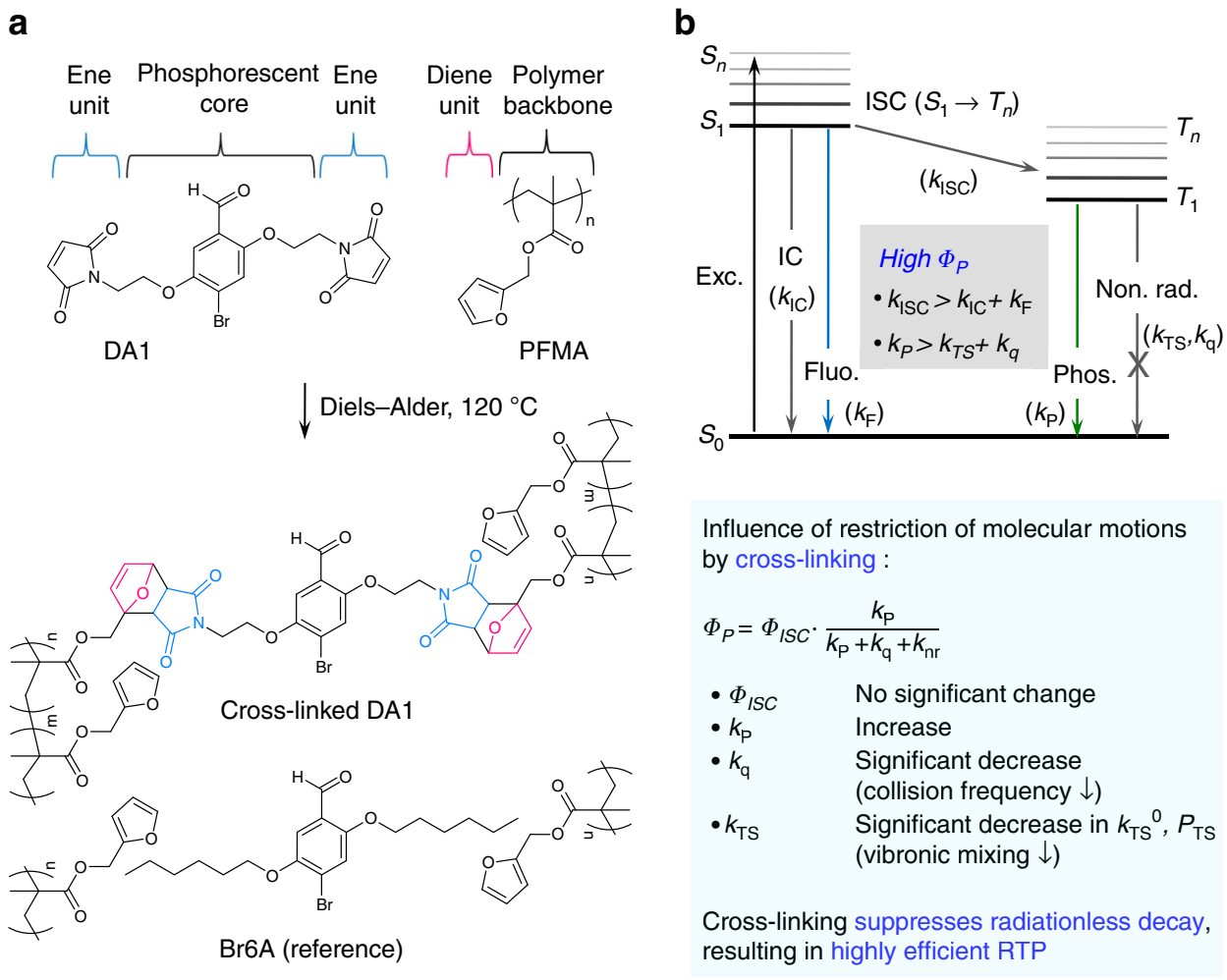

Figure 1.4 | Chemical structures of designed phosphor and polymer and description of covalent cross-linking strategy. a, Chemical structures of the designed phosphor and polymer with functional groups for Diels-Alder click chemistry. **b,** A general Jablonski diagram showing the influence of molecular motion restriction by covalent-crosslinking strategy. Adapted from reference 18.

It also should be noted that temperature significantly affects both intra- and intermolecular vibration. At high temperatures, such vibrations are more prominent. This is why conventionally metal-free organic molecules that strongly phosphoresce at low temperature such as 77K have no detectable phosphorescence at room temperature.

1.4 Phosphorescence Quenching by Oxygen

Organic phosphorescence signal from the long-lived triplet exciton is highly susceptible to quenching by molecular oxygen through triplet energy transfer (Figure 1.5).[19-24] The ground state of most molecules are singlet because two electrons in the same highest occupied molecular orbital (HOMO) are antisymmetric due to Pauli exclusion principle. However, molecular oxygen is a rare exception in that it has two degenerate HOMOs (Figure 1.5a) filled with two electrons with the same spin according to Hund's rule. Therefore, the ground state of molecular oxygen is triplet.

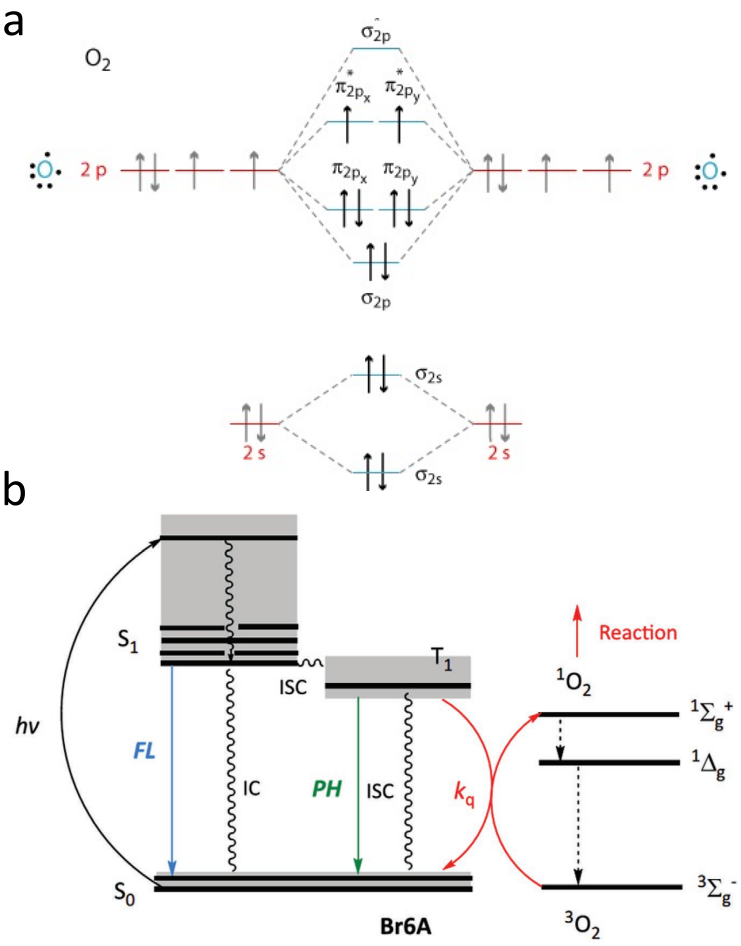

Figure 1.5 | Possible mechanism of phosphorescence quenching by molecular oxygen. a, ground state electron configuration and spin multiplicity of molecular oxygen. **b,** oxygen quenching of organic phosphorescence of Br6A via triplet energy transfer. Adapted from reference 23.

1.5 Recent Advances in Room-Temperature Organic Phosphorescence Materials

1.5.1 Crystal engineering

In the crystalline state, the molecular motions are restricted by the crystal lattices and intermolecular interactions such as hydrogen bonding and halogen bonding. Thereby, the organic luminogens are firmly locked and their conformations are rigidified. Crystallization can also protect triplet states from oxygen quenching and collisional quenching. Yuan *et al.*[12] first reported efficient crystallization-induced phosphorescence (CIP) from benzophenone and its derivatives under ambient conditions. It is important to note that these luminogens are non-phosphorescent when they are in good solvents, adsorbed on TLC plates, or doped into polymer films. Bolton *et al.*[10] also designed a bright green phosphor Br6A (Φ_{ph} ~3%) containing triplet-promoting aromatic aldehyde, heavy atom bromine, and crystalline state halogen bonding (Figure 1.6). One drawback of the dense crystal packing is aggregation-caused quenching. However, this was overcome by dilution via co-crystallization. When Br6A was doped into the crystal of Br6, the quantum yield was increased to 55%.

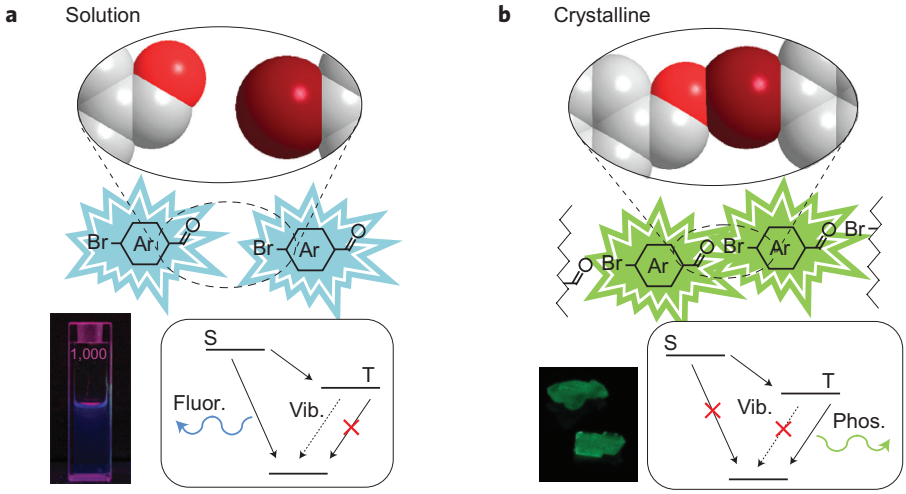

Figure 1.6 | Crystallization-induced efficient room-temperature phosphorescence. a, In solution (disordered state), halogenated aromatic aldehydes produce fluorescence emission. **b,** In the crystalline form, halogen bonding promotes triplet formation, and vibrational motions are limited by tight packing, allowing triplets to decay radiatively. Adapted from reference 10.

Lately, significant progress has been made in achieving persistent or ultralong RTP with lifetimes up to 10^2 seconds. An *et al.*[25] presented a general design strategy used to prolong the emission lifetime of a wide range of luminescent organic molecules up to 1.35 s. Triplet states were effectively stabilized through strong intermolecular electron coupling in H-aggregated molecules. They further integrated this approach with polymeric nanoparticle formulation and developed water-soluble organic nanoparticles for *in vivo* afterglow imaging (Figure 1.7).[26] However, quantum yields of these systems were low (Φ_{ph} < 10%) due to weak SOC and aggregation-caused quenching. Fateminia *et al.*[27] developed a new design strategy to realize bright red persistent RTP (Φ_{ph} ~11%) in nanocrystals. H-aggregation enhancement moiety was incorporated to facilitate persistent RTP. The nanocrystals were directly applied for the imaging of breast cancer cells, showing efficient cellular uptake and bright phosphorescence emission.

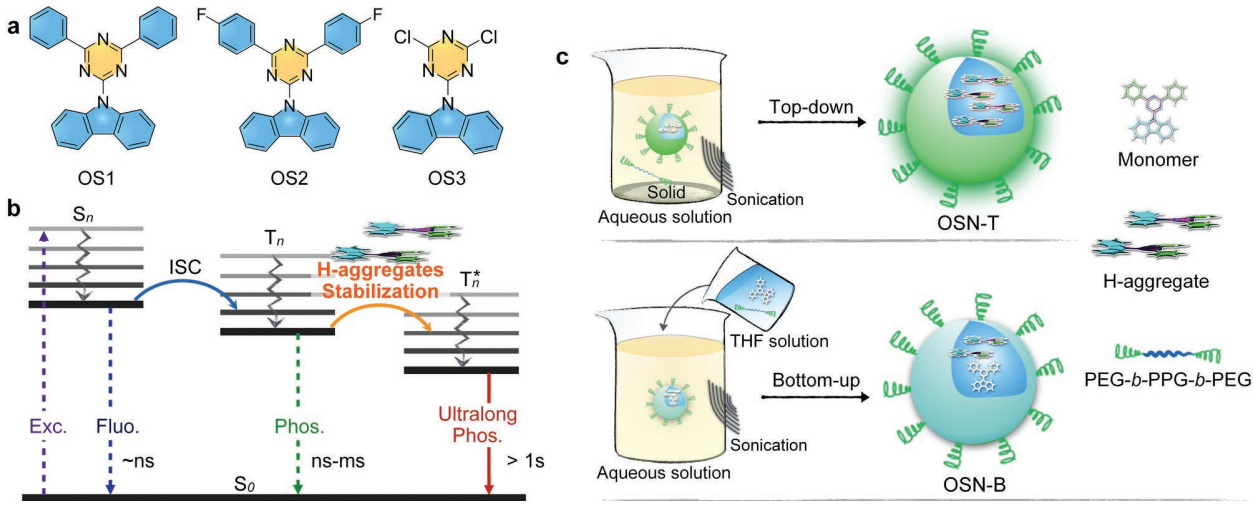

Figure 1.7 | H-aggregation in nanocrystals prolongs phosphorescence emission lifetime. a, Chemical structures of organic phosphors. **b,** Proposed mechanism for ultralong phosphorescence based on H-aggregates formation. **c,** Top-down and bottom-up routes for organic phosphor-encapsulated nanoparticles formulation. Adapted from reference 25.

More recently, Cheng *et al.*[28] reported ultralong RTP from rigid organic ionic crystals formed by terephthalic acid and $NH4^+$, Na^+, or K^+ (Figure 1.8). The emission color can be readily tuned from yellow green to sky blue by using these three different cations. The lifetime of phosphorescence was ultralong (~500 ms) due to H-aggregation.

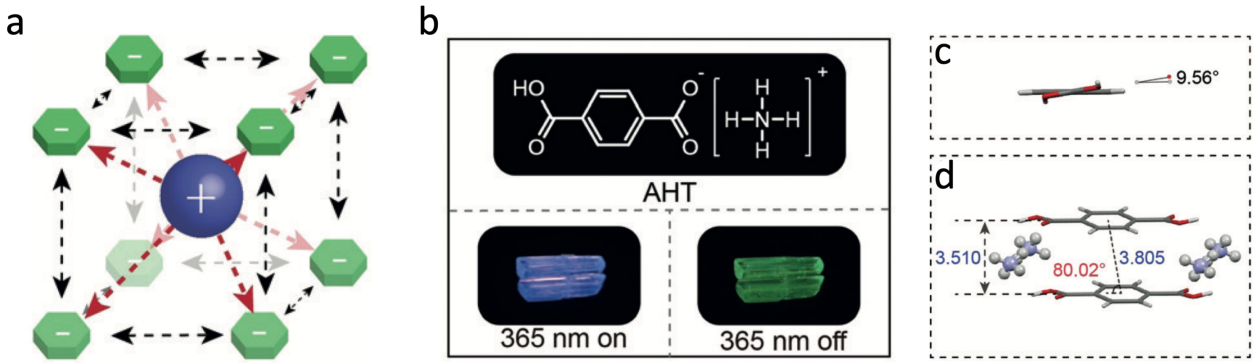

Figure 1.8 | H-aggregates in organic ionic crystals facilitate ultralong (persistent) room-temperature phosphorescence. a, Schematic illustration of organic ionic crystal. **b,** Chemical structure and photographs of ammonium hydrogen terephthalate (AHT) crystal before and after the irradiation with a 365 nm UV lamp was removed. **c,** Illustration of the torsion angle between the carboxyl group and benzene. **d,** Molecular packing in dimer. Adapted from reference 28.

1.5.2 Host-guest amorphous film

Although it is theoretically feasible to minimize the non-radiative deactivation of organic phosphors by doping them into rigid host molecules, it is experimentally challenging to develop such host-guest material systems containing both highly emissive phosphorescent guests and effective hosts capable of restricting molecular motions as well as blocking humidity and oxygen simultaneously. Multiple design criteria must be met. First, the organic phosphor needs to be highly compatible with the host for excellent dispersion within the host matrix; second, the host materials must be optically and chemically inert for both photoexcitation and luminescence extraction; third, host molecules should have higher T_1 and S_1 energy levels than that of the guest phosphors to prevent the luminescence quenching by energy transfer from the guest to the host.

When used in organic light-emitting diode (OLED), there are additional requirements such as host being electronically active for charge injection and transport to the guest emitters via electronic excitation.

Hirata *et al.*[17] successfully developed a purely organic amorphous host-guest system with efficient persistent RTP under ambient condition. The concept involved a design of a secondary amino-substituted deuterated aromatic hydrocarbon guest surrounded by a rigid host with short π conjugation (thus high T_1 energy level), amorphous hydroxy steroid (Figure 1.9). Deuteration of the guest slows down its non-radiative decay rate while the amino group promotes ISC for abundant T_1 population. Moreover, hydroxy steroid provides excellent oxygen barrier. As a result, efficient red-green-blue (RGB) persistent RTP with remarkable afterglow performance (lifetime > 1 s; Φ_{ph} > 10%) was obtained.

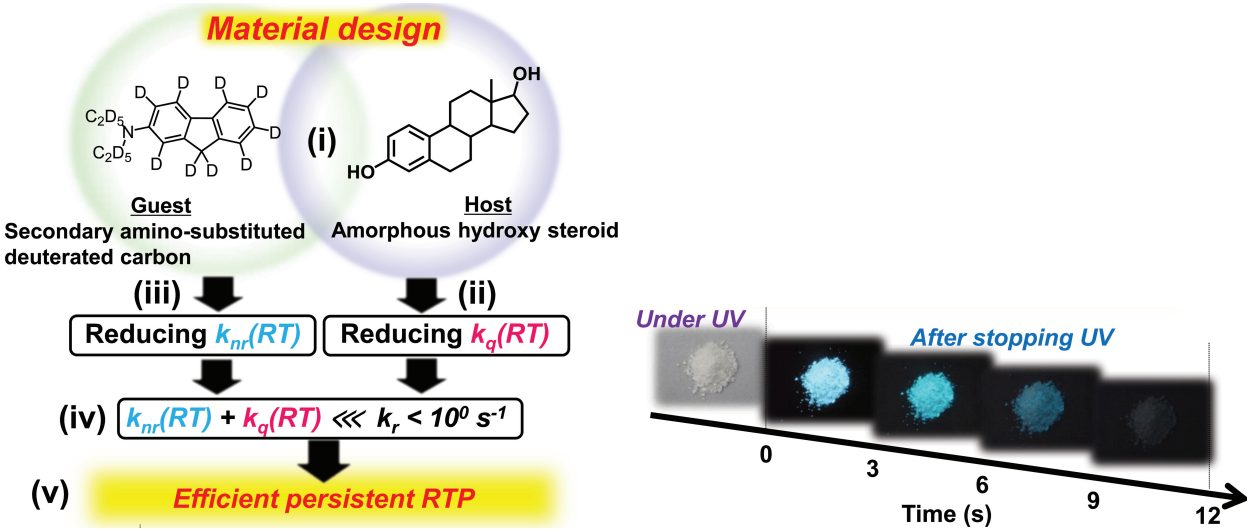

Figure 1.9 | Host-guest amorphous design for efficient persistent room-temperature phosphorescence. Adapted from reference 17.

Following this material design principle, the authors further demonstrated a three-component co-guest system, where two types of guests were dispersed in the amorphous hydroxy

steroidal host.[29] One guest is the organic phosphor also served as an acceptor while the other is an organometallic complex functioned as a triplet donor to populate the T_1 state of the acceptor via photosensitization. The phosphorescence lifetime reached 2.77s with a total quantum yield of 44%. Other host materials such as androstene derivatives have also been developed and showed promising performance for electronic device applications.[30]

Transparent amorphous glassy polymers (high glass transition temperature) can also effectively rigidify guest organic phosphors embedded within and thus suppress non-radiative decay pathways at room temperature. Besides, some polymers have low oxygen and moisture permeability. Depending on the applications, polymers as host materials can provide versatile functionalities. Lee *et al.*[31] reported bright RTP (Φ_{ph} 7.5%) by embedding the previously discovered metal-free organic phosphor Br6A[10] into poly(methyl methacrylate) (PMMA). Later, Kwon *et al.*[32] further minimized both the diffusion motion of the matrix polyvinyl alcohol (PVA) and the vibration of the guest phosphor G1 by introducing the intermolecular hydrogen-bonding between them (Figure 1.10). The G1-PVA80 film achieved a quantum yield of 13%, which is much higher than that of the Br6A-doped counterpart (Br6A is incapable of forming hydrogen bonds), suggesting the important role of such strong non-covalent interactions. By using PVA100, which has more hydrogen-bonding sites than PVA80, quantum yield reached up to 24% in G1-PVA100 films.

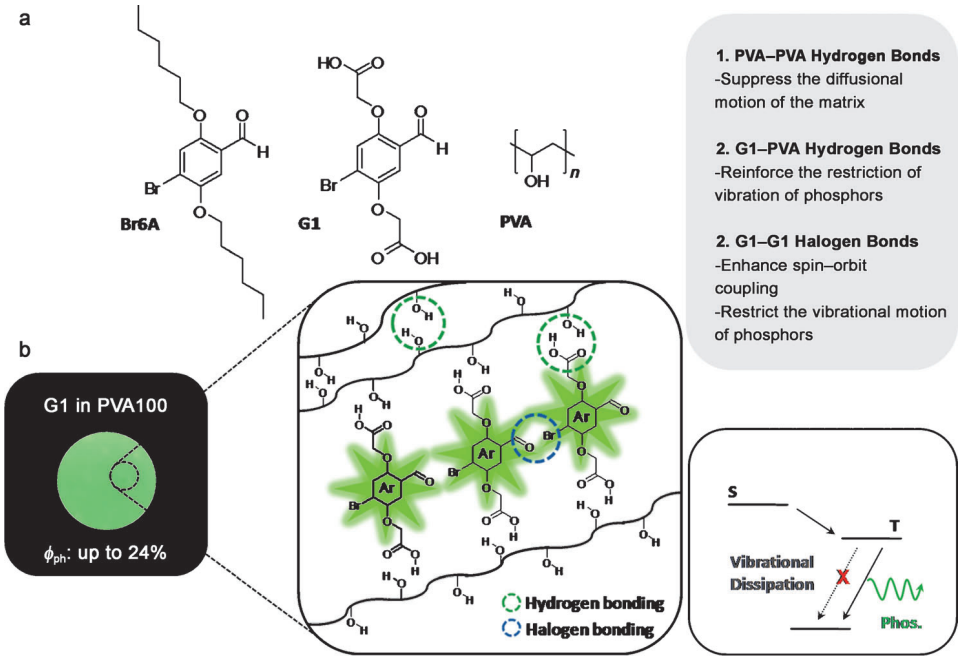

Figure 1.10 | Hydrogen bonding between organic phosphor guest and polymer matrix host enhances phosphorescence quantum efficiency. a, Chemical structures of Br6A, G1 and PVA. **b,** Schematic illustration of phosphorescence processes in the G1-PVA composite and system design rationale. On the left is a phosphorescence image of G1 embedded in PVA100 under UV 365 nm. Adapted from reference 32.

The interaction between the guest phosphor and the host polymer was further strengthened by covalent crosslinking between them via Diels-Alder click chemistry (Figure 1.4).[18] Highly efficient green RTP was demonstrated with quantum efficiency enhanced up to 28%. Following a similar strategy, a water-dispersible core-shell polymeric nanoparticle system with the organic phosphor C1 crosslinked within the core via reversible addition-fragmentation chain-transfer (RAFT) dispersion polymerization was developed (Figure 1.11).[24] Polymethyloxazoline was selected as the outer shell for good water dispersity and polystyrene as the core for its oxygen permeability. The resulting nanoparticles showed very high sensitivity for optical detection of dissolved oxygen (DO), with a detection limit of 60 nM. Such nanoparticle system can function as a novel versatile platform for sensitive oxygen quantification in both aqueous as well as gaseous

environment. When crosslinked with PMMA, C1-PMMA film exhibited phosphorescence quantum efficiency as high as 40%.

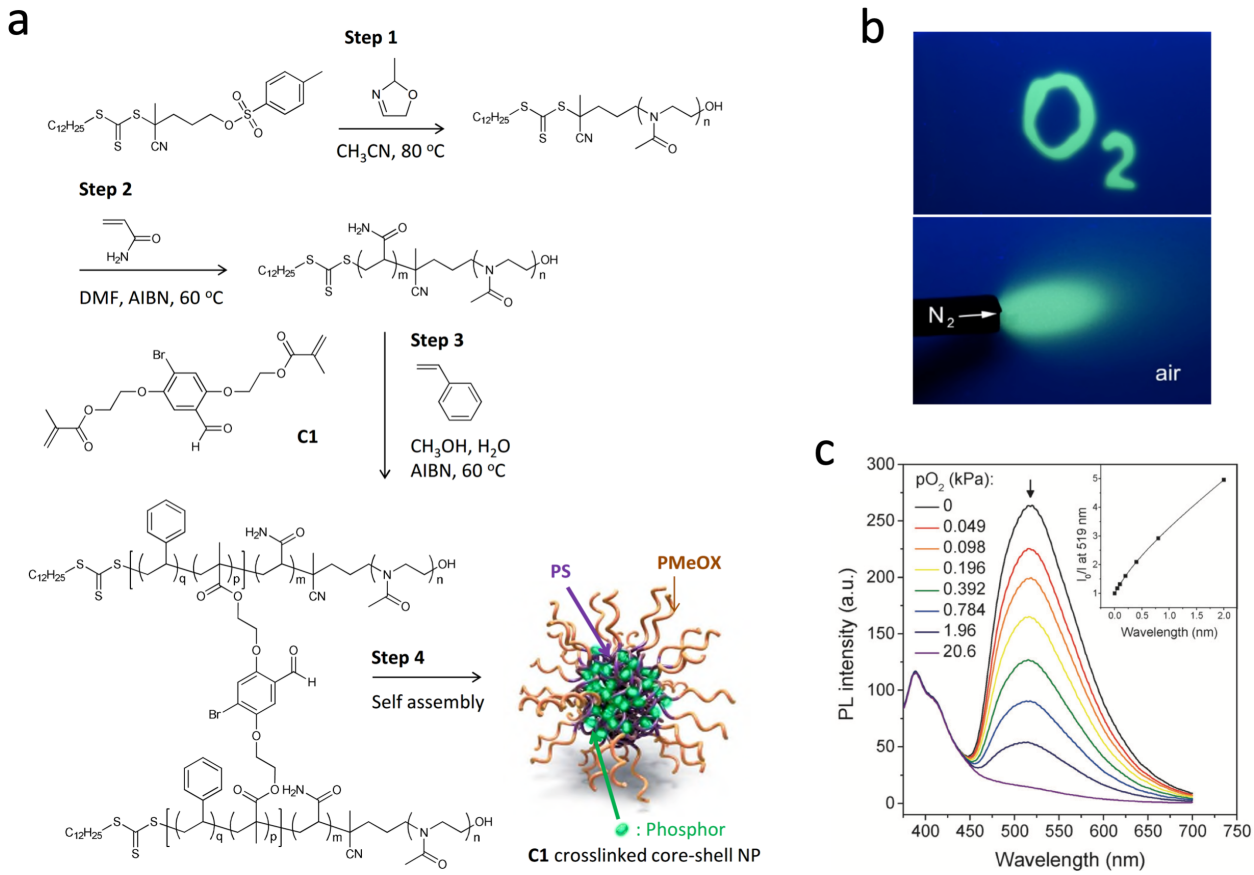

Figure 1.11 | Covalent crosslinking between guest phosphor and host polymer in nanoparticles produces bright organic room-temperature phosphorescence for oxygen-sensing. a, Synthetic routes of C1-crosslinked nanoparticles (NPs). **b,** Photographic images obtained of the planar optical sensor upon UV 365 nm illumination. Top: green phosphorescence area was soaked with an anoxic aqueous solution containing 5 wt% of glucose and 0.05 wt% of glucose oxidase. Bottom: deoxygenated with a flow of nitrogen. **c,** Luminescence spectra for the sensor upon exposure to various oxygen tensions. Adapted from reference 24.

1.5.3 Metal-organic frameworks

Metal-organic frameworks (MOFs) are metal-organic ligand hybrid materials, which have three-dimensional periodic structures. The material is known for its high porosity and large surface areas.[33-37] Tuning fluorescence color and quantum yield by rigidifying the fluorophore as organic

ligand linker of a robust MOF was reported by Wei *et al.*[38] A new tetraphenylethylene-based zirconium MOF (PCN-94) exhibited a deep-blue fluorescent emission at 470 nm with a unity quantum yield (ca. 99%) under argon at room temperature in the solid state (Figure 1.12). Compared to the yellow fluorescent linker precursor, PCN-94 blue shifted ca. 3600 cm^{-1} and doubled radiative decay efficiency. The high quantum yield is attributed to the reduced intra- and intermolecular interactions by framework rigidity.

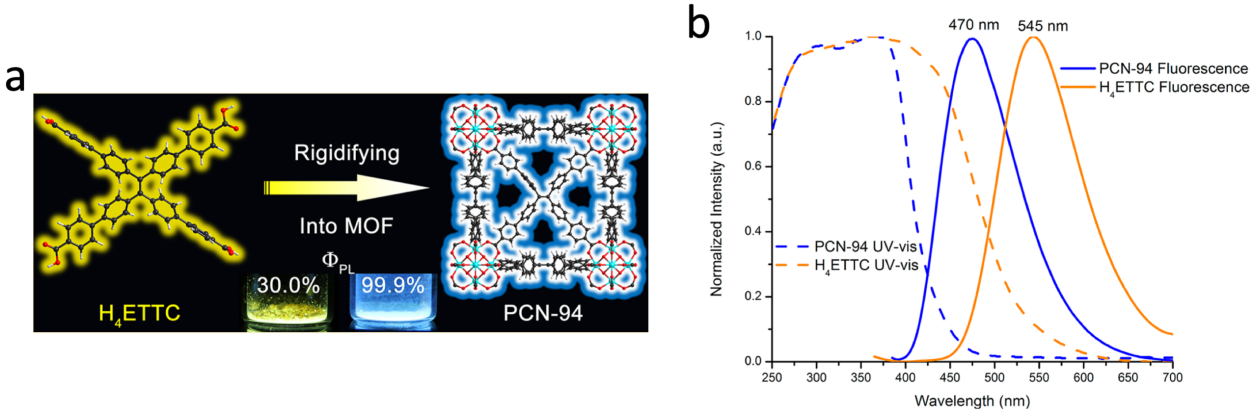

Figure 1.12 | Rigidifying effect of metal-organic framework on the incorporated fluorophore. **a,** Schematic illustration of rigidifying the fluorophore (H4ETTC) into MOF and photographic images of H2ETTC and PCN-94 under UV light respectively. **b,** Solid-state absorption and emission spectra. Adapted from reference 38.

This work demonstrated that MOF formation can produce significant effect on photophysical properties of the organic linker, which represented a new design strategy for constructing luminescent MOFs for potential applications in device and sensor. However, systems utilizing MOF platform to modulate the RTP behavior of organic luminogens have rarely been thoroughly investigated. The first example of MOFs with RTP was developed by Yang *et al.*[39] by coordinating terephthalic acid (TPA), isophthalic acid (IPA), and trimesic acid (TMA) with Zn^{2+} and Cd^{2+}. Among which, Zn-TPA showed a Φ_{ph} value of 3.4% with phosphorescence lifetime of 475 ms, a great enhancement in both features compared to the pristine TPA crystal with Φ_{ph} of

0.5% and lifetime of 2.7 ms (Figure 1.13); Interestingly, Zn-IPA displayed the longest lifetime of 1.3 s.

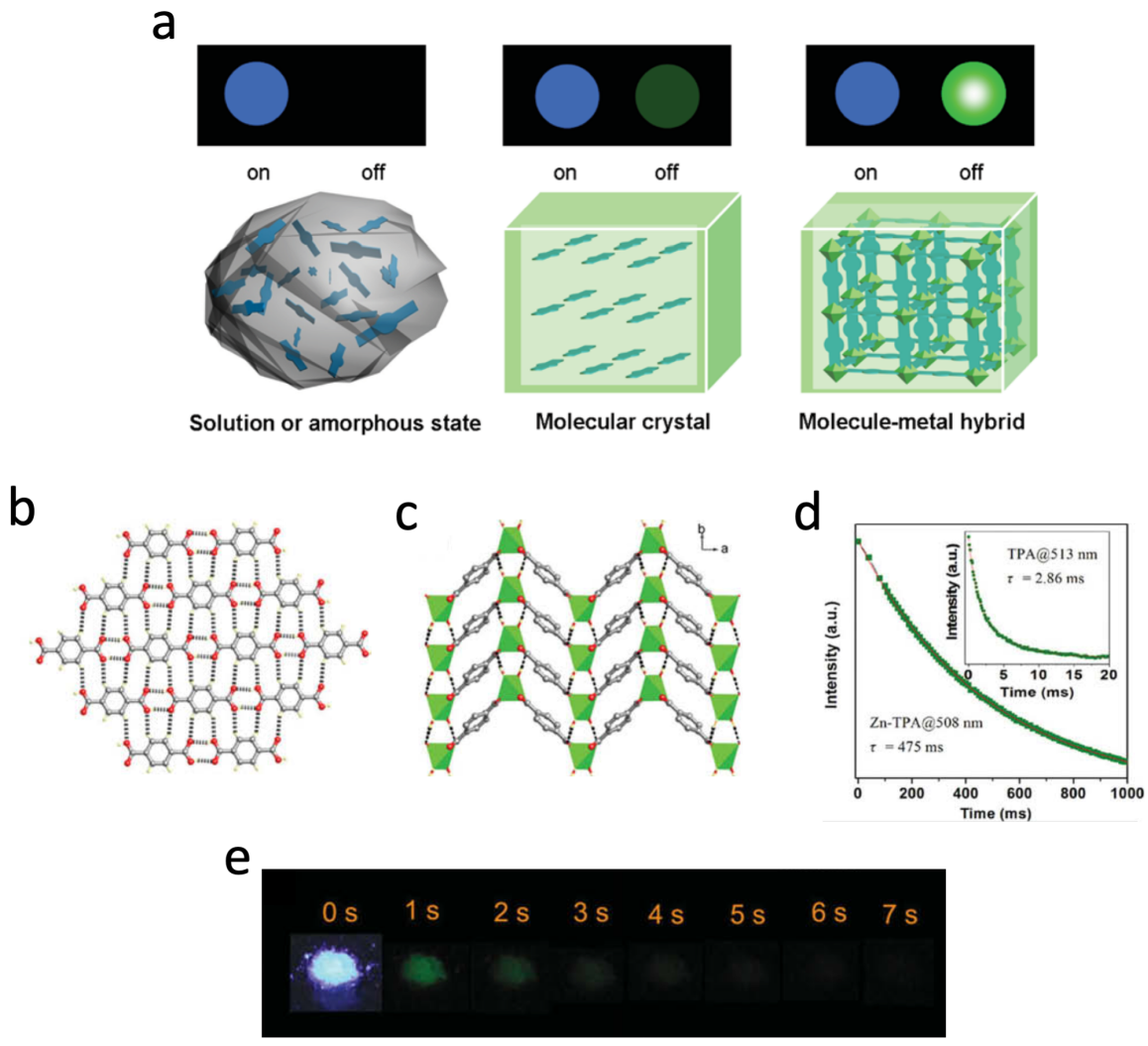

Figure 1.13 | Persistent room-temperature phosphorescence via coordination into MOF. a, Schematic representation of persistent RTP (before and after turning off the excitation) within molecule-metal hybrid compared with crystalline, amorphous and solution states of molecular systems. **b,c,** Crystal structures of TPA (**b**) and Zn-TPA (**c**). **d,** phosphorescence decay curves of TPA and Zn-TPA. **e,** photographs of Zn-TPA taken at different time intervals before and after turning off the excitation source (365 nm) under ambient condition. Adapted from reference 39.

The influence of metal ions on the RTP performance was further investigated by comparing the Zn (II)-based MOFs to Cd (II)-based ones. The corresponding lifetimes were relative shorter for Cd-MOFs than those of Zn counterparts. Moreover, RTP emissions were shifted as well, likely

due to different spatial arrangements of the organic ligands. As a result, it is unclear whether heavy atom effect from transition metals is involved in this material system since the crystal architecture changed simultaneously when the metal ions changed. In a follow-up study,[40] the authors prepared dynamic MOFs (Zn-TPA-DMF and MOF-5) that can reversibly change structures and colors upon solvation or guest adsorption.

MOFs can also be used as rigid host matrices to encapsulate guest organic molecules in their pores and to suppress non-radiative decay processes for RTP generation.[41] Zeolite imidazolate framework ZIF-8 was selected as the host for its relatively small pore diameter (1.16 nm) among all MOFs, which is close to the molecular size of the guest coronene (1.17 nm) (Figure 1.14). Besides, the small aperture size (0.34 nm) of ZIF-8 would effectively trap coronenes within. A phosphorescence quantum yield of about 1.8% with lifetime of 7.4 s was observed at room temperature. It is important to note that the deuterated coronene guest still exhibited long-lived emission with a lifetime of 400 ms even at 460K. The remarkable thermal stability of persistent phosphorescence and chemical stability of MOFs imply the great potential of organic phosphorescent materials coupled with MOF structures in a wide range of applications.

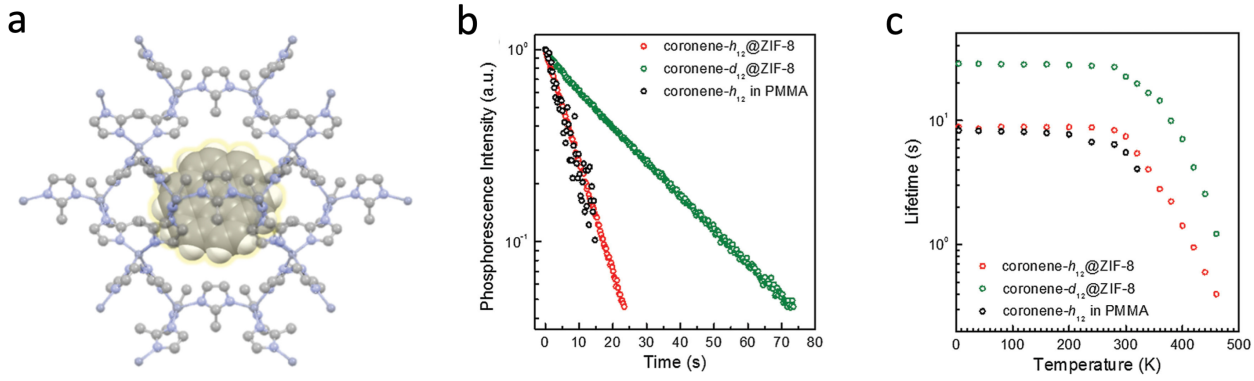

Figure 1.14 | Persistent and high-temperature phosphorescence via encapsulation into MOF pores. a, Structure of coronene@ZIF-8. **b,c,** Phosphorescence decay profiles (**b**) and temperature-dependent phosphorescence lifetime (**c**) of coronene doped into PMMA, coronene-h12@ZIF-8, and coronene-d12@ZIF-8, respectively. Adapted from reference 41.

In summary, despite the progress made in developing organic materials with RTP, most of the focus to date has been largely centered on suppressing adversary factors such as molecular rotations and vibrations. Though these strategies can effectively extend the phosphorescence lifetime, very few metal-free organic material systems have the desirable brightness for practical applications, i.e., low quantum efficiency at room or elevated temperatures. This is inherently originated from the weak SOC and low ISC rate between singlet and triplet states in the purely organic materials. In this perspective, to improve the performance of organic RTP materials, it is of great importance to systematically investigate the enhancement of SOC especially through heavy atom effect.

1.6 Dissertation Outline

The dissertation work covers both the fundamental and applied aspects of triplet excitons in purely organic RTP molecules. The first section (Chapter 2 and 3) builds upon previous work and leverages triplet energy quenching by molecular oxygen for biosensing applications. A versatile oxygen-sensing platform technology based on lipid-polymer hybrid core-shell organic room-temperature phosphorescence (RTP) nanoparticles (NPs) is developed and applied toward *in vivo* tissue hypoxia imaging and *in vitro* phosphorimetric biodetection. Chapter 2 describes that these organic RTP NPs effectively detects chorioretinal tissue hypoxia in clinically relevant living animal models in real-time and with high signal-to-noise ratio. Chapter 3 reports the integration of organic RTP-based biosensor with a sandwich-DNA hybridization assay on 96-well plates for highly sensitive and quantitative detection of cell-free nucleic acids.

The second (Chapter 4) and third (Chapter 5) sections focus on fundamental characteristics of triplet excitons and interactions between electronic states of different multiplicity, and yielded

rational material design strategies to modulate triplet excitons and harvest triplet energy more efficiently. Chapter 4 details an efficient intermolecular triplet-to-singlet energy transfer process in purely organic luminescent materials through a pseudo-Förster resonance energy transfer (pseudo-FRET) mechanism, challenging the notion of spin angular momentum conservation observed in conventional energy transfer pathways. Chapter 5 aims to address the weak SOC and molecular vibration issues simultaneously by coordinating organic phosphors with zirconium and hafnium metal clusters in a rigid metal-organic framework. Phosphorescence properties of obtained MOFs are examined. Future research directions are outlined at the end of each technical chapter. Finally, Chapter 6 provides a summary of key research findings and contributions, as well as a comprehensive outlook of organic phosphorescence field.

1.7 References

1. Jablonski energy diagram. https://www.olympus-lifescience.com/en/microscope-resource/primer/java/jablonski/jabintro/.
2. Turro, N. J.; Ramamurthy, V.; Scaiano, J. C. *Modern molecular photochemistry of organic molecules*. University Science Books: Sausalito, Calif., 2010; p xxxiii, 1084 p.
3. Marian, C. M. Spin-orbit coupling and intersystem crossing in molecules. *Wiley Interdisciplinary Reviews: Computational Molecular Science* **2012,** *2* (2), 187-203.
4. El-Sayed, M. A. Spin—orbit coupling and the radiationless processes in nitrogen heterocyclics. *The Journal of Chemical Physics* **1963,** *38* (12), 2834-2838.
5. Baba, M. Intersystem crossing in the 1npi* and 1pipi* states. *J Phys Chem A* **2011,** *115* (34), 9514-9.
6. Zhao, W.; He, Z.; Tang, B. Z. Room-temperature phosphorescence from organic aggregates. *Nat. Rev. Mater.* **2020**.
7. Hofbeck, T.; Yersin, H. The triplet state of fac-ir(ppy)3. *Inorg. Chem.* **2010,** *49* (20), 9290-9.
8. Baldo, M. A.; O'Brien, D. F.; You, Y.; Shoustikov, A.; Sibley, S.; Thompson, M. E.; Forrest, S. R. Highly efficient phosphorescent emission from organic electroluminescent devices. *Nature* **1998,** *395* (6698), 151-154.

9. Adachi, C.; Baldo, M. A.; Thompson, M. E.; Forrest, S. R. Nearly 100% internal phosphorescence efficiency in an organic light-emitting device. *J. Appl. Phys.* **2001,** *90* (10), 5048-5051.

10. Bolton, O.; Lee, K.; Kim, H. J.; Lin, K. Y.; Kim, J. Activating efficient phosphorescence from purely organic materials by crystal design. *Nat. Chem.* **2011,** *3* (3), 205-10.

11. Lee, D. R.; Lee, K. H.; Shao, W.; Kim, C. L.; Kim, J.; Lee, J. Y. Heavy atom effect of selenium for metal-free phosphorescent light-emitting diodes. *Chem. Mater.* **2020,** *32* (6), 2583-2592.

12. Yuan, W. Z.; Shen, X. Y.; Zhao, H.; Lam, J. W. Y.; Tang, L.; Lu, P.; Wang, C. L.; Liu, Y.; Wang, Z. M.; Zheng, Q.; Sun, J. Z.; Ma, Y. G.; Tang, B. Z. Crystallization-induced phosphorescence of pure organic luminogens at room temperature. *J Phys Chem C* **2010,** *114* (13), 6090-6099.

13. Wang, J.; Gu, X.; Ma, H.; Peng, Q.; Huang, X.; Zheng, X.; Sung, S. H. P.; Shan, G.; Lam, J. W. Y.; Shuai, Z.; Tang, B. Z. A facile strategy for realizing room temperature phosphorescence and single molecule white light emission. *Nat. Commun.* **2018,** *9* (1), 2963.

14. Yang, Z.; Xu, C.; Li, W.; Mao, Z.; Ge, X.; Huang, Q.; Deng, H.; Zhao, J.; Gu, F. L.; Zhang, Y.; Chi, Z. Boosting the quantum efficiency of ultralong organic phosphorescence up to 52 % via intramolecular halogen bonding. *Angew. Chem. Int. Ed.* **2020,** *59* (40), 17451-17455.

15. Xu, L.; Li, G.; Xu, T.; Zhang, W.; Zhang, S.; Yin, S.; An, Z.; He, G. Chalcogen atom modulated persistent room-temperature phosphorescence through intramolecular electronic coupling. *Chem. Commun.* **2018,** *54* (66), 9226-9229.

16. She, P.; Yu, Y.; Qin, Y.; Zhang, Y.; Li, F.; Ma, Y.; Liu, S.; Huang, W.; Zhao, Q. Controlling organic room temperature phosphorescence through external heavy-atom effect for white light emission and luminescence printing. *Adv. Optical Mater.* **2019,** *8* (4), 1901437.

17. Hirata, S.; Totani, K.; Zhang, J.; Yamashita, T.; Kaji, H.; Marder, S. R.; Watanabe, T.; Adachi, C. Efficient persistent room temperature phosphorescence in organic amorphous materials under ambient conditions. *Adv. Funct. Mater.* **2013,** *23* (27), 3386-3397.

18. Kwon, M. S.; Yu, Y.; Coburn, C.; Phillips, A. W.; Chung, K.; Shanker, A.; Jung, J.; Kim, G.; Pipe, K.; Forrest, S. R.; Youk, J. H.; Gierschner, J.; Kim, J. Suppressing molecular motions for enhanced room-temperature phosphorescence of metal-free organic materials. *Nat. Commun.* **2015,** *6*, 8947.

19. Papkovsky, D. B.; Dmitriev, R. I. Biological detection by optical oxygen sensing. *Chem. Soc. Rev.* **2013,** *42* (22), 8700-32.

20. Hirata, S.; Totani, K.; Zhang, J. X.; Yamashita, T.; Kaji, H.; Marder, S. R.; Watanabe, T.; Adachi, C. Efficient persistent room temperature phosphorescence in organic amorphous materials under ambient conditions. *Adv. Funct. Mater.* **2013,** *23* (27), 3386-3397.

21. Vanderkooi, J. M.; Maniara, G.; Green, T. J.; Wilson, D. F. An optical method for measurement of dioxygen concentration based upon quenching of phosphorescence. *J. Biol. Chem.* **1987,** *262* (12), 5476-5482.

22. Schulman, E. M.; Parker, R. T. Room-temperature phosphorescence of organic-compounds - effects of moisture, oxygen, and nature of support-phosphor interaction. *J. Phys. Chem.* **1977,** *81* (20), 1932-1939.

23. Zang, L.; Shao, W.; Kwon, M. S.; Zhang, Z.; Kim, J. Photoresponsive luminescence switching of metal-free organic phosphors doped polymer matrices. *Adv. Optical Mater.* **2020,** *8*, 2000654.

24. Yu, Y.; Kwon, M. S.; Jung, J.; Zeng, Y.; Kim, M.; Chung, K.; Gierschner, J.; Youk, J. H.; Borisov, S. M.; Kim, J. Room-temperature-phosphorescence-based dissolved oxygen detection by core-shell polymer nanoparticles containing metal-free organic phosphors. *Angew. Chem. Int. Ed.* **2017,** *56* (51), 16207-16211.

25. An, Z.; Zheng, C.; Tao, Y.; Chen, R.; Shi, H.; Chen, T.; Wang, Z.; Li, H.; Deng, R.; Liu, X.; Huang, W. Stabilizing triplet excited states for ultralong organic phosphorescence. *Nat Mater* **2015,** *14* (7), 685-90.

26. Zhen, X.; Tao, Y.; An, Z.; Chen, P.; Xu, C.; Chen, R.; Huang, W.; Pu, K. Ultralong phosphorescence of water-soluble organic nanoparticles for in vivo afterglow imaging. *Adv. Mater.* **2017,** *29* (33), 1606665.

27. Fateminia, S. M. A.; Mao, Z.; Xu, S.; Yang, Z.; Chi, Z.; Liu, B. Organic nanocrystals with bright red persistent room-temperature phosphorescence for biological applications. *Angew Chem Int Ed Engl* **2017,** *56* (40), 12160-12164.

28. Cheng, Z.; Shi, H.; Ma, H.; Bian, L.; Wu, Q.; Gu, L.; Cai, S.; Wang, X.; Xiong, W. W.; An, Z.; Huang, W. Ultralong phosphorescence from organic ionic crystals under ambient conditions. *Angew Chem Int Ed Engl* **2018,** *57* (3), 678-682.

29. Hirata, S.; Totani, K.; Yamashita, T.; Adachi, C.; Vacha, M. Large reverse saturable absorption under weak continuous incoherent light. *Nat Mater* **2014,** *13* (10), 938-46.

30. Kabe, R.; Notsuka, N.; Yoshida, K.; Adachi, C. Afterglow organic light-emitting diode. *Adv. Mater.* **2016,** *28* (4), 655-60.

31. Lee, D.; Bolton, O.; Kim, B. C.; Youk, J. H.; Takayama, S.; Kim, J. Room temperature phosphorescence of metal-free organic materials in amorphous polymer matrices. *J. Am. Chem. Soc.* **2013,** *135* (16), 6325-6329.

32. Kwon, M. S.; Lee, D.; Seo, S.; Jung, J.; Kim, J. Tailoring intermolecular interactions for efficient room-temperature phosphorescence from purely organic materials in amorphous polymer matrices. *Angew Chem Int Ed* **2014,** *53* (42), 11177-81.

33. Yuan, S.; Feng, L.; Wang, K.; Pang, J.; Bosch, M.; Lollar, C.; Sun, Y.; Qin, J.; Yang, X.; Zhang, P.; Wang, Q.; Zou, L.; Zhang, Y.; Zhang, L.; Fang, Y.; Li, J.; Zhou, H. C. Stable metal-organic frameworks: Design, synthesis, and applications. *Adv. Mater.* **2018,** *30* (37), e1704303.

34. Cui, Y.; Li, B.; He, H.; Zhou, W.; Chen, B.; Qian, G. Metal-organic frameworks as platforms for functional materials. *Acc. Chem. Res.* **2016,** *49* (3), 483-93.

35. Silva, P.; Vilela, S. M.; Tome, J. P.; Almeida Paz, F. A. Multifunctional metal-organic frameworks: From academia to industrial applications. *Chem. Soc. Rev.* **2015,** *44* (19), 6774-803.

36. Wang, J.; Li, D.; Ye, Y.; Qiu, Y.; Liu, J.; Huang, L.; Liang, B.; Chen, B. A fluorescent metal-organic framework for food real-time visual monitoring. *Adv. Mater.* **2021,** *33* (15), e2008020.

37. Suresh, K.; Matzger, A. J. Enhanced drug delivery by dissolution of amorphous drug encapsulated in a water unstable metal–organic framework (mof). *Angew. Chem. Int. Ed.* **2019,** *58* (47), 16790-16794.

38. Wei, Z.; Gu, Z. Y.; Arvapally, R. K.; Chen, Y. P.; McDougald, R. N., Jr.; Ivy, J. F.; Yakovenko, A. A.; Feng, D.; Omary, M. A.; Zhou, H. C. Rigidifying fluorescent linkers by metal-organic framework formation for fluorescence blue shift and quantum yield enhancement. *J. Am. Chem. Soc.* **2014,** *136* (23), 8269-76.

39. Yang, X.; Yan, D. Strongly enhanced long-lived persistent room temperature phosphorescence based on the formation of metal-organic hybrids. *Adv. Optical Mater.* **2016,** *4* (6), 897-905.

40. Yang, X.; Yan, D. Long-afterglow metal-organic frameworks: Reversible guest-induced phosphorescence tunability. *Chem. Sci.* **2016,** *7* (7), 4519-4526.

41. Mieno, H.; Kabe, R.; Notsuka, N.; Allendorf, M. D.; Adachi, C. Long-lived room-temperature phosphorescence of coronene in zeolitic imidazolate framework zif-8. *Adv. Optical Mater.* **2016,** *4* (7), 1015-1021.

Chapter 2

Chorioretinal Hypoxia Detection Using Lipid-Polymer Hybrid Organic Room-Temperature Phosphorescent Nanoparticles

Zeng, Y.[§]; Nguyen, V. P.[§]; Li, Y.; Kang, D.; Paulus, Y. M.; Kim, J. "Chorioretinal Hypoxia Detection Using Lipid-Polymer Hybrid Organic Room-Temperature Phosphorescent Nanoparticles." **2021**, *submitted*. ([§]Both authors contributed equally to this work.)

Kim, J.; **Zeng, Y.**; Kang, D.; Paulus, Y. M.; Nguyen, V. P. "Room-Temperature Phosphorescence Nanoparticles and Methods of Making the Same." US Patent App. 63/121, 688. December 4, 2020

2.1 Introduction

Ischemia-induced hypoxia is a common complication that can lead to neovascularization and severe vision impairment in several diseases, including retinal vein occlusion (RVO),[1,2] proliferative diabetic retinopathy (PDR), sickle cell retinopathy (SCR), retinopathy of prematurity (ROP), and choroidal ischemia.[3-5] RVO is the 2nd most common retinal vascular disorder and represents a major cause of vision loss, affecting more than 16 million people worldwide.[6-8] In RVO, the retina within the affected occluded retinal vasculature can become ischemic and thereby become hypoxic.[9] RVO is a very heterogeneous disease with highly variable visual acuity outcomes. It is essential that physicians be able to prognosticate outcomes with patients to counsel them on treatments and set appropriate expectations. Therefore, it is critical to detect ischemia-induced hypoxia, the most important pathogenic and prognostic factor of RVO, to better understand RVO pathogenesis.[8] In addition, long-term visualization and quantification of retinal

hypoxia are strongly desirable and can lead to a better understanding of the pathophysiology of ischemic retinopathies, including RVO, PDR, SCR, and ROP.

Recently, several techniques have been developed to monitor hypoxia such as oxygen-sensitive microelectrodes, magnetic resonance imaging (MRI), flow oximetry system, dual wavelength retinal oximetry, and fluorescence and phosphorescence lifetime imaging.[10-13] However, these methods each have their limitations. Oxygen-sensitive microelectrode is very positionally-dependent. In tissue with focal hypoxia surrounded by physoxia (normal physiologic oxygen tension), multiple measurements are required, and hypoxic regions can be missed. In addition, this technique is a destructive procedure that requires the implantation of microelectrodes, limiting its clinical utility. Although MRI is a minimally invasive approach and provides a large field of view and depth information, it is unable to provide enough resolution to identify small areas of focal hypoxia (in-plane pixel size = 0.39×0.39 mm^2).[12] Retinal oximetry is a commercially available, non-invasive method to measure the percentage of hemoglobin oxygen saturation within the large retinal vasculature.[13] However, it is unable to measure choroidal oximetry, which provides oxygen to the central vision or fovea, and it is unable to measure the perivascular oxygen tension within tissue, where there can be hypoxia due to impaired ability of the tissue to extract oxygen from the vasculature in many disease states.[14-18] Fluorescence and phosphorescence lifetime imaging are minimally-invasive, optical approaches based on oxygen-dependent quenching of fluorescence or phosphorescence, which can be used to image and measure oxygen tension within retinal vessels.[10,19] One disadvantage of this technique is that it cannot provide long-term visualization of hypoxia due to rapid clearance of the injected small molecule dyes from the body. Thus, there is a critical clinical need for an effective, non-destructive

method to measure oxygen tension in the tissue microenvironment rather than strictly within retinal blood vessels, and no effective solution exists to this problem.

Metal-free purely organic phosphors are an emerging class of room-temperature phosphorescence (RTP) materials with unique properties such as long lifetime (milliseconds to seconds) and large Stokes shift (wavelength difference between the absorption and emission peak maxima).[20-24] These features endow organic phosphorescence-based sensors several advantages over traditional optical sensor design for hypoxia detection and imaging in biological systems. First, purely organic phosphorescence signal from the long-lived triplet excited state is highly susceptible to molecular oxygen quenching through triplet energy transfer,[25-30] whereas conventional fluorescent probes have short-lived emission (nanoseconds), and thus are typically insensitive to oxygen tension change. Second, the large Stokes shift effectively eliminates the interference of the excitation light source or the background autofluorescence by wavelength-based deconvolution, enabling high signal-to-noise ratio measurements. Last, unlike conventional inorganic or organometallic-based RTP materials such as Oxyphors[31] containing precious rare-earth and transition metals with potential toxicity or stability issues in bio-applications,[32] purely organic phosphors are more cost-effective, robust, and biocompatible.

There are several key design considerations to achieve bright organic RTP, including molecular motion suppression[33-35] through doping in rigid hosts such as solid-state crystalline structures or rigid polymer films. However, these strategies limit the practical applicability of organic phosphors toward *in vivo* hypoxia detection since good oxygen diffusivity, excellent aqueous dispersibility, and biocompatibility also need to be integrated in material design and processing. Consequently, despite the great potential, there are very few organic RTP material systems exploited as *in vivo* oxygen sensors.[36-39]

This report describes a lipid-polymer hybrid core-shell, metal-free organic RTP nanoparticle (NP) platform that can optically visualize chorioretinal tissue hypoxia in real-time with high signal-to-noise ratio (SNR). Specifically, through a facile one-pot self-assembly protocol, the oxygen-sensitive organic phosphor is encapsulated in a rigid, oxygen-permeable polymer matrix core, which is further encased in a layer of phospholipid shell. Such formulation of organic phosphors into nanoprobes represents an effective strategy to enhance their biocompatibility and spatiotemporal resolution for *in vivo* bioimaging. The fabricated hybrid NPs exhibit long-lived bright RTP with high sensitivity toward oxygen quenching and good long-term stability *in vitro*, making them promising tissue hypoxia imaging agents for pre-clinical studies. As a proof of concept, the *in vivo* tissue oxygen-sensing efficacy and biosafety of these RTP NPs are assessed via intravitreal injection in a rabbit RVO model and intravenous (IV) injection in a rabbit choroidal vascular occlusion (CVO) model. To the best of our knowledge, this work represents the first non-destructive method to longitudinally visualize oxygen tension in the chorioretinal tissue rather than in hemoglobin within the retinal vasculature. The reported hybrid RTP NP platform could enable quantitative mapping of oxygen gradient and measure the degree of tissue ischemia with high spatiotemporal resolution.

2.2 Results and Discussion

2.2.1 Self-assembly of lipid-polymer hybrid organic RTP NPs

A facile and versatile assembling approach for organic RTP nanomaterials is required for practical biosensing and bioimaging applications. Nanoprecipitation is a simple method which can produce homogenous NPs rapidly on a large scale by utilizing a sharp solubility change of host materials in miscible dissimilar solvents.[40] Here we developed a new type of lipid-polymer hybrid,

core-shell RTP NPs, termed Br6A-LPS4Br NPs, with the metal-free organic phosphor embedded within the polymer matrix core, the surface of which was further coated with an amphiphilic lipid shell. Poly(4-bromostyrene) (PS4Br) was chosen as the host polymer, and Br6A, previously reported by our lab,[41] as the metal-free organic phosphor for the NP assembly (Figure 2.1). In addition to the optical inertness, the rigidity and oxygen permeability of PS4Br are two critical parameters for the nanosensor design in order to achieve bright and sensitive RTP for tissue hypoxia detection. The high rigidity of the host polymer is required to effectively suppress the vibrational energy dissipation of the metal-free phosphor for bright RTP emission.[33] Good oxygen permeability of the polymer matrix is necessary for the embedded organic phosphor to respond to oxygen tension change in the surrounding environment in real-time. Styrene-based polymers have desirable rigidity and proper oxygen permeability and have been exploited in sensors for dissolved oxygen detection.[30,42,43] Additionally, we envision that PS4Br, the brominated polystyrene matrix can enhance the RTP emission of Br6A through external halogen bonding. The halogen bonding between the oxygen atom of the carbonyl group of Br6A and the neighboring bromine atom of PS4Br can further suppress the vibrational energy dissipation meanwhile enhancing spin–orbit coupling and intersystem crossing of Br6A.[41]

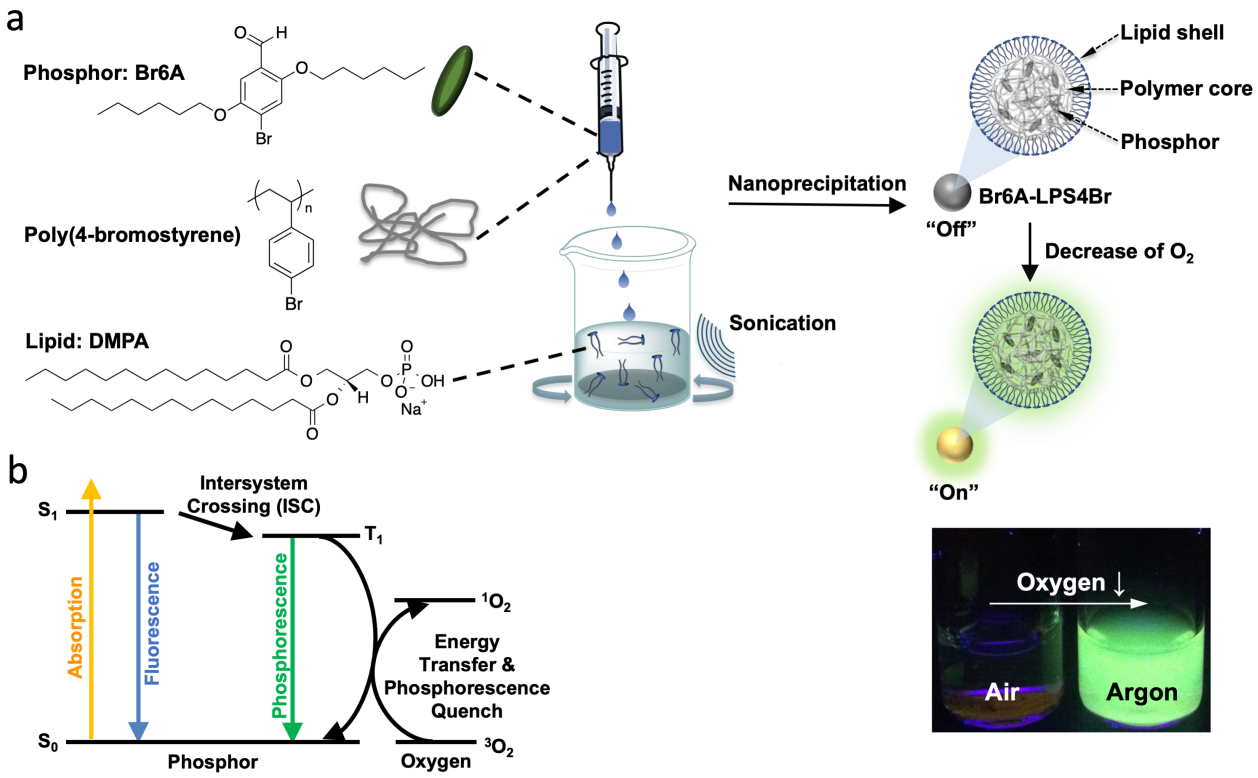

Figure 2.1 | Materials design strategy for biocompatible oxygen-sensing. a, Synthetic procedure of lipid-polymer hybrid core-shell, room-temperature phosphorescent nanoparticles, Br6A-LPS4Br NPs. The phosphorescence signal of NPs aqueous suspension is susceptible to oxygen quenching. **b,** Simplified Jablonski diagram showing the mechanism of phosphorescence quenching by molecular oxygen through triplet energy transfer. S_0, S_1, and T_1 are the singlet ground state, first excited singlet state, and excited triplet state of the organic phosphor, respectively.

Lipid coating on the solid polymeric core was achieved by adding an anionic phospholipid, 1,2-dimyristoyl-sn-glycero-3-phosphate (DMPA) in the aqueous outer phase during the nanoprecipitation process. As the main components of cellular membrane, phospholipids have excellent biocompatibility.[44] Its amphiphilic and anionic structure can help increase the NPs' stability in water by preventing their aggregation through electrostatic repulsion or hydration,[45-49] particularly at concentrated states and for long-term storage. It is important to note that direct injection of polymer solution at a high concentration (10 mg/mL PS4Br) to the aqueous outer phase without DMPA lipid resulted in massive aggregation instead of discrete NPs. Stable Br6A-PS4Br

NPs can be produced only at a low polymer concentration (1 mg/mL). Thus, the addition of DMPA lipids also ensured homogeneous dispersion of the polymer in the aqueous phase. Dynamic light scattering (DLS) data indicate fairly narrow-dispersed Br6A-LPS4Br NPs at an encapsulation ratio of 5 wt% Br6A (with respect to PS4Br), with an average hydrodynamic diameter of 163.9 ± 2.7 nm (mean ± S.D., n = 3) and polydispersity index (PDI) of 0.134 ± 0.008 (mean ± S.D., n = 3) in Milli-Q water (Figure 2.2a,b). The more negative zeta potential (ζ) of the resulting Br6A-LPS4Br (−44.7 ± 0.5 mV) in comparison to bare Br6A-PS4Br (−32.1 ± 0.8 mV) suggests the successful coating of the negatively charged DMPA lipid on the NP surface (Figure 2.2c). Particle size and its spherical shape were further confirmed by scanning electron microscope (SEM, Figure 2.2d).

The colloidal stability of RTP NPs is an important criterion for their long-term *in vivo* oxygen-sensing applications. We studied the temporal storage stability of Br6A-LPS4Br NPs by monitoring the change in their size and polydispersity over 13 weeks. The stock solution (2.5 mg/mL) was stored in Milli-Q water under ambient conditions. There was no sign of aggregation of the RTP NPs suspension over 13 weeks, as shown in Figure 2.2e. Therefore, this simple one-step nanoprecipitation method is suitable for robust production of lipid-stabilized, polymer-supported organic RTP NPs.

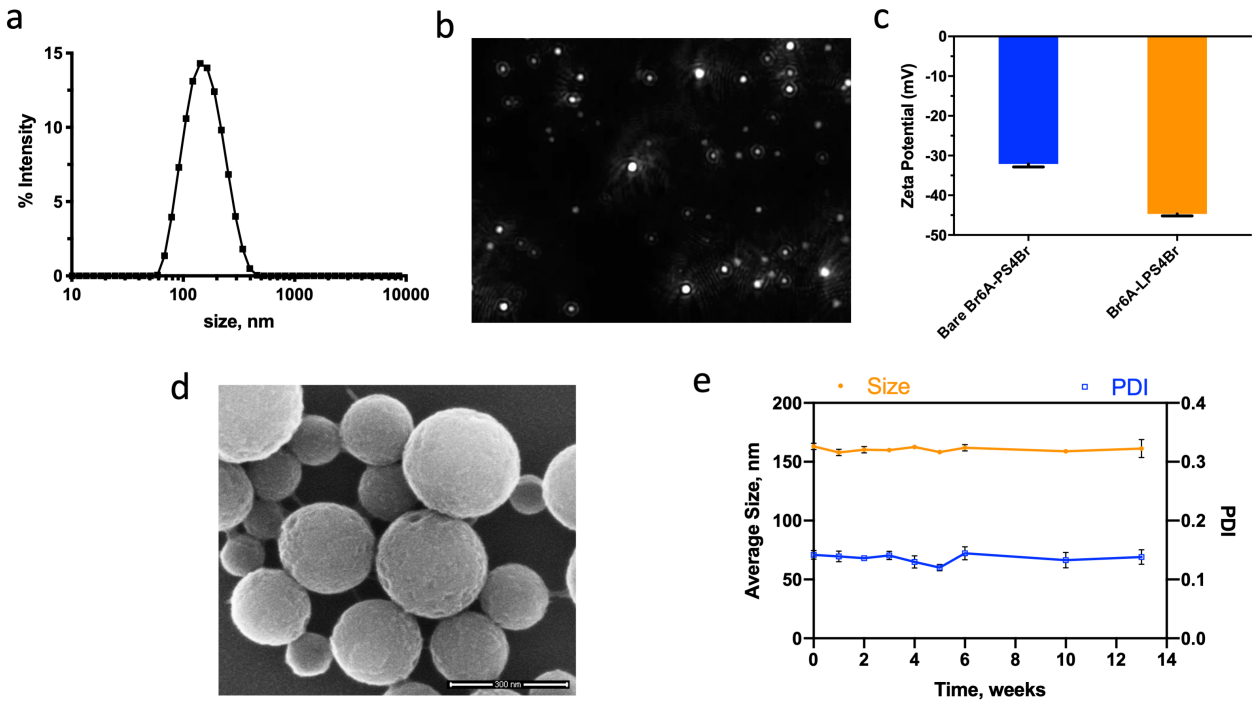

Figure 2.2 | Chemophysical characterizations and colloidal stability of Br6A-LPS4Br NPs. **a**, Hydrodynamic size (diameter, nm) distribution of Br6A-LPS4Br NPs measured by dynamic light scattering (DLS). Well-dispersed NPs in aqueous solutions with an average hydrodynamic diameter of 163.9 nm (PDI: 0.134) were fabricated from a single-step nanoprecipitation process. **b**, Light-scattering image of Br6A-LPS4Br NPs visualized by Nanoparticle Tracking Analysis, corroborating well-dispersed NPs in aqueous solutions. **c**, Surface zeta potential change with and without lipid DMPA coating. Compared to bare Br6A-PS4Br NPs, Br6A-LPS4Br exhibited a relatively more negative value, indicating its surface was successfully coated with anionic DMPA. **d**, Morphology of Br6A-LPS4Br NPs observed by scanning electron microscopy. Scale bar: 300 nm. **e**, Temporal stability of Br6A-LPS4Br NPs stored in Milli-Q water at room temperature. NPs size (orange line) and polydispersity (blue line) were monitored over the course of 13 weeks using DLS. No obvious aggregation was observed, suggesting long-term stability. All error bars indicate S.D. (n = 3).

2.2.2 Phosphorescence properties of organic RTP NPs

The RTP nature of the emission from the fabricated Br6A-LPS4Br NPs was then confirmed. As expected, the NPs aqueous suspension exhibited bright green emission under 365 nm excitation after the removal of dissolved oxygen by argon purging (photograph in Figure 2.1). Steady state photoluminescence spectroscopy data confirmed the excitation and emission spectra maxima at 360 nm and 530 nm, respectively. The small shoulder peak around 425 nm corresponds

to the fluorescence emission of Br6A. The gated emission spectrum acquired after a 500 μs delay well-overlapped with the steady state emission maxima at 530 nm, which indicated that the green emission is indeed of phosphorescent nature rather than fluorescent (Figure 2.3a). Lifetime (τ) measurement of the green emission monitored at 530 nm resulted in 4.0 milliseconds (ms) (Figure 2.3b), further corroborating the phosphorescent emission. Quantum efficiency of Br6A-LPS4Br NPs in anoxic aqueous suspension Φ_p (455–675 nm) was measured to be 16.9 ± 3.0%. Therefore, these photophysical characteristics of Br6A-LPS4Br NPs are in good agreement with those of Br6A in crystalline state[41] or embedded in isotactic poly(methyl methacrylate) film[35] reported previously, indicating the successful inclusion of Br6A into the NP matrix by nanoprecipitation method. We then tested the total emission intensity of Br6A-LPS4Br NPs aqueous suspension with various partial pressures of oxygen (pO_2 from 0–21%). The green phosphorescence emission is highly responsive to small changes in pO_2, with gradually quenched phosphorescence signal as the pO_2 increased, whereas the fluorescence emission at 420 nm remained the same (Figure 2.3c). This confirms our hypothesis that the phosphorescence emission of Br6A-based RTP NPs can be applied for sensitive hypoxia detection. Though measurements with more precise control over pO_2 would be needed to calculate the hypoxia detection range, it is reasonable to estimate that these RTP NPs will be able to distinguish differences of approximately 3% in pO_2, and hence with great potential to determine different degrees of tissue ischemia. In addition, we studied the optical stability of Br6A-LPS4Br NPs and found that the total emission intensity of the NPs suspension upon Argon purging remained the same after 13 weeks (Figure 2.3d).

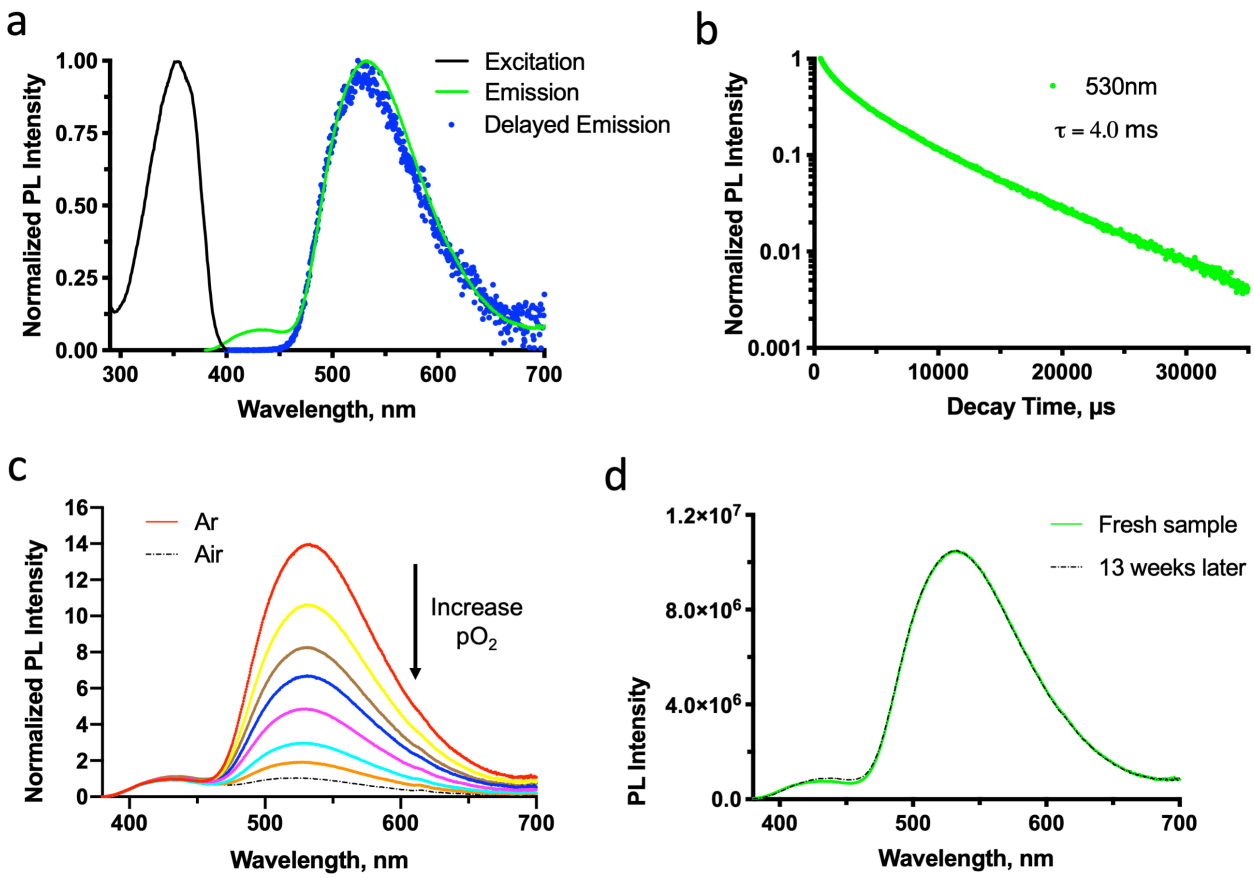

Figure 2.3 | Photophysical characterizations and optical stability of Br6A-LPS4Br NPs. **a**, Steady state photoluminescence excitation, emission, and delayed emission (delayed for 500 µs) spectra of Br6A-LPS4Br NPs dispersed in Argon (Ar)-purged, anoxic aqueous solution. **b**, Phosphorescence lifetime of RTP NPs in an anoxic aqueous solution monitored at 530 nm (λ_{ex} = 365 nm). Photophysical properties of Br6A-LPS4Br NPs confirmed that the green, 530 nm emission is indeed of phosphorescent nature. **c**, Oxygen sensitivity calibration. Steady state photoluminescence emission of Br6A-LPS4Br NPs suspension at various O_2 saturation levels (0–21%). λ_{ex} = 365 nm. **d**, Optical stability of Br6A-LPS4Br NPs measured by steady state photoluminescence spectroscopy. The NPs stock solution (2.5 mg/mL) was stored in Milli-Q water under ambient conditions. The total emission intensity of the NPs suspension upon Argon purging remained the same after 13 weeks.

2.2.3 In vivo imaging of organic RTP NPs in rabbit RVO models

To evaluate the efficiency of organic RTP NPs as *in vivo* nanosensors for the detection of tissue hypoxia, the synthesized Br6A-LPS4Br NPs were administrated intravitreally into six rabbits with laser-induced hemi-RVO as described previously to obtain localized hypoxia.[50,51] After acquiring baseline images one week post laser-induced RVO (Figure 2.4), 50 µL of Br6A-

LPS4Br NPs at a concentration of 2.5 mg/mL was administrated to the rabbits via intravitreal injection. Longitudinal distribution and phosphorescence signal of the NPs was monitored for up to 7 days post-injection using color fundus photography and fundus phosphorescence imaging (Figure 2.5). The phosphorescence intensity was determined using the regions of interest (ROI) analysis method. Figure 2.5 shows *in vivo* longitudinal visualization of hypoxia and the surrounding retinal vasculature pre- and post-administration of Br6A-LPS4Br NPs at different time points such as 15 min, 1, 2, 4, 8, and 24 hours, and 2, 4, and 7 days. Figure 2.5a and 2.5c illustrate the color fundus images of two different sides of the same rabbit eye: the hypoxic RVO side and the physoxic control (untreated) side. There was no phosphorescent signal observed before the injection of Br6A- LPS4Br NPs and the NPs were clearly visualized starting at 1 h post-injection (Figure 2.5b). These images demonstrate dynamic changes of the RTP signal of Br6A-LPS4Br NPs over time. The location of NPs is clearly visualized at 1–2 h post-injection and is still visible up to 7 days on the hypoxic side. This contrast indicates the ability of these organic RTP NPs to track tissue hypoxia *in vivo* over multi-day period without having to do re-injection. As expected for the untreated side, no phosphorescence signal was detected over time given the normal tissue oxygen tension (Figure 2.5d). By applying an image segmentation algorithm to separate the contrast derived from the distribution of Br6A-LPS4Br NPs, average phosphorescence intensity (API) was quantified for each time point (Figure 2.5e). This quantification shows that API significantly increased post-injection compared to pre-injection of Br6A-LPS4Br NPs. The API in the hypoxia increased by 4.97-fold over the first hour post-injection from 8.58 ± 1.46 (a.u.) pre-injection to 42.67 ± 0.07 (a.u.) ($p < 0.001$) and reached a peak at 2 h post-injection (API = 45.13 ± 1.31 (a.u.)), yielding a SNR of 12.5 (First Standard Deviation method). Although the API

then decreased over time, it was still 168 % higher at day 7 (API = 14.45 ± 8.86 (a.u.)) compared to pre-injection.

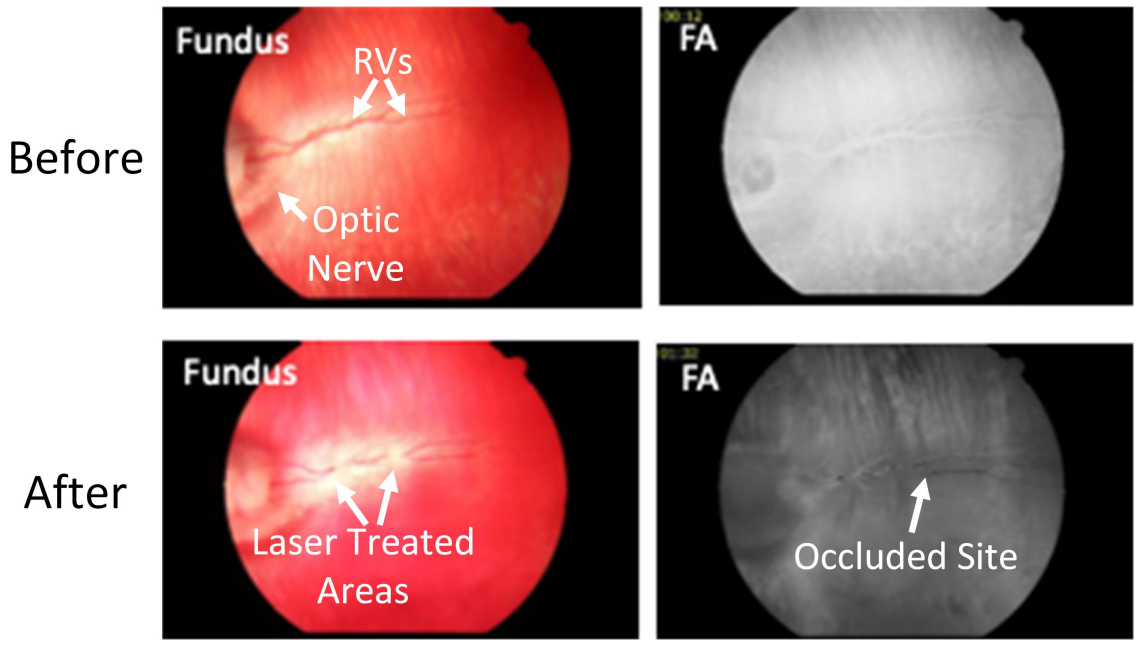

Figure 2.4 | Rose-Bengal RVO model generation demonstrating occlusion of the retinal vasculature of the medullary ray after laser irradiation. Color fundus photography (top left) and fluorescein angiography (FA) (top right) images show the location of the optic nerve and retinal vessels (RVs, white arrows) and normal blood flow. In contrast, the blood vessels were completely occluded with significantly reduced blood flow (white arrow) observed on the FA image after laser irradiation (bottom right).

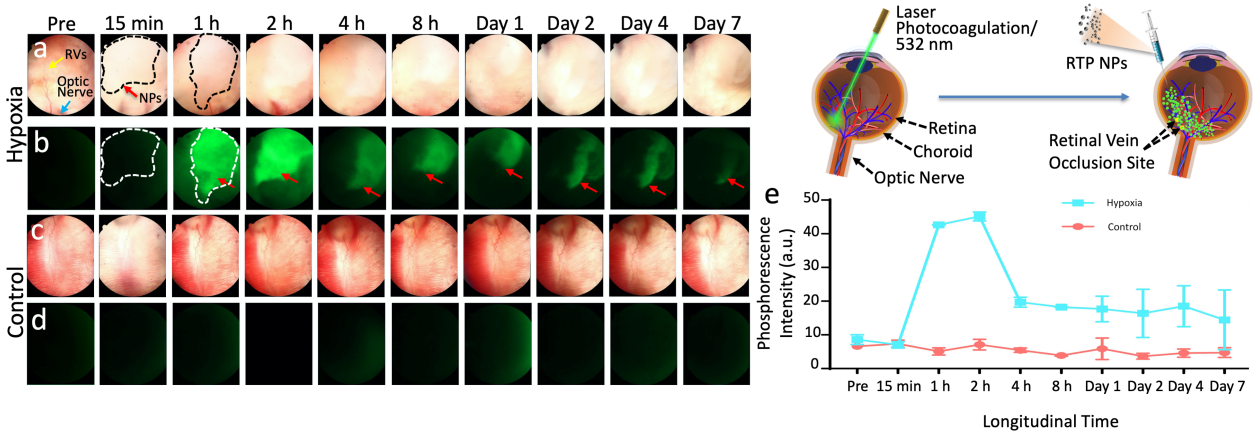

Figure 2.5 | Longitudinal phosphorescence imaging of intravitreal Br6A-LPS4Br NPs in living rabbit retinal hypoxia and control over 7 days (λ_{ex} = 365 nm, λ_{em} = 530 nm). a,c, Color fundus photographs of the hypoxic (**a**) and the physoxic control (**c**) side of the same rabbit before and after intravitreal administration of Br6A-LPS4Br NPs (50 μL, 2.5 mg/mL) at different time points (15 min, 1, 2, 4, 8 h and day 1, 2, 4, and 7). The color fundus photographs show rabbit fundus features such as retinal vessels (RVs) (yellow arrow), choroidal vessels, optic nerve (turquoise arrows), and distribution of NPs in the vitreous. **b,d,** Phosphorescence images of the hypoxic (**b**) and the physoxic control (**d**) side before and up to 7 days after intravitreal administration of Br6A-LPS4Br NPs. Black dotted circles (**a**) and white dotted circles (**b**) indicate the position of NPs. Red arrow (**b**) indicates the location of phosphorescence signal. **e,** Average phosphorescence intensity measured from the hypoxic side (blue line) and the control side (red line). Error bars show the standard deviations of three independent measurements. The phosphorescence signal increased significantly on the hypoxic side by 1 h post-injection, peaked at 2 h post-injection, and persisted for at least 7 days.

The *in vivo* reproducibility of retinal hypoxia detection by organic RTP NPs was verified in other rabbits with laser-induced RVO two weeks prior to intravitreal injection of Br6A-LPS4Br NPs with the same dose and concentration (50 μL, 2.5 mg/mL) (Figure 2.6). Hypoxia was monitored for 7 days. Phosphorescence images showed high contrast and peaked at 2 h post-injection, reconfirming the *in vivo* hypoxia detecting and tracking capability of these organic RTP NPs for different degrees of tissue ischemia. To further validate that the phosphorescence signal is activated by local hypoxia, Br6A-LPS4Br NPs (50 μL, 2.5 mg/mL) was injected into a normal rabbit and imaged with color fundus photography and fundus phosphorescence imaging at different time points over a period of 17 days (Figure 2.7). Phosphorescence signal was not

detected either in the nanoparticle-injected side or in the non-injected side (Figure 2.7b,d), and ROI analysis shows that API did not change over time (Figure 2.7e). These results confirmed that the RTP signal of Br6A-LPS4Br NPs is quenched under normal oxygen tension in a healthy retina, and hence the developed RTP NPs can selectively detect ischemia-induced hypoxia.

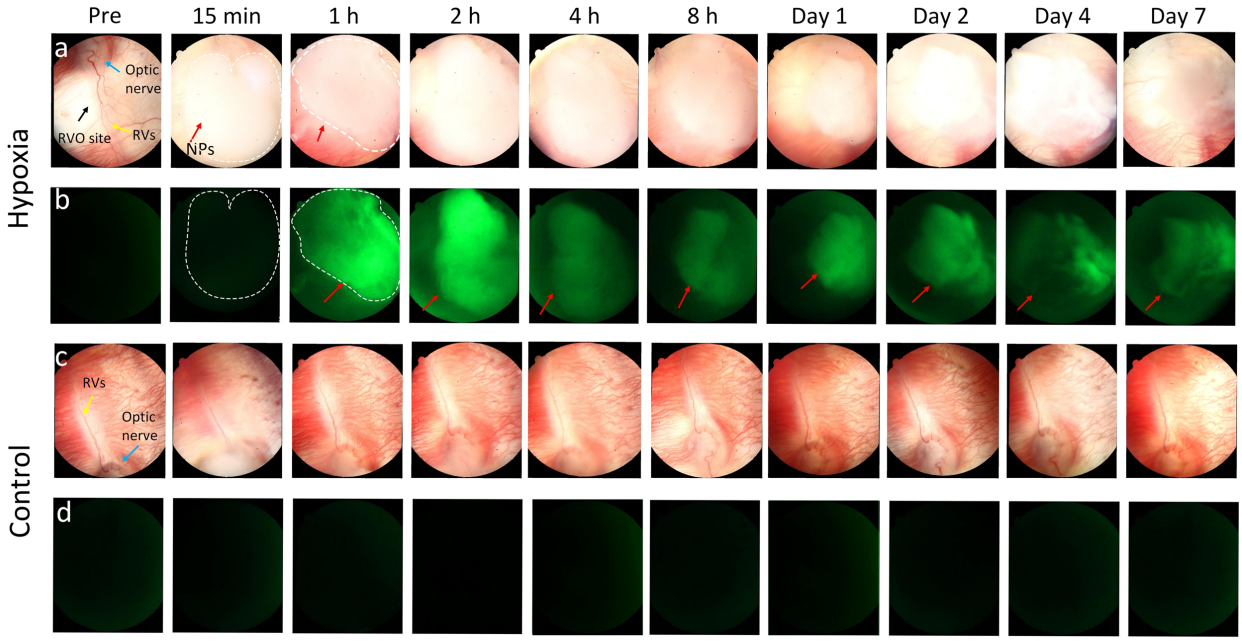

Figure 2.6 | *In vivo* phosphorescence imaging of retinal hypoxia acquired at different time points post-intravitreal injection of Br6A-LPS4Br NPs in a living rabbit. a,c, Color fundus photograph of the hypoxic (**a**) and the physoxic control (**c**) side of the same rabbit eye acquired pre- and post-injection of Br6A-LPS4Br NPs (50 µL, 2.5 mg/mL) at day 14 post laser-induced RVO model. Yellow arrow indicates the location of retinal vessels (RVs), black arrow represents the RVO site, turquoise arrow illustrates the position of optic nerve, and red arrow shows the position of Br6A-LPS4Br NPs after injection. **b,d,** In vivo phosphorescence images of the hypoxic (**b**) and the physoxic control (**d**) side acquired at pre, 15 min, 1, 2, 4, 8 h and day 1, 2, 4, and 7 post-injection of Br6A-LPS4Br NPs. The distribution of RTP NPs post-injection is co-registered with the fundus color photograph (white dotted circle). RTP NPs clearly showed up on phosphorescence images at 1 h post-injection with high contrast.

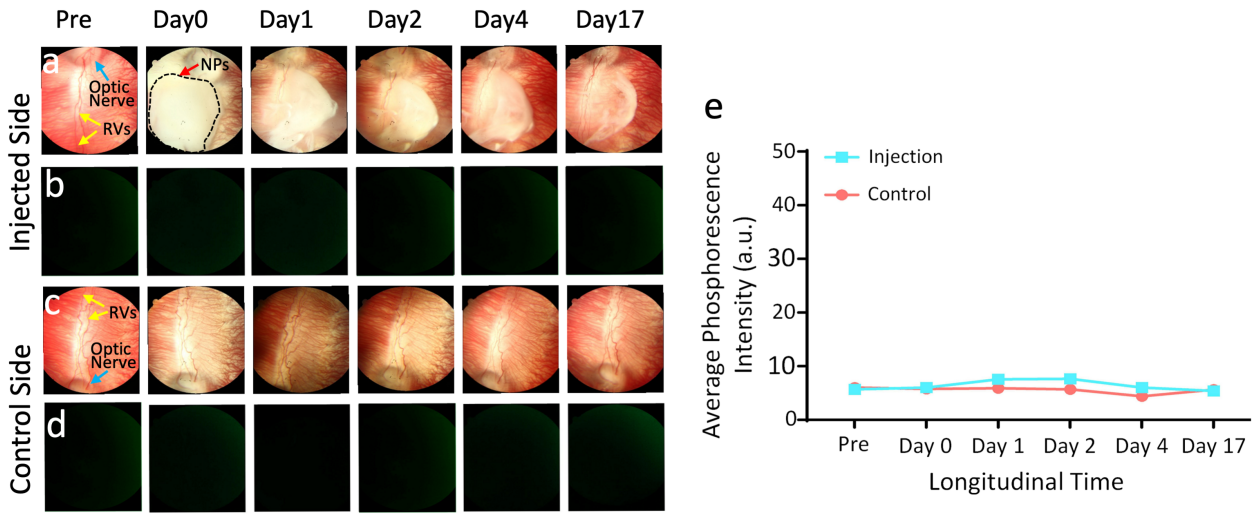

Figure 2.7 | Longitudinal phosphorescence imaging of a healthy control rabbit before and up to 17 days after the injection of Br6A-LPS4Br NPs. a,c, Color fundus photography at the injection side (**a**) and non-injection side (**c**) in normal, healthy control rabbits. **b,d,** Corresponding phosphorescence images of the injection (**b**) and non-injection (**d**) side. Black dotted line in a shows the margin of RTP NPs post-injection. **e,** Average phosphorescence intensities from the injection (blue line) and non-injection (red line) side over 17 days. No phosphorescence emission was observed on the phosphorescence images at any time point since there is no tissue hypoxia.

2.2.4 In vivo multimodal imaging of organic RTP NPs

We then sought out to confirm that the signal generated in the hypoxic area of the RVO model is truly arising from the phosphorescence emission of Br6A in RTP NPs. A near-infared fluorescent dye (IR-780) was co-encapsulated with the organic phosphor Br6A, yielding narrow-dispersed (PDI: 0.108 ± 0.012) Br6A-IR780-LPS4Br NPs with an average hydrodynamic diameter of 130.5 ± 1.7 nm (Figure 2.8a), to allow for dual phosphorescence and fluorescence imaging. Since the fluorescent signal of IR-780 is not affected by oxygen tension change, co-localizing the fluorescence and phosphorescence signals allows us to track the post-injection distribution of RTP NPs. Intravitreal injection of Br6A-IR780-LPS4Br NPs (50 μL, 2.5 mg/mL) into the RVO rabbit showed co-localization of the fluorescence signal of IR780 and the phosphorescence signal (Figure 2.8b,c), indicating the hyperphosphorescence signal in the RVO model originates from Br6A in the RTP NPs in response to tissue hypoxia.

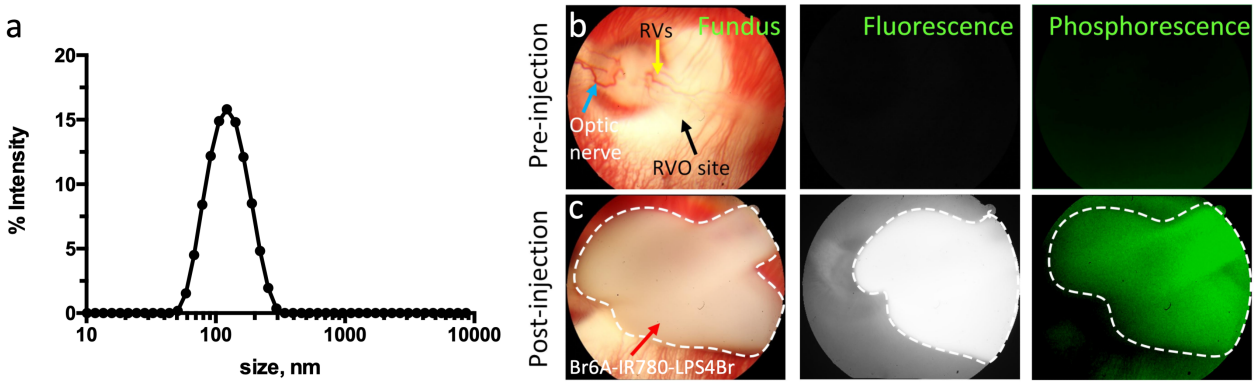

Figure 2.8 | *In vivo* multimodal fluorescence and phosphorescence images of intravitreal Br6A-IR780-LPS4Br NPs and retinal hypoxia in living rabbits. a, Hydrodynamic size distribution of Br6A-IR780-LPS4Br NPs measured by dynamic light scattering. Narrow-dispersed (PDI: 0.108 ± 0.012), fluorescent dye (IR-780) and organic phosphor (Br6A) co-encapsulated RTP NPs with an average hydrodynamic diameter of 130.5 ± 1.7 nm were synthesized using a similar nanoprecipitation method. **b,c,** Fundus photography, fluorescence, and phosphorescence images obtained before (**b**) and after (**c**) intravitreal administration of 50 µL of Br6A-IR780-LPS4Br NPs at a concentration of 2.5 mg/mL. White dotted lines show the distribution of RTP NPs in the vitreous post-injection, the corresponding fluorescence emission from IR-780, and the corresponding phosphorescence emission from Br6A. The results show close correlation between the fluorescent and phosphorescent signal, indicating that the phosphorescent signal in the rabbit RVO model is emanating from RTP NPs.

2.2.5 In vivo imaging of organic RTP NPs in rabbit CVO models

To realize minimally invasive delivery of these organic RTP NPs for *in vivo* hypoxia imaging, we identified an RTP NPs formulation suitable to be administrated intravenously. Nanotherapeutics via intravenous delivery are usually formulated with average sizes of 10–150 nm in diameter to reduce reticuloendothelial system (RES) clearance and evade the 5 nm renal filtration cut off.[52,53] Unlike normal blood vessels with endothelial tight junctions and blood–retina barrier, occluded retinal vessels tend to be disorganized and demonstrate hyperpermeability.[54,55] With these design criteria in mind, we hypothesized that smaller RTP NPs in the sub-100 nm range will more effectively extravasate and accumulate at occluded sites, leveraging the enhanced permeability and retention (EPR) effect. They will also more likely to have higher diffusivity, allowing for more efficient penetration into the hypoxic chorioretinal tissue. Therefore, we used a

more hydrophilic diblock copolymer, polystyrene-*b*-poly(4-vinylpyridine) (PS4VP, PS block MW 35.5 kD and P4VP block MW 4.4 kD, Figure 2.9a), as the host matrix to construct NPs' polymeric core, which leads to smaller RTP NPs via bulk nanoprecipitation. Similar to polystyrene, P4VP is highly rigid at room temperature, and is oxygen-permeable.[56] The low block ratio of P4VP in the overall diblock copolymer allows PS4VP to have similar characteristics in its rigidity and oxygen permeability compared to polystyrene. Hence, the resulting RTP NPs have brightness and sensitivity comparable to those of Br6A-LPS4Br NPs toward hypoxia detection. IR-780 was co-encapsulated for particle tracking in blood vessels and the retina. To improve RTP NPs' biocompatibility and pharmacokinetics for systemic delivery, a FDA-approved lipid-PEG conjugate, 1,2-distearoyl-sn-glycero-3-phosphoethanolamine-N-[carboxy(polyethylene glycol)-2000] (DSPE-PEG2000), was used instead of DMPA to create a "stealth" shell on the surface of the organic RTP NPs.[57] By means of a similar nanoprecipitation procedure as described before, RTP NPs Br6A-IR780-LPS4VP-PEG with an average hydrodynamic diameter of 46.1 ± 0.6 nm and PDI of 0.134 ± 0.005 were successfully synthesized (Figure 2.9b).

The choroid is a vascular-rich tissue immediately deep to the retina which supplies oxygen to the outer half of the retina including the fovea, or central vision, and thus it is critical to understand tissue oxygen tension within both the retina and choroid. Using an established rabbit model of CVO with laser photocoagulation[58] (Figure 2.10), we found that intravenously administrated Br6A-IR780-LPS4VP-PEG NPs were able to effectively accumulate at the laser lesions (~ 300 μm in diameter) in the choroid and detect focal tissue hypoxia in a "turn-on" modality with a peak RTP signal at 2 h post-injection (Figure 2.9d–f). While the phosphorescence signal wasn't clearly visualized until 1 h post intravitreal injection in rabbits with RVO, it was clearly visible here at 15 min post IV injection. This is likely due to the different initial oxygen

levels in RTP NPs. For intravitreal injection, the NPs suspension is initially saturated with atmospheric oxygen (~ 21% O_2). It takes time to deplete the dissolved oxygen injected along with the NPs at the hypoxia site before the phosphorescence signal can be turned on. In contrast, NPs after IV injection is immediately diluted with high volume of blood and hence can be considered at physoxia, i.e. much lower levels of oxygen universally found in blood and normal tissues, approximately 5–13% and 4–7.5%, respectively.[59]

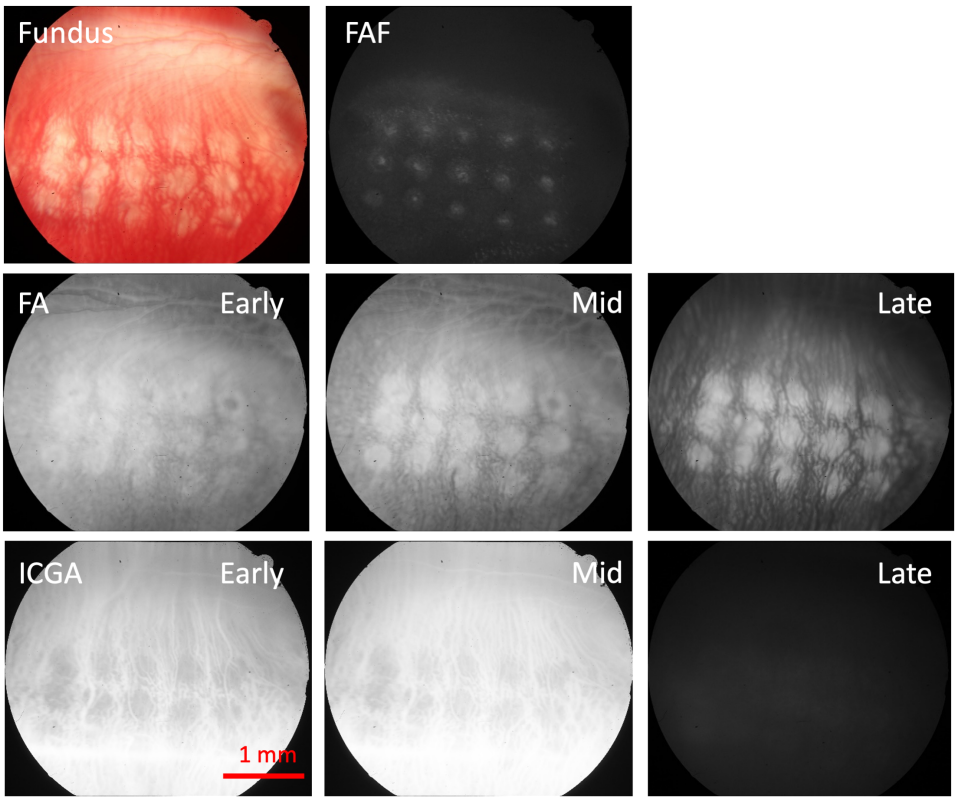

Figure 2.9 | CVO model generation and leakage confirmation at day 7 post photocoagulation. Top row images show color fundus photography (left) and fundus autofluorescence (FAF) image (right). Middle and bottom rows exhibit fluorescein angiography (FA) and indocyanine green angiography (ICGA) images acquired at different phases (early, middle, and late) after intravenous injection of fluorescein sodium and ICG, respectively. This demonstrates whitening on fundus photography, progressive hyperfluorescence on FA, and hypofluorescence on ICGA, consistent with CVO.

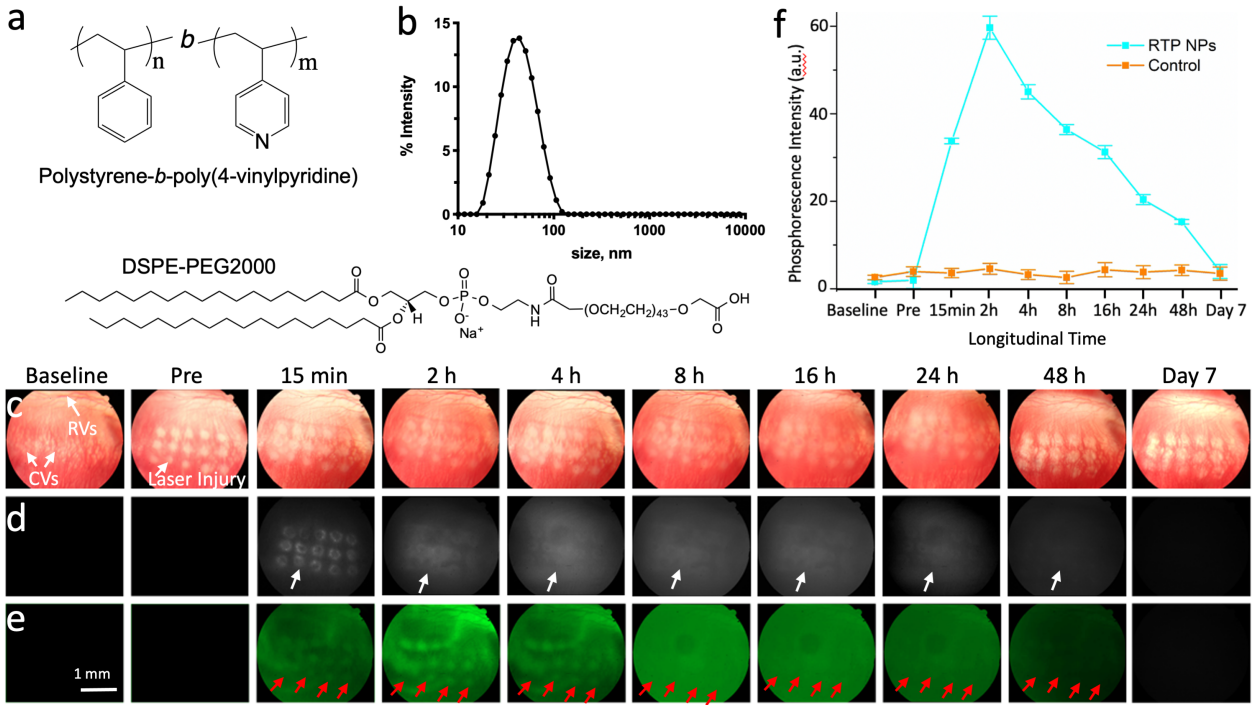

Figure 2.10 | *In vivo* phosphorescence images of Br6A-IR780-LPS4VP-PEG NPs and chorioretinal hypoxia in living rabbits. a, Chemical structure of polymer PS4VP and phospholipid DSPE-PEG2000. **b**, Dynamic light scattering measurement of Br6A-IR780-LPS4VP-PEG NPs fabricated from PS4VP and DSPE-PEG2000. Fairly narrow-dispersed (PDI: 0.134 ± 0.005), fluorescent dye (IR-780) and organic phosphor (Br6A) co-encapsulated RTP NPs with an average hydrodynamic diameter of 46.1 ± 0.6 nm were synthesized using a similar nanoprecipitation method. **c**–**e**, Color fundus photography (**c**), fluorescence (**d**), and phosphorescence (**e**) images before and after intravenous injection of 4 mL Br6A-IR780-LPS4VP-PEG NPs at a concentration of 2.5 mg/mL. Color fundus images in **c** show the healthy retinal vessels (RVs), choroidal vessels (CVs) as well as the location of laser injured sites (white spots). Fluorescence and phosphorescence images obtained before and post injection at different time points, demonstrating the accumulation of RTP NPs at laser lesions (white arrow) and the corresponding phosphorescent signal from the RTP NPs (red arrows) detecting tissue hypoxia. **f**, Quantification of mean phosphorescence intensities at laser lesions over 7 days. Phosphorescent signal was not visible before the injection of RTP NPs or on the physoxic control side. In contrast, the phosphorescent signal increased significantly in the hypoxic areas at 15 min post-injection, peaked at 2 h post-injection, and gradually decreased after that. Error bars show the standard deviations of three independent measurements.

To confirm the phosphorescent signal detected is attributed to RTP NPs selectively sensing hypoxia rather than tissue autofluorescence, NPs encapsulated with IR-780 only and no Br6A (IR780-LPS4VP-PEG NPs) was injected intravenously into rabbits with CVO. Consequently, only

the fluorescent signal showing NPs location was observed, and no hyperphosphorescence at the occluded hypoxic laser lesions (Figure 2.11).

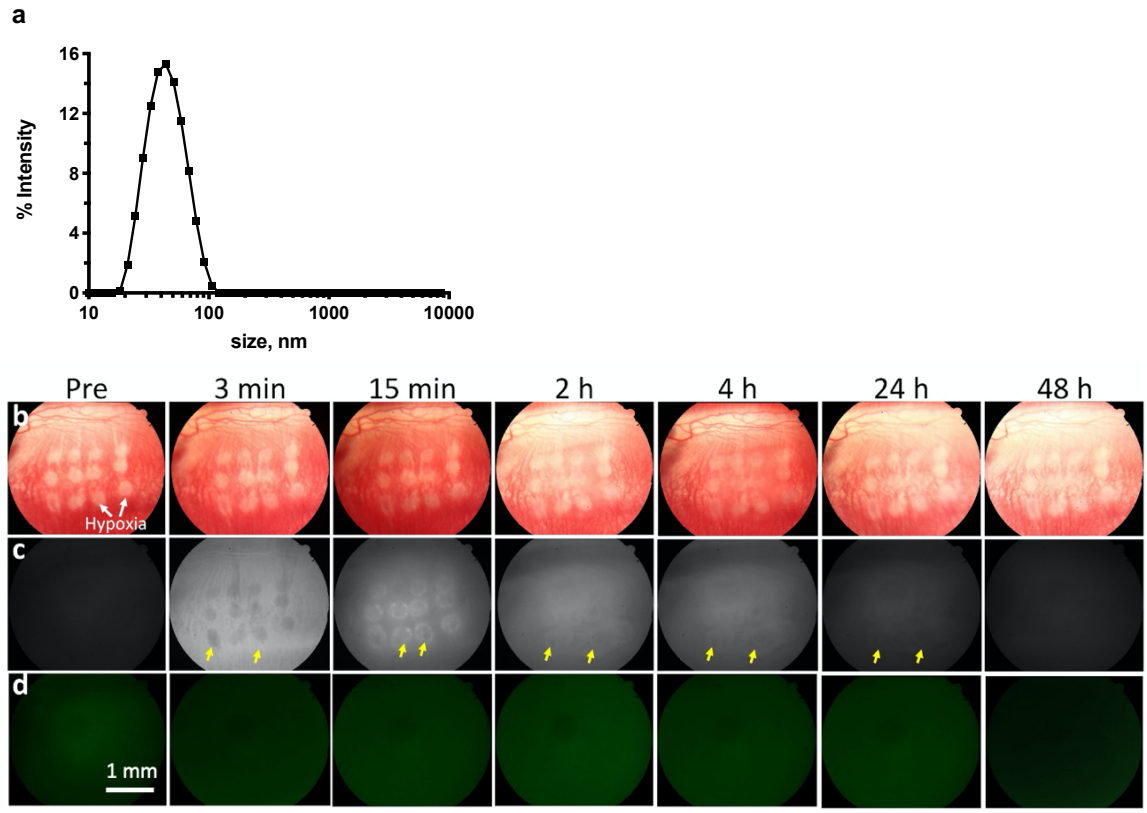

Figure 2.11 | *In vivo* hypoxia visualization of CVO in rabbits. a, hydrodynamic size distribution of IR780-LPS4VP-PEG NPs measured by dynamic light scattering. Narrow-dispersed (PDI: 0.109 ± 0.012) NPs, containing fluorescent dye IR-780 only, with an average hydrodynamic diameter of 46.3 ± 0.6 nm were synthesized using a similar nanoprecipitation procedure. **b,** Color fundus photography of the eye pre- and post-intravenous injection of IR780-LPS4VP-PEG NPs. White arrows show the local hypoxia induced by laser photocoagulation. **c,** Fluorescent images obtained after injection of 4 mL NPs (2.5 mg/mL). The treated areas were clearly observed from the leakage of NPs from occluded choroidal vessels at 15 min (yellow arows). **d,** Phosphorescence images showed no signal emitted from the NPs since no organic phosphor was incorporated in them. These results ensure that tissue autofluorescence or other noise signals will not interfere with the phosphorescence imaging settings, and the phosphorescent signal detected in CVO model injected with IR-780 and Br6A co-encapsulated RTP NPs is attributed to Br6A selectively detecting hypoxia.

To increase the clinical translatability, the *in vivo* reproducibility of choroidal hypoxia detection by Br6A-IR780-LPS4VP-PEG NPs via IV injection was verified in multiple Dutch

Belted rabbits (Figure 2.12). These RTP NPs initially clustered at the rim of laser lesions (15 min) and gradually penetrated into the center region. At 4 h, patches of RTP NPs accumulated at the center regions of laser lesions can be clearly visualized on the fluorescence channel (Figure 2.12b). Strong fluorescence signal was still detectable in both retinal and choroidal blood vessels even at 48 h post-injection, suggesting that Br6A-IR780-LPS4VP-PEG NPs exhibit prolonged blood circulation.

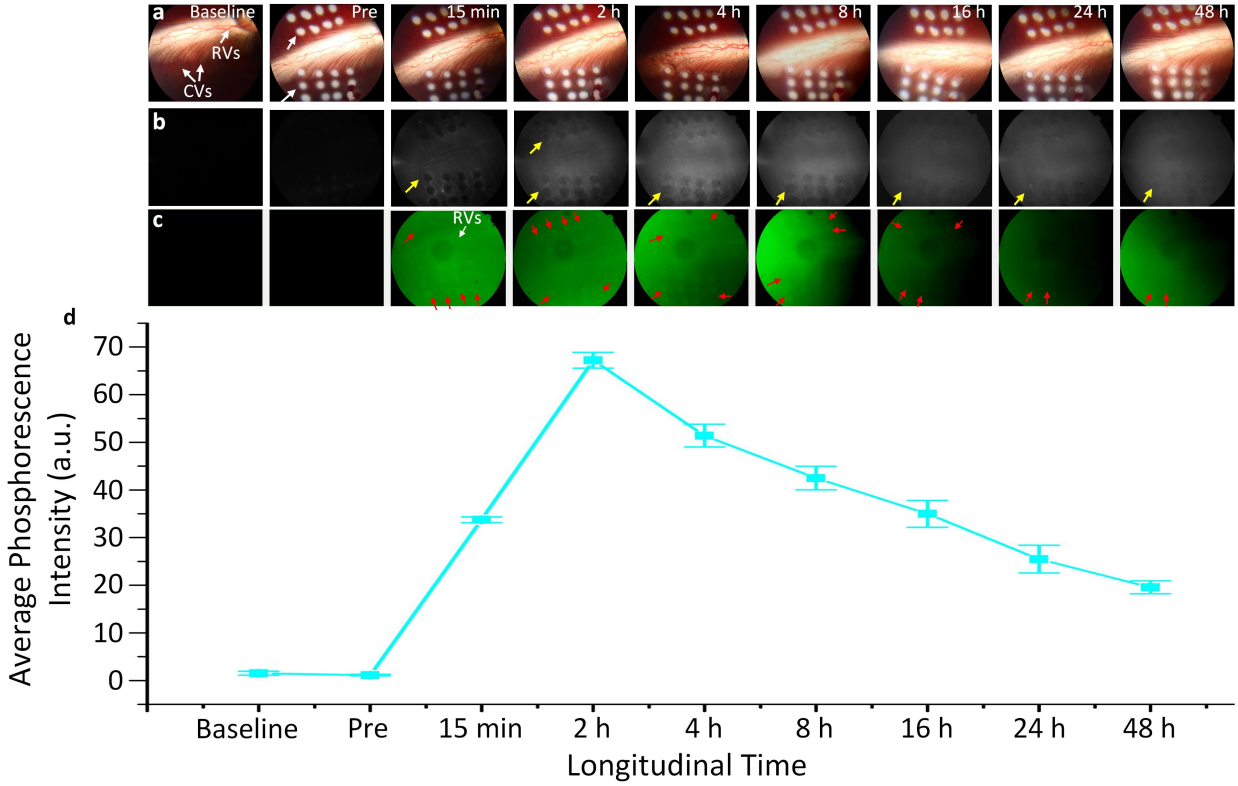

Figure 2.12 | *In vivo* multimodal visualization of retinal hypoxia in Dutch belted rabbit CVO model. a–c, Color fundus photograph (**a**), fluorescence (**b**), and phosphorescence (**c**) images of a rabbit retina before and after laser-induced choroidal vessel occlusion (white arrows), and various time points post-intravenous injection of Br6A-IR780-LPS4VP-PEG NPs (4 mL, 2.5 mg/mL). Color fundus photography images show healthy retinal vessels (RVs) and choroidal vessels (CVs) network as well as laser injured sites (white arrows). Fluorescent images indicate the RTP NPs can effectively extravasate through fenestrations in the vasculature and accumulate at laser lesions (yellow arrows). Phosphorescence images demonstrate that choroidal tissue hypoxia is visualized by RTP NPs in CVO rabbit choroids (green). **d**, Quantitative analysis of mean phosphorescence intensity at laser lesions in the choroid of CVO rabbits. Error bars show the standard deviations of three independent measurements.

2.2.6 In vivo toxicity and biosafety analysis of organic RTP NPs

To test the potential toxicity of IV and intravitreal administration of RTP NPs in these rabbits, several biosafety analyses were performed, including body weight analysis, liver function tests (LFT), kidney function tests (KFT), TUNEL assay, and histopathology. All rabbits used in this study had their weight measured daily (Figure 2.13 and 2.14). Body weight of intravenously treated, intravitreally treated, and untreated groups increased appropriately over 7 days, demonstrating that these RTP NPs do not induce negative systemic impact on living rabbits. Hematoxylin and eosin (H&E) staining demonstrates preserved normal retinal cellular morphology and nuclei without fragmentation or extracellular debris (Figure 2.13b,c and Figure 2.14b,c). TUNEL assay analysis demonstrates no evidence of cells undergoing apoptosis (Figure 2.13d and Supporting Information, Figure 2.14d). To inspect potential local inflammations post-intravitreal administration, slit lamp examination was performed and there was no evidence of intraocular inflammation, either anterior uveitis or vitritis. Serum blood tests were performed to examine the acute toxicity of RTP NPs to liver or kidney function of the animals. As shown in Table 2.1 for intravenous injection and Table 2.2 for intravitreal injection, all LFTs and KFTs are within normal range at 14 days after RTP NPs administration in all animals, indicating normal liver and kidney functions with no systemic toxicity. According to a National Institute for Occupational Safety and Health report on ocular ultraviolet effects from 295 nm to 400 nm in the rabbit eye, the effect on the lens abruptly drops at 313 nm.[60] Therefore, the excitation wavelength of 365 nm for only a short period of exposure for imaging will not likely to cause harmful effect, and indeed in our study no ocular or systemic complications were observed in the rabbit models after imaging.

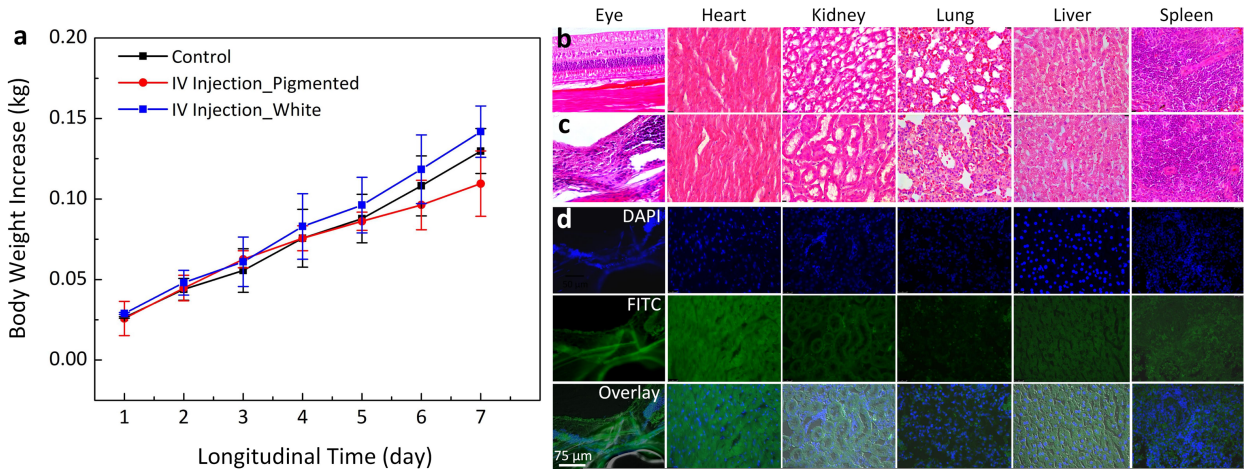

Figure 2.13 | Biosafety evaluation in living rabbits after intravenous injection. a, Body weight increase measured daily for 7 days from three different groups: untreated control and intravenously treated CVO models in White New Zealand and Dutch Belted pigmented rabbits, showing no evidence of systematic toxicity through equivalent, appropriate weight gain in both RTP NPs treated and untreated control groups. **b**,**c**, H&E staining of tissues obtained 1 month post-intravenous injection of Br6A-IR780-LPS4VP-PEG NPs (**b**) compared to the untreated control group (**c**), demonstrating preserved cellular morphology and nuclei without fragmentation or extracellular debris from dead cells in all of the evaluated organs, including eye, heart, kidney, lung, liver, and spleen. **d**, TUNEL assay analysis at 1-month post-intravenous injection of Br6A-IR780-LPS4VP-PEG NPs. DAPI (blue) indicates cell nuclei. Green color stained with FITC evaluates for any potentially apoptotic cells, which are not noted. Scale bar: 75 μm.

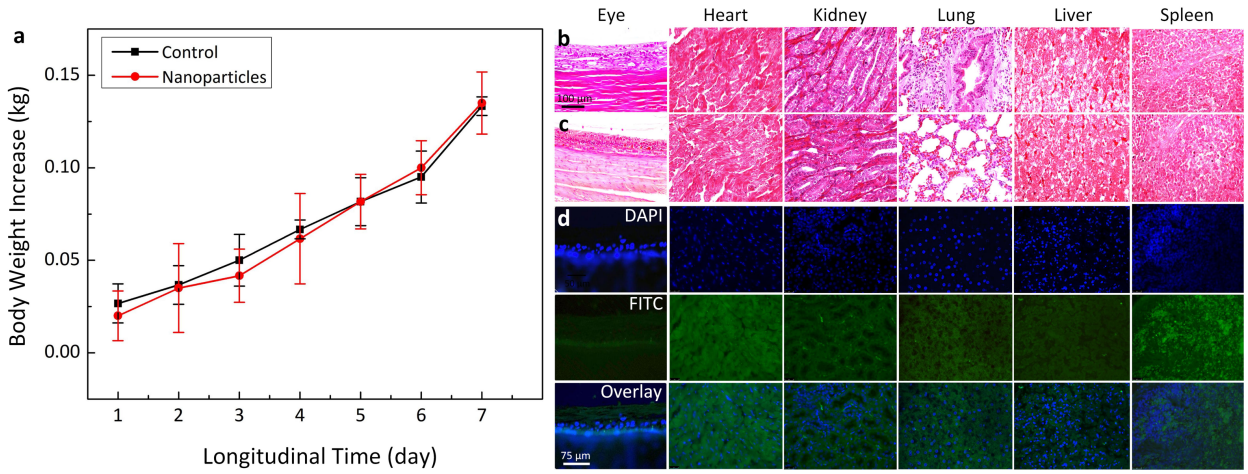

Figure 2.14 | Biosafety evaluation in living rabbits after intravitreal injection. a, Body weight increase of untreated control and RTP NPs treated RVO model in White New Zealand rabbits via intravitreal injection measured daily for 7 days. The results show that rabbit weights are gradually increased at similar rates for both treated and untreated groups, indicating no evidence of systematic toxicity caused by RTP NPs via intravitreal injection. **b**,**c**, H&E images of tissues after intravitreal injection of Br6A-LPS4Br NPs (b) compared to the untreated control group (c). Scale bar: 100 μm. **d**, TUNEL assay analysis. DAPI (blue) indicates cell nuclei. Green color stained with FITC evaluates for any potentially apoptotic cells, which are not noted. Scale bar: 75 μm.

Table 2.1 | Liver and Kidney Function tests at 14 days post-administration for untreated control and intravenously treated choroidal vascular occlusion model in New Zealand white and Dutch Belted pigmented rabbits, demonstrating normal liver and kidney function tests

			Br6A-IR780-LPS4VP-PEG			**Control**
Liver Function Tests (LFT)	**Normal Range**	**Unit**	**NZ White Rabbit**	**Pigmented Rabbit #1**	**Pigmented Rabbit #2**	**NZ White Rabbit**
Albumin	2.7–5	g/dL	3.7	4.1	4.2	4.0 ± 0.3
Total Protein (TPRO)	5–7.5	g/dL	5.3	6	6.2	5.8 ± 0.5
Alanine aminotransferase (ALT)	25–65	U/L	35	43	41	39.7 ± 4.2
Alkaline phosphatase (ALP)	10.0–86.0	U/L	76	86	66	76.0 ± 10.0
Total Bilirubin (TBIL)	0.2–0.5	mg/dL	0.4	0.3	0.2	0.3 ± 0.1
Kidney Function Tests (KFT)						
Blood urea nitrogen (BUN)	5.0–25.0	mg/dL	15	21	21	19 ± 3.5
Creatinine (CREA)	0.5–2.6	mg/dL	0.67	0.68	1.11	0.8 ± 0.2
Calcium	5.6–12.1	mg/dL	12.0	14	12.9	13.0 ± 1.0
Glucose	74–148	mg/dL	137	111	189	145.7 ± 39.7

Table 2.2 | Liver and Kidney Function tests obtained 14 days after intravitreal injection of Br6A-LPS4Br NPs. All values for both untreated control and RTP NPs treated groups are within normal limits.

Liver Function Tests (LFT)	**Normal Range**	**Unit**	**Control**	**Treated #1**	**Treated #2**	**Treated #3**
Albumin	2.7–5	g/dL	4.2	3.4	3.5	3
Total Protein (TPRO)	5–7.5	g/dL	6.6	6.7	5	7.3
Alanine aminotransferase (ALT)	25–65	U/L	31	25	51	29
Alkaline phosphatase (ALP)	10.0–86.0	U/L	77	81	51	85
Total Bilirubin (TBIL)	0.2–0.5	mg/dL	0.4	0.3	0.33	0.22
Kidney Function Tests (KFT)						
Blood urea nitrogen (BUN)	5.0–25.0	mg/dL	25	20	15	17
Creatinine (CREA)	0.5–2.6	mg/dL	1.35	0.68	0.78	0.74
Calcium	5.6–12.1	mg/dL	11.2	11.4	11.7	9.7
Glucose	74–148	mg/dL	102	122	133	114

2.3 Conclusion and Outlook

In this work, we have successfully developed a versatile lipid-polymer hybrid assembly platform to generate efficient metal-free organic RTP NPs for longitudinal optical visualization of chorioretinal tissue hypoxia in living rabbits in a non-destructive fashion. The facile nanoformulation involves (1) a rigid and oxygen-permeable polymer core for the effective activation of bright RTP from the embedded organic phosphor in hypoxic environments, and (2) an amphiphilic phospholipid shell, allowing for excellent water dispersity, biocompatibility, and colloidal stability. The phosphorescent signal of the fabricated organic RTP NPs demonstrates milliseconds decay time and is highly responsive toward oxygen quenching, which enables them to be exploited as “turn-on” imaging probes for chorioretinal tissue hypoxia. When tested *in vivo*

using rabbit RVO and CVO models, both oxygen-sensing efficacy and biosafety of the organic RTP NPs were demonstrated. The phosphorescence signal was exclusively generated with high SNR in the RVO side or laser lesions in the CVO side of the rabbit eye where tissue hypoxia was present. Specifically, when administrated intravenously in rabbit CVO model, the RTP NPs exhibited prolonged blood circulation and were able to effectively accumulate at target laser lesions in the choroid and detect focal tissue hypoxia. The fluorescent dye and organic phosphor co-encapsulated NPs showed co-localization of fluorescence and phosphorescence signals via multimodal imaging, confirming the hyperphosphorescence in both RVO and CVO models originates from organic RTP NPs in response to tissue hypoxia. No ocular or systemic complications or toxicity were noted after either intravenous or intravitreal administration of RTP NPs. These data provide proof-of-concept that the developed nanoformulation of organic RTP materials allows for biocompatible, non-destructive detection of hypoxia in chorioretinal tissue, currently unachievable by other methods.

The oxygen sensitivity of these organic RTP NPs can be optimized for visualizing the hypoxia in the retina and choroid by tuning the host polymer's oxygen permeability. If the oxygen sensing window of the current nanoformulation falls outside of the clinically-relevant range for retinal and choroidal tissue hypoxia, the chemical composition of RTP NPs' polymeric core can be tuned to modulate its oxygen sensitivity and detection range. For example, poly(methyl methacrylate) (PMMA), particularly isotactic PMMA, is known to have low permeability toward oxygen[35,43,61]. Therefore, a mixture of PS4VP and PMMA of different compositions can be used to encapsulate Br6A.

While further studies will be conducted to assess this RTP nanosensor's hypoxia detection window, *in vivo* oxygen tension determination, and pharmacokinetics, the results of this work provide a strong indication that the developed organic RTP NPs hold significant promise as an advanced non-invasive imaging tool for long-term visualization of tissue oxygen levels and evaluation of various hypoxia-driven vascular diseases. Since the light-generating mechanism of the organic phosphor Br6A in response to oxygen tension is at molecular scale, and RTP particles are at nanoscale, it is reasonable to anticipate high spatial resolution (nanoscale) for *in vivo* hypoxia imaging, though in practice the resolution will be limited to around 5 μm due to optical resolution in the eye without adaptive optics. This study lays a solid foundation demonstrating that this organic RTP nanosensor has a great potential to serve as a general tissue hypoxia tracking probe via minimally invasive systemic delivery, beyond the retina and choroid.

2.4 Experimental Section

2.4.1 Materials

Reagents used to synthesize the organic phosphor Br6A were purchased from Millipore Sigma. Phospholipids 1,2-dimyristoyl-sn-glycero-3-phosphate (DMPA) and 1,2-distearoyl-sn-glycero-3-phosphoethanolamine-N-[carboxy(polyethylene glycol)-2000] (DSPE-PEG2000) were purchased from Avanti Polar Lipids. Polystyrene-*b*-poly(4-vinylpyridine) (PS4VP) was purchased from Polymer Source. Other chemicals and materials such as IR-780 iodide, poly(4-bromostyrene) (PS4Br, M_w ~65,000), solvents, and Amicon® Ultra-4 centrifugal filters (MWCO 30 kD) were also purchased from Millipore Sigma. Malvern Panalytical folded capillary zeta cells were purchased from Fisher Scientific.

2.4.2 Preparation of lipid-polymer hybrid organic RTP NPs for intravitreal injection

The metal-free organic phosphor, Br6A was synthesized according to a published procedure from our lab,[41] and its purity was confirmed by ^{1}H NMR. The lipid-polymer hybrid NPs containing the organic phosphor were fabricated by a single-step nanoprecipitation method. To prepare Br6A-LPS4Br NPs, phospholipid DMPA was dispersed into 4 wt% ethanol-water solution at a concentration of 0.15 mg/mL (15 wt% to PS4Br) as the aqueous outer phase. The dispersion was then heated up to 65 °C until the solution became completely transparent to ensure that all the lipids were in the liquid phase. A stock solution of 10 mg/mL PS4Br mixed with Br6A (5 wt% to PS4Br) was prepared in tetrahydrofuran (THF) as the organic internal phase. Then 1 mL of this THF mixture solution was rapidly injected into the aqueous outer phase with vigorous stirring. The resulting suspension was subsequently sonicated for 10 min using a bath sonicator (Bransonic 2510-DTH) at a frequency of 42 kHz and power of 100 W. It was then further stirred at room temperature for 30 h to allow for the complete evaporation of organic solvents. Purification was done by washing the NPs in Milli-Q water 3 times using Amicon® Ultra-4 centrifugal filters with a molecular weight cutoff of 30 kD. The purified Br6A-LPS4Br NPs were re-suspended in Milli-Q water to make 2.5 mg/mL stock concentration. The fluorescent dye co-encapsulated Br6A-IR780-LPS4Br NPs were synthesized using a similar procedure except when mixing PS4Br with organic phosphor Br6A, IR-780 iodide (stock solution prepared in acetone at 1mg/mL) was also added at 2 wt% to PS4Br.

2.4.3 Preparation of lipid-polymer hybrid organic RTP NPs for intravenous injection

To prepare Br6A-IR780-LPS4VP-PEG NPs for intravenous administration, PS4VP was used as the polymer matrix instead of PS4Br, and DSPE-PEG2000 (30 wt% to PS4VP) was used

as the phospholipid instead of DMPA. To make 1 mL of the organic internal phase containing polymer, organic phosphor (5 wt% to polymer), and fluorescent dye (2 wt% to polymer), 400 μL THF was used to dissolve 10 mg of PS4VP, followed by adding 100 μL of Br6A stock in THF at 5 mg/mL and 200 μL of IR-780 iodide stock in acetone at 1mg/mL. Then 300 μL of acetone was added to the mixture to adjust the volume ratio of THF and acetone (1:1). The rest of the steps were similar to the nanoprecipitation procedure described above.

2.4.4 Characterization of lipid-polymer hybrid organic RTP NPs

Hydrodynamic size (diameter, nm), PDI, and surface charge (ζ potential, mV) of the lipid-polymer hybrid NPs were measured in Milli-Q water on Malvern Zetasizer Nano ZSP (Model number: ZEN5600) using disposable cuvettes and folded capillary zeta cells, respectively. All measurements were conducted at a backscattering angle of 173° (NIBS default) at 25 °C. Size and polydispersity analyses were performed using Malvern Zetasizer software (Ver. 7.11). The average hydrodynamic diameters of NPs are reported using the peak means of size distribution plots by intensity. Particle size and morphology were further examined by SEM (Thermo Fisher Nova 200 Nanolab) after carbon coating. Photophysical properties including steady state emission and excitation spectra, delayed emission, lifetime, and absolute quantum yield were measured using a Photo Technologies International (PTI) QuantaMaster spectrofluorometer equipped with an integrating sphere. Anoxic aqueous suspensions of RTP NPs were prepared by bubbling argon gas through sample solutions placed in rubber septum-capped quartz cuvettes for 30 min. Then to achieve various pO_2 (0–21%) in the aqueous suspension, different amount of air was refilled back into the anoxic sample. All experiments were performed in triplicate from freshly prepared samples (n = 3). Data are expressed as the mean ± standard deviation.

2.4.5 Animal model preparation

All animal studies were implemented under the guidelines of the Association for Research in Vision and Ophthalmology (ARVO) Statement on the Care and Use of Laboratory Animals in Ophthalmic and Vision Research. The experimental protocol was approved by the Institutional Animal Care and Use Committee (IACUC) of the University of Michigan (Protocol number: PRO00008566, PI: Y. Paulus).

A total of 11 rabbits were used in this study. Nine New Zealand white rabbits (2–4 months and 2.5–3.0 kg) were obtained from the Center for Advanced Models and Translational Sciences and Therapeutics (CAMTraST) at the University of Michigan Medical School, and two Dutch Belted rabbits (3 months and 1.3–1.5 kg) were purchased from Covance. The animals were divided into three groups: control, RVO, and choroidal vascular occlusion (CVO). In the RVO control group, the animals received intravitreal injection of organic RTP NPs (50 μL, 2.5 mg/mL) and had normal, healthy retinas. In the RVO group, the animals received hemi-retinal vein occlusion (RVO) by Rose Bengal dye-enhanced photochemical thrombosis laser photocoagulation. In the CVO group, the rabbits were treated with laser photocoagulation without administration of Rose Bengal. Throughout experiments and recovery, the animal condition including mucous membrane color, body temperature, heart rate, and respiratory rate was recorded and documented every 15 minutes. To induce anesthesia, a dose of ketamine (40 mg/kg) and xylazine (5 mg/kg) was injected intramuscularly (IM). The rabbit's pupils were dilated using tropicamide 1% and phenylephrine 2.5% ophthalmic. A drop of 0.5% tetracaine was applied for topical anesthesia before experiments. In addition, lubricant (Systane, Alcon Inc., TX, USA) was provided every minute to avoid corneal dehydration during experiments. To maintain the animal's body temperature, a water-circulating heating blanket was used.

2.4.6 RVO model generation

RVO model was generated using Rose Bengal dye-enhanced photochemical thrombosis as described in detail in previous studies.[50,51,62] Briefly, a 532 nm green light laser mounted on a slit lamp was used to create the RVO model (Vitra 532 nm, Quantel Medical, Cournon d'Auvergne, France). To visualize the target retina vessels, a contact lens (Volk H-R Wide Field, laser spot 2x magnification, Volk Optical Inc, Mentor, OH, USA) was placed on the cornea. Rabbits under anesthesia were injected IV with Rose Bengal (50 mg/mL). 5–10 seconds after the injection, 20 spots of 532 nm laser at a power of 150 mW, aerial spot diameter of 75 μm, and pulse duration of 500 ms were illuminated at the same position at a distance of one-half to one disc diameter from the optic nerve to avoid optic neuropathy.[63] To avoid reperfusion, 20 laser spots were further applied with a power of 300 mW. The treated position on the veins was carefully selected to prevent damaging the adjacent arteries or optic nerve.[64]

2.4.7 CVO model generation

To induce CVO model, a contact lens was placed on the cornea of the rabbit eye. Gonak Hypromellose Ophthalmic Demulcent Solution 2.5% was placed on the surface of the contact lens for coupling. The rabbit eye was irradiated with a 532 nm green light laser at a power of 450 mW, aerial beam diameter of 150 μm, and pulse duration of 500 ms using a Zeiss SL 130 slit lamp (Carl Zeiss Meditec, Jena, Germany), to which the Vitra photocoagulator was connected. Fifteen shots of the laser were illuminated into the eye at different positions. To create CVO model in Dutch Belted rabbits, the laser power was reduced from 450 mW to 300 mW due to melanin absorption. Twelve spots were illuminated on the retina with aerial spot size of 150 μm and pulse duration of 500 ms. After taking color fundus photographs, fluorescein angiography (FA) and indocyanine

green angiography (ICGA) were performed to evaluate the vasculature and confirm vascular occlusion.

2.4.8 Follow-up RVO and CVO evaluation

All rabbits with RVO model were examined fifteen minutes after the laser treatment, and at day 7 and day 14 post-photocoagulation. The rabbit models were assessed by color fundus photography, fluorescein angiography (FA), indocyanine green (ICG) angiography, and phosphorescence photography.

2.4.9 Color fundus photography

All retinal vessel network and laser-induced hypoxia were imaged using a custom-modified 50-degree color fundus photography (Topcon 50EX, Topcon Corporation, Tokyo, Japan). The digital images were captures by EOS 5D camera with a resolution of 5472×3648 pixels with a pixel size of 6.55 μm^2. Color fundus images were obtained using the maximum 50-degree angle of coverage centered at five different positions of the eye: the optic nerve, the superior retina above the optic disc, the inferior retina below the optic disc, the temporal medullary ray, and the nasal medullary ray. Color fundus montages were created using the I2K Retina software (Topcon Corporation, Tokyo, Japan).

2.4.10 Fluorescein angiography and indocyanine green angiography

FA and ICGA were performed on the Topcon 50EX camera by changing the camera's appropriate internal excitation and emission filters for each. For FA, a dose of 0.2 mL fluorescein sodium at a concentration of 10% fluorescein (Akorn, Lake Forest, IL, USA) was intravenously

injected into the rabbit via the marginal ear vein. For ICGA, 2.0 mL of ICG solution at concentration of 2.5 mg/mL (Akorn, Lake Forest, IL, USA) was injected intravenously via the marginal ear vein. FA and ICGA images were subsequently acquired after fluorophore injection, and late phase FA and ICGA images were acquired at every minute for a period of at least 20 minutes.

2.4.11 Phosphorescence photography examinations

To evaluate the potential of organic RTP NPs as an oxygen sensor for detection of hypoxia *in vivo*, phosphorescence photography was evaluated on rabbit models using a custom-modified Topcon 50EX camera with custom-made filters (excitation filter with the bandpass wavelengths of 335 to 379 nm (FF01-357/44, Semrock, NY, USA) and barrier filter with a bandpass of 498 to 542 nm (FF01-520/44, FF01-357/44, Semrock, NY, USA) and UV-excitation light source (4.4 x 10^{-4} W/cm^2) with center wavelength of 365 nm and bandwidth of 9 nm (M365LP1, Thorlabs, USA). All rabbits with the RVO model received intravitreal injection of 50 µL organic RTP NPs at a concentration of 2.5 mg/mL. Phosphorescent photography was acquired immediately after the injection and follow-ups for different time points: 15 min, 1, 2, 4, 8, 24 h and day 2, 4, and 7. For intravenous injection, the rabbits with CVO model were injected with 4 mL of RTP NPs at a concentration of 2.5 mg/mL. Phosphorescent imaging was acquired immediately after the injection and follow-ups for different time points: 15 min, 2, 4, 8, 16, 24 h, 48 h and day 7. It took about 2 seconds to capture each fundus phosphorescence image of the rabbit models. The control groups were monitored over a period of 17 days post-injection. The dynamic changes of phosphorescent signal over time were determined by region of interest (ROI) using ImageJ software.

2.4.12 Biosafety analysis

Biosafety analysis was performed on the treated animals using different methods such as body weight analysis, hematoxylin and eosin (H&E) staining, TUNEL assay, liver function test (LFTs), and kidney function tests (KFTs). Body weight was measured daily post administration of RTP NPs for each group over a period of 7 days. At day 14 after injection of RTP NPs, 400 µL of blood sample was collected from each rabbit for LFTs and KFTs. Then, the rabbits were euthanized by intravenous injection of euthanasia solution (0.22 mg/kg) via the marginal ear vein (Beuthanasia-D Special, Intervet Inc., Madison, NJ, USA). The organs and eye tissues were harvested and fixed with 10% neutral buffered formalin (VWR, Radnor, PA, USA). To prevent retinal detachment, eye tissues were fixed with Davidson's fixative solution (Electron Microscope Sciences, PA, USA) for 24 h. Afterwards, the samples were placed in 50% alcohol solution for 8 h and then replaced with 70% alcohol solution and kept at room temperature for 24 h. The fixed tissues were embedded in paraffin, sectioned into 6 µm thick sections, and stained with hematoxylin and eosin (H&E) for histopathological examination. TUNEL assay analysis were performed using TUNEL in situ Cell Death Detection Kit protocol (Sigma-Aldrich, USA). The stained slides were analyzed using DM6000 microscope. H&E images were captured using the BF450C camera and TUNEL fluorescence images were obtained using the FF363x camera (DM600, Leica Biosystems, Nussloch, Germany).

2.5 References

1. Rehak, J.; Rehak, M. Branch retinal vein occlusion: Pathogenesis, visual prognosis, and treatment modalities. *Curr. Eye Res.* **2008,** *33* (2), 111-131.
2. Gariano, R. F.; Gardner, T. W. Retinal angiogenesis in development and disease. *Nature* **2005,** *438* (7070), 960-966.

3. Campochiaro, P. A. Molecular pathogenesis of retinal and choroidal vascular diseases. *Prog. Retin. Eye Res.* **2015,** *49*, 67-81.

4. Tsuiki, E.; Suzuma, K.; Ueki, R.; Maekawa, Y.; Kitaoka, T. Enhanced depth imaging optical coherence tomography of the choroid in central retinal vein occlusion. *Am. J. Ophthalmol.* **2013,** *156* (3), 543-547 e1.

5. Hayreh, S. S. Ocular vascular occlusive disorders. In *Ocular vascular occlusive disorders*, Springer International Publishing: Berlin, Germany, 2015; pp pp. 379-427.

6. Hayreh, S. S. Ocular vascular occlusive disorders: Natural history of visual outcome. *Progress in retinal and eye research* **2014,** *41*, 1-25.

7. Rogers, S.; McIntosh, R. L.; Cheung, N.; Lim, L.; Wang, J. J.; Mitchell, P.; Kowalski, J. W.; Nguyen, H.; Wong, T. Y.; Consortium, I. E. D. The prevalence of retinal vein occlusion: Pooled data from population studies from the united states, europe, asia, and australia. *Ophthalmology* **2010,** *117* (2), 313-319. e1.

8. Li, J.; Paulus, Y. M.; Shuai, Y.; Fang, W.; Liu, Q.; Yuan, S. New developments in the classification, pathogenesis, risk factors, natural history, and treatment of branch retinal vein occlusion. *J. Ophthalmol.* **2017,** *2017*, 4936924.

9. Ashton, N. Pathological basis of retrolental fibroplasia. *Br. J. Ophthalmol.* **1954,** *38* (7), 385.

10. Feenstra, D. J.; Drawnel, F. M.; Jayagopal, A. Imaging of hypoxia in retinal vascular disease. *Early Events in Diabetic Retinopathy and Intervention Strategies* **2018**, 47.

11. Cringle, S. J.; Yu, D.-Y.; Paula, K. Y.; Su, E.-N. Intraretinal oxygen consumption in the rat in vivo. *Investig. Ophthalmol. Vis. Sci.* **2002,** *43* (6), 1922-1927.

12. Berkowitz, B. A.; McDonald, C.; Ito, Y.; Tofts, P. S.; Latif, Z.; Gross, J. Measuring the human retinal oxygenation response to a hyperoxic challenge using mri: Eliminating blinking artifacts and demonstrating proof of concept. *Magnetic Resonance in Medicine: An Official Journal of the International Society for Magnetic Resonance in Medicine* **2001,** *46* (2), 412-416.

13. Stefánsson, E.; Olafsdottir, O. B.; Eliasdottir, T. S.; Vehmeijer, W.; Einarsdottir, A. B.; Bek, T.; Torp, T. L.; Grauslund, J.; Eysteinsson, T.; Karlsson, R. A.; Van Keer, K.; Stalmans, I.; Vandewalle, E.; Todorova, M. G.; Hammer, M.; Garhöfer, G.; Schmetterer, L.; Šín, M.; Hardarson, S. H. Retinal oximetry: Metabolic imaging for diseases of the retina and brain. *Prog. Retin. Eye Res.* **2019,** *70*, 1-22.

14. Aouiss, A.; Anka Idrissi, D.; Kabine, M.; Zaid, Y. Update of inflammatory proliferative retinopathy: Ischemia, hypoxia and angiogenesis. *Curr. Res. Transl. Med.* **2019,** *67* (2), 62-71.

15. Gu, L.; Xu, H.; Zhang, C.; Yang, Q.; Zhang, L.; Zhang, J. Time-dependent changes in hypoxia- and gliosis-related factors in experimental diabetic retinopathy. *Eye (Lond.)* **2019,** *33* (4), 600-609.

16. Shimazaki, T.; Hirooka, K.; Nakano, Y.; Nitta, E.; Ukegawa, K.; Tsujikawa, A. Oxygen venular saturation correlates with a functional loss in primary open-angle glaucoma and normal-tension glaucoma patients. *Acta Ophthalmol. (Copenh.)* **2018,** *96* (3), e304-e308.

17. Felder, A. E.; Wanek, J.; Tan, M. R.; Blair, N. P.; Shahidi, M. A method for combined retinal vascular and tissue oxygen tension imaging. *Sci. Rep.* **2017,** *7* (1), 10622.

18. Blumenroder, S.; Augustin, A. J.; Koch, F. H. The influence of intraocular pressure and systemic oxygen tension on the intravascular po2 of the pig retina as measured with phosphorescence imaging. *Surv. Ophthalmol.* **1997,** *42 Suppl 1*, S118-26.

19. Wanek, J.; Teng, P.-y.; Albers, J.; Blair, N. P.; Shahidi, M. Inner retinal metabolic rate of oxygen by oxygen tension and blood flow imaging in rat. *Biomed. Opt. Express* **2011,** *2* (9), 2562-2568.

20. Zhao, W.; He, Z.; Tang, B. Z. Room-temperature phosphorescence from organic aggregates. *Nat. Rev. Mater.* **2020**.

21. Ma, X.; Wang, J.; Tian, H. Assembling-induced emission: An efficient approach for amorphous metal-free organic emitting materials with room temperature phosphorescence. *Acc. Chem. Res.* **2019,** *52* (3), 738-748.

22. Kenry; Chen, C.; Liu, B. Enhancing the performance of pure organic room-temperature phosphorescent luminophores. *Nat. Commun.* **2019,** *10* (1), 2111.

23. Ma, H.; Lv, A.; Fu, L.; Wang, S.; An, Z.; Shi, H.; Huang, W. Room-temperature phosphorescence in metal-free organic materials. *Annalen der Physik* **2019,** *531* (7), 1800482.

24. Gan, N.; Shi, H. F.; An, Z. F.; Huang, W. Recent advances in polymer-based metal-free room-temperature phosphorescent materials. *Adv. Funct. Mater.* **2018,** *28* (51), 1802657.

25. Papkovsky, D. B.; Dmitriev, R. I. Biological detection by optical oxygen sensing. *Chem. Soc. Rev.* **2013,** *42* (22), 8700-32.

26. Hirata, S.; Totani, K.; Zhang, J. X.; Yamashita, T.; Kaji, H.; Marder, S. R.; Watanabe, T.; Adachi, C. Efficient persistent room temperature phosphorescence in organic amorphous materials under ambient conditions. *Adv. Funct. Mater.* **2013,** *23* (27), 3386-3397.

27. Vanderkooi, J. M.; Maniara, G.; Green, T. J.; Wilson, D. F. An optical method for measurement of dioxygen concentration based upon quenching of phosphorescence. *J. Biol. Chem.* **1987,** *262* (12), 5476-5482.

28. Schulman, E. M.; Parker, R. T. Room-temperature phosphorescence of organic-compounds - effects of moisture, oxygen, and nature of support-phosphor interaction. *J. Phys. Chem.* **1977,** *81* (20), 1932-1939.

29. Zang, L.; Shao, W.; Kwon, M. S.; Zhang, Z.; Kim, J. Photoresponsive luminescence switching of metal-free organic phosphors doped polymer matrices. *Adv. Optical Mater.* **2020,** *8*, 2000654.

30. Yu, Y.; Kwon, M. S.; Jung, J.; Zeng, Y.; Kim, M.; Chung, K.; Gierschner, J.; Youk, J. H.; Borisov, S. M.; Kim, J. Room-temperature-phosphorescence-based dissolved oxygen detection by core-shell polymer nanoparticles containing metal-free organic phosphors. *Angew. Chem. Int. Ed.* **2017,** *56* (51), 16207-16211.

31. Esipova, T. V.; Barrett, M. J. P.; Erlebach, E.; Masunov, A. E.; Weber, B.; Vinogradov, S. A. Oxyphor 2p: A high-performance probe for deep-tissue longitudinal oxygen imaging. *Cell Metab.* **2019,** *29* (3), 736-744 e7.

32. Rai, M.; Ingle, A. P.; Medici, S. *Biomedical applications of metals*. Springer: Cham, 2018; p xviii, 325 pages.

33. Kwon, M. S.; Yu, Y.; Coburn, C.; Phillips, A. W.; Chung, K.; Shanker, A.; Jung, J.; Kim, G.; Pipe, K.; Forrest, S. R.; Youk, J. H.; Gierschner, J.; Kim, J. Suppressing molecular motions for enhanced room-temperature phosphorescence of metal-free organic materials. *Nat. Commun.* **2015,** *6*, 8947.

34. Kwon, M. S.; Lee, D.; Seo, S.; Jung, J.; Kim, J. Tailoring intermolecular interactions for efficient room-temperature phosphorescence from purely organic materials in amorphous polymer matrices. *Angew Chem Int Ed* **2014,** *53* (42), 11177-81.

35. Lee, D.; Bolton, O.; Kim, B. C.; Youk, J. H.; Takayama, S.; Kim, J. Room temperature phosphorescence of metal-free organic materials in amorphous polymer matrices. *J. Am. Chem. Soc.* **2013,** *135* (16), 6325-6329.

36. DeRosa, C. A.; Seaman, S. A.; Mathew, A. S.; Gorick, C. M.; Fan, Z.; Demas, J. N.; Peirce, S. M.; Fraser, C. L. Oxygen sensing difluoroboron beta-diketonate polylactide materials with tunable dynamic ranges for wound imaging. *ACS Sens.* **2016,** *1* (11), 1366-1373.

37. Samonina-Kosicka, J.; Weitzel, D. H.; Hofmann, C. L.; Hendargo, H.; Hanna, G.; Dewhirst, M. W.; Palmer, G. M.; Fraser, C. L. Luminescent difluoroboron beta-diketonate peg-pla oxygen nanosensors for tumor imaging. *Macromol. Rapid Commun.* **2015,** *36* (7), 694-9.

38. Kersey, F. R.; Zhang, G. Q.; Palmer, G. M.; Dewhirst, M. W.; Fraser, C. L. Stereocomplexed poly(lactic acid)-poly(ethylene glycol) nanoparticles with dual-emissive boron dyes for tumor accumulation. *ACS Nano* **2010,** *4* (9), 4989-4996.

39. Zhang, G.; Palmer, G. M.; Dewhirst, M. W.; Fraser, C. L. A dual-emissive-materials design concept enables tumour hypoxia imaging. *Nat. Mater.* **2009,** *8* (9), 747-51.

40. Schubert, S.; Delaney, J. T.; Schubert, U. S. Nanoprecipitation and nanoformulation of polymers: From history to powerful possibilities beyond poly(lactic acid). *Soft Matter* **2011,** *7* (5), 1581-1588.

41. Bolton, O.; Lee, K.; Kim, H. J.; Lin, K. Y.; Kim, J. Activating efficient phosphorescence from purely organic materials by crystal design. *Nat. Chem.* **2011,** *3* (3), 205-10.

42. Siracusa, V. Food packaging permeability behaviour: A report. *Int. J. Polym. Sci.* **2012**, 302029.

43. Miller, K. S.; Krochta, J. M. Oxygen and aroma barrier properties of edible films: A review. *Trends Food Sci. Technol.* **1997,** *8* (7), 228-237.

44. Li, J.; Wang, X. L.; Zhang, T.; Wang, C. L.; Huang, Z. J.; Luo, X.; Deng, Y. H. A review on phospholipids and their main applications in drug delivery systems. *Asian J. Pharm. Sci.* **2015,** *10* (2), 81-98.

45. Shah, R.; Eldridge, D.; Palombo, E.; Harding, I. Physicochemical stability. In *Lipid nanoparticles: Production, characterization and stability*, Springer: Cham, 2015; pp 75-97.

46. Mandal, B.; Mittal, N. K.; Balabathula, P.; Thoma, L. A.; Wood, G. C. Development and in vitro evaluation of core-shell type lipid-polymer hybrid nanoparticles for the delivery of erlotinib in non-small cell lung cancer. *Eur. J. Pharm. Sci.* **2016,** *81*, 162-171.

47. Mandal, B.; Bhattacharjee, H.; Mittal, N.; Sah, H.; Balabathula, P.; Thoma, L. A.; Wood, G. C. Core-shell-type lipid-polymer hybrid nanoparticles as a drug delivery platform. *Nanomedicine* **2013,** *9* (4), 474-491.

48. Fang, R. H.; Aryal, S.; Hu, C. M. J.; Zhang, L. F. Quick synthesis of lipid-polymer hybrid nanoparticles with low polydispersity using a single-step sonication method. *Langmuir* **2010,** *26* (22), 16958-16962.

49. Zhang, L. F.; Chan, J. M.; Gu, F. X.; Rhee, J. W.; Wang, A. Z.; Radovic-Moreno, A. F.; Alexis, F.; Langer, R.; Farokhzad, O. C. Self-assembled lipid-polymer hybrid nanoparticles: A robust drug delivery platform. *ACS Nano* **2008,** *2* (8), 1696-1702.

50. Nguyen, V. P.; Li, Y.; Zhang, W.; Wang, X.; Paulus, Y. M. High-resolution multimodal photoacoustic microscopy and optical coherence tomography image-guided laser induced branch retinal vein occlusion in living rabbits. *Scientific reports* **2019,** *9* (1), 1-14.

51. Nguyen, V. P.; Li, Y.; Zhang, W.; Wang, X.; Paulus, Y. M. Multi-wavelength, en-face photoacoustic microscopy and optical coherence tomography imaging for early and selective detection of laser induced retinal vein occlusion. *Biomed Opt Express* **2018,** *9* (12), 5915-5938.

52. Blanco, E.; Shen, H.; Ferrari, M. Principles of nanoparticle design for overcoming biological barriers to drug delivery. *Nat. Biotechnol.* **2015,** *33* (9), 941-51.

53. Choi, H. S.; Liu, W.; Misra, P.; Tanaka, E.; Zimmer, J. P.; Itty Ipe, B.; Bawendi, M. G.; Frangioni, J. V. Renal clearance of quantum dots. *Nat. Biotechnol.* **2007,** *25* (10), 1165-70.

54. Diaz-Coranguez, M.; Ramos, C.; Antonetti, D. A. The inner blood-retinal barrier: Cellular basis and development. *Vision Res.* **2017,** *139*, 123-137.

55. Kusuhara, S.; Fukushima, Y.; Ogura, S.; Inoue, N.; Uemura, A. Pathophysiology of diabetic retinopathy: The old and the new. *Diabetes Metab. J.* **2018,** *42* (5), 364-376.

56. Shieh, J.; Chung, T. Gas permeability, diffusivity, and solubility of poly(4-vinylpyridine) film. *Journal of Polymer Science Part B* **1999,** *37*, 2851-2861.

57. Suk, J. S.; Xu, Q. G.; Kim, N.; Hanes, J.; Ensign, L. M. Pegylation as a strategy for improving nanoparticle-based drug and gene delivery. *Adv. Drug Deliv. Rev.* **2016,** *99*, 28-51.

58. Nguyen, V. P.; Li, Y.; Henry, J.; Zhang, W.; Wang, X.; Paulus, Y. M. High resolution multimodal photoacoustic microscopy and optical coherence tomography visualization of choroidal vascular occlusion. *Int. J. Mol. Sci.* **2020,** *21* (18).

59. McKeown, S. R. Defining normoxia, physoxia and hypoxia in tumours-implications for treatment response. *Br. J. Radiol.* **2014,** *87* (1035), 20130676.

60. Pitts, D. G.; Cullen, A. P.; Hacker, P. D. Ocular effects of ultraviolet radiation from 295 to 365 nm. *Invest. Ophthalmol. Vis. Sci.* **1977,** *16* (10), 932-939.

61. Oxygen permeability coefficients of polymers for hard and soft contact lens applications. *J. Membr. Sci.* **1981**.

62. Oncel, M.; Peyman, G. A.; Khoobehi, B. Tissue plasminogen activator in the treatment of experimental retinal vein occlusion. *Retina (Philadelphia, Pa.)* **1989,** *9* (1), 1-7.

63. Ho, J. K.; Stanford, M. P.; Shariati, M. A.; Dalal, R.; Liao, Y. J. Optical coherence tomography study of experimental anterior ischemic optic neuropathy and histologic confirmation. *Investig. Ophthalmol. Vis. Sci.* **2013,** *54* (9), 5981-8.

64. Ameri, H.; Ratanapakorn, T.; Rao, N. A.; Chader, G. J.; Humayun, M. S. Natural course of experimental retinal vein occlusion in rabbit; arterial occlusion following venous photothrombosis. *Ger J Ophthalmol* **2008,** *246* (10), 1429.

Chapter 3

Organic Room-Temperature Phosphorescent Lipid-Polymer Hybrid Nanoparticles for Highly Sensitive and Quantitative Biodetection

Kang, D.[§]; **Zeng, Y.**[§]; Tewari, M.; Kim, J. "Organic Room-Temperature Phosphorescent Lipid-Polymer Hybrid Nanosensors for Highly Sensitive and Quantitative Biodetection." **2021**, *submitted*. ([§]Both authors contributed equally to this work.)

3.1 Introduction

Optical biosensors are crucial tools in a variety of clinical medicine and biological research areas because they can provide both rapid, qualitative analyses by the naked eye and high-throughput, precise quantifications using more sophisticated optical spectrometers.[1-9] Most of the developed optical biodetection sensors have utilized colorimetric (i.e. absorbance), fluorometric, or chemiluminometric changes of the signal transducing unit, which are triggered by a specific recognition and binding event between the targeted bioanalytes and devised receptors.[10-16] However, these methodologies have their own inherent drawbacks. Colorimetric sensors have a narrow linear correlation detection range due to the deviation in absorptivity of the signal transducing substrates at high concentrations.[17] Fluorometric detection has a low signal-to-noise ratio due to the small Stokes shift and short lifetime (nanoseconds regime) of fluorescent probes.

In this study, we devised a new organic phosphor-based sensor system for bio-detection applications. Phosphorescence is the delayed light emission generated by relaxation of excited electrons from a triplet excited state to the singlet ground state, offering bright emission with a

larger Stokes shift and a longer lifetime (milliseconds to seconds regime for metal-fee purely organic phosphors) than fluorescence.[18] These unique features provide organic phosphorescence-based sensors with a few advantages: (i) ample time to respond to environmental changes and/or external stimuli, such as oxygen tension change, temperature variation, and presence of analytes; (ii) high signal-to-noise ratio owing to minimal interference from the excitation light source or the background autofluorescence. However, phosphorescence-based generic biosensors have not been extensively explored likely due to unclear toxicity and stability of conventional inorganic or organometallic room temperature phosphorescent (RTP) materials for bio-applications.[19]

Metal-free purely organic phosphors are an emerging class of RTP materials showing attractive advantages over their conventional inorganic or organometallic counterparts, such as low cost, high earth-abundance, low toxicity, and flexibility in molecular design. Various metal-free organic phosphors such as BF2-chelates,[20-24] phenylthiobenzene,[25] benzophenone,[26-29] fluorene,[30-32] triazine,[33-35] boronic ester,[36] naphthalimide,[37] sulfone,[38] bromobenzaldehyde,[39-44] and polyaromatic analogues[45,46] have been recently reported. However, employing these organic phosphors in biosensor applications is still at an early stage. Among the successful demonstrations are detection of dissolved oxygen (DO) and bioimaging.[23,44,47-51] In such sensing systems, DO is detected in a signal "turn-off" manner by measuring the decreased phosphorescence intensity, induced by energy transfer from the excited triplet state of phosphors to the ground triplet state of oxygen present[44,52] (Figure 3.1a). We previously reported dissolved oxygen sensing by core-shell polymeric nanoparticles having bromobenzaldehyde-based organic phosphor covalently crosslinked with the polymer matrix by reversible addition-fragmentation chain-transfer (RAFT) polymerization.[44] This dissolved oxygen detection platform showed a very high sensitivity (limit of detection of 60 nM DO) and good compatibility with aqueous environment.

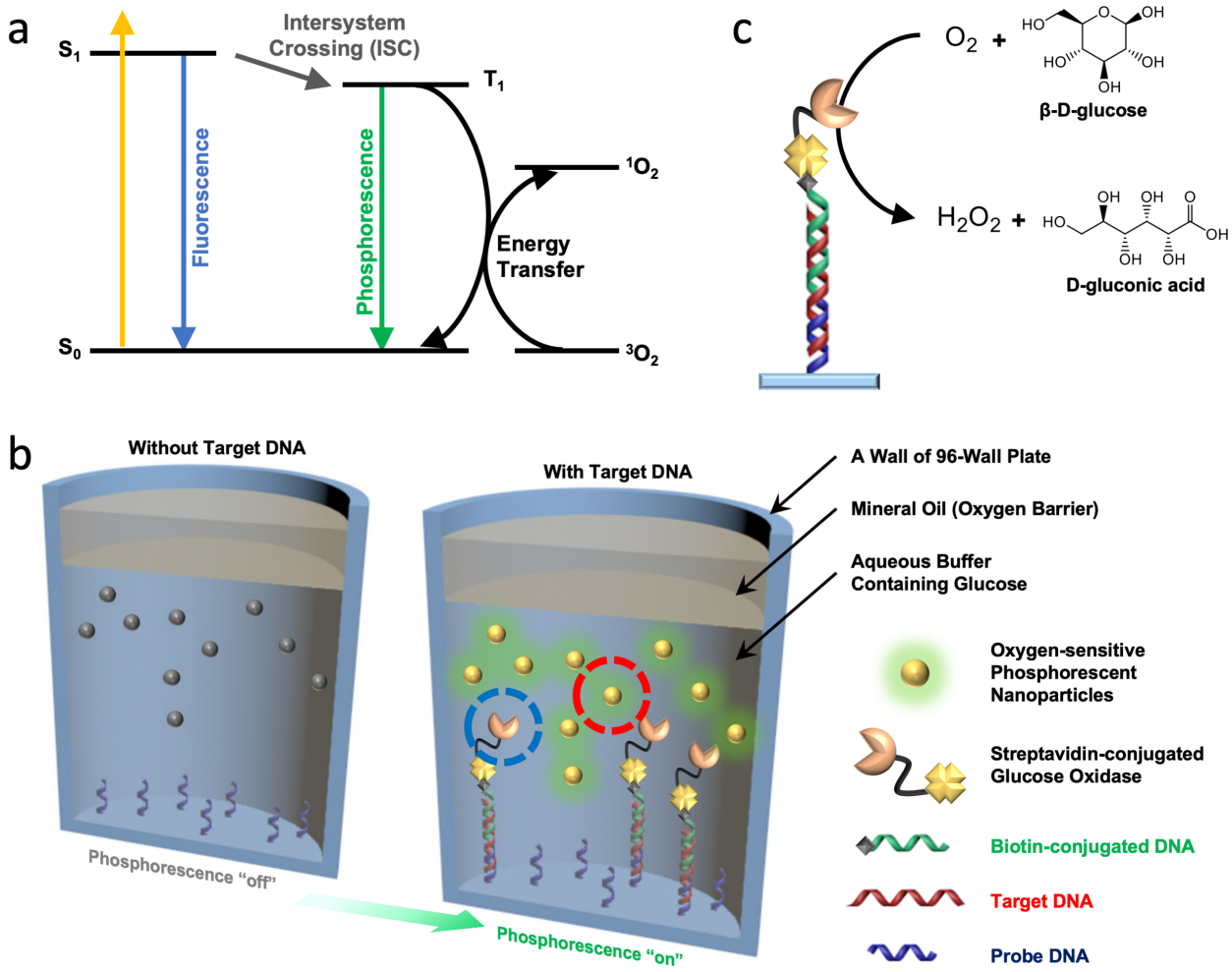

Figure 3.1 | Materials design and detection mechanism of the "turn-on" phosphorescence-based assay platform. a, Energy level diagram illustrating fluorescence and phosphorescence generation process upon photoexcitation, and the phosphorescence quenching process via energy transfer to the triplet state of atmospheric molecular oxygen. **b**, Schematic illustration of the phosphorimetric sandwich hybridization assay detecting DNA using oxygen-sensitive phosphorescent nanoparticles coupled with oxygen-scavenging enzymatic reaction. **c**, Oxygen-scavenging enzymatic reaction of glucose and glucose oxidase.

In this work, we designed an RTP-based "turn-on" biosensor platform by combining the oxygen-sensing capability of the metal-free organic phosphor with an enzymatic oxygen scavenging reaction induced by the presence of targeted analytes. Glucose oxidase enzyme (GOx) is a well-known oxygen scavenger that efficiently consumes DO in the process of oxidizing glucose to gluconic acid (Figure 3.1b,c).[53] Our unique methodology for the phosphorescence-

based biodetection consists of the following three steps; i) the targeted bioanalyte binds to the probe and bioreceptor through specific interaction such as nucleic acid hybridization; ii) the bound bioreceptor will then be labeled with GOx through another specific binding such as avidin-biotin interaction; and iii) finally a solution containing glucose and oxygen-sensitive RTP nanoparticles will be introduced to the target-bioreceptor-GOx complex, as depicted in Figure 3.1c. As the GOx scavenges the DO in the surrounding environment, the signal transducing RTP nanoparticles emit the "turn-on" phosphorescence signal, whose intensity correlates with the concentration of target bioanalytes. It is reasonable to expect that the cyclic enzymatic signal generation will allow for a significant signal amplification hence high sensitivity toward practical applications.[54-57] As a proof of concept, a tumor-associated TP53 gene fragment was tested as the target DNA analyte. Our data support sequence-specific detection with sub-picomolar sensitivity.

3.2 Results and Discussion

3.2.1 Nanoparticle assembly and characterization

To realize our organic RTP-based detection system, we developed a new type of lipid-polymer hybrid core-shell nanoparticles with the metal-free organic phosphor embedded within the polymer matrix core, whose surface was passivated with an amphiphilic lipid shell. Our group has previously reported a synthetic method based on RAFT polymerization to achieve efficient organic RTP in nanoparticles, where metal-free organic phosphors were cross-linked with the polymer matrix.[44] In this study, we adapted a more facile and versatile fabrication method, nanoprecipitation, which can produce homogenous nanoparticles rapidly on a large scale by utilizing a sharp change in the solubility of host materials.[58] In detail, to the aqueous phase, a mixture of the host polymer and guest molecules dissolved in water-miscible organic solvent (e.g.

tetrahydrofuran) was injected. The drastic change of the solubility precipitates the host polymer as insoluble solid nanoparticles encapsulating the guest molecules. The nanoprecipitation is a very instant process occurred when the two solvents are mixed. Therefore, we expected that the nanoprecipitation would result in efficient phosphorescence emission from the uniformly embedded metal-free organic phosphors.

We chose poly(4-bromostyrene) (P4BrS, M_w ~65,000) as the host polymer and Br6A as the metal-free organic phosphor respectively for the nanoparticle assembly (Figure 3.2a). In addition to the optical inertness, the rigidity and oxygen permeability of the host polymer are two critical parameters for the sensor design in order to achieve bright and sensitive RTP for the dissolved oxygen detection. The high rigidity of the host polymer can effectively suppress the vibrational energy dissipation of metal-free phosphors and allow for bright RTP emission.[43] The moderate oxygen permeability of the polymer matrix is necessary for balancing the phosphorescence emission intensity and quenching of the signal by oxygen. Styrene-based polymers have desirable rigidity and proper oxygen permeability for dissolved oxygen detection.[59,60] We further expected that P4BrS, the brominated polystyrene, matrix can enhance the RTP emission of the guest Br6A through additional halogen bonding. The halogen bonding between the oxygen atom of the carbonyl group of Br6A and the neighboring bromine atom of P4BrS can further suppress the vibrational energy dissipation meanwhile enhancing spin−orbit coupling and intersystem crossing of Br6A.[39] About 3% increase in the RTP quantum yield was observed for Br6A-P4BrS nanoparticles (17.1 ± 3.5%) compared to that of Br6A-PS nanoparticles (13.2 ± 3.1%).

We further synthesized the lipid-polymer hybrid core-shell organic RTP nanoparticle, termed Br6A-LP4BrS, by adding an anionic phospholipid, 1,2-dimyristoyl-sn-glycero-3-

phosphate (DMPA) in the aqueous phase during the nanoprecipitation process. The purpose of phospholipid coating on the nanoparticle surface is to increase the dispersion stability in water at concentrated states, particularly for long-term storage, by preventing aggregation through the electrostatic repulsion or hydration.[61-65] When the DMPA lipid was used at 15 wt% with respect to P4BrS, dynamic light scattering (DLS) data indicate narrow-dispersed (polydispersity index (PDI): 0.063) nanoparticles with a Z-average diameter of 161.7 nm (Figure 3.2b black line). The particle size and its spherical shape were further confirmed by scanning electron microscope (SEM, Figure 3.2c). In contrast, nanoparticles prepared without DMPA lipid have a higher polydispersity (PDI; 0.158) and a larger hydrodynamic diameter of 250 nm (Figure 3.2b orange line) when the initial P4BrS concentration is 1 mg/ml in THF. It is also important to note that the highly concentrated polymer solution (10 mg/ml) injected into the aqueous phase without the DMPA lipid resulted in massive aggregation instead of discrete nanoparticle formation. Thus, the addition of DMPA lipids is necessary to ensure homogeneous dispersion of the polymer in the aqueous phase by serving as a surfactant, which reduces the surface and interfacial tension and stabilizes the polymer-water interface during the nanoprecipitation process.[66,67] The decrease in the zeta potential (ζ) of the resulting Br6A-LP4BrS nanoparticles (-43.6 ± 2.0 mV) in comparison with bare Br6A-P4BrS (-23.4 ± 0.8 mV) suggests the successful coating of the negatively-charged DMPA lipid on the nanoparticle surface (Figure 3.2d). This simple one-step nanoprecipitation method is easy to scale up for mass and reproducible production of such organic RTP nanoparticles.

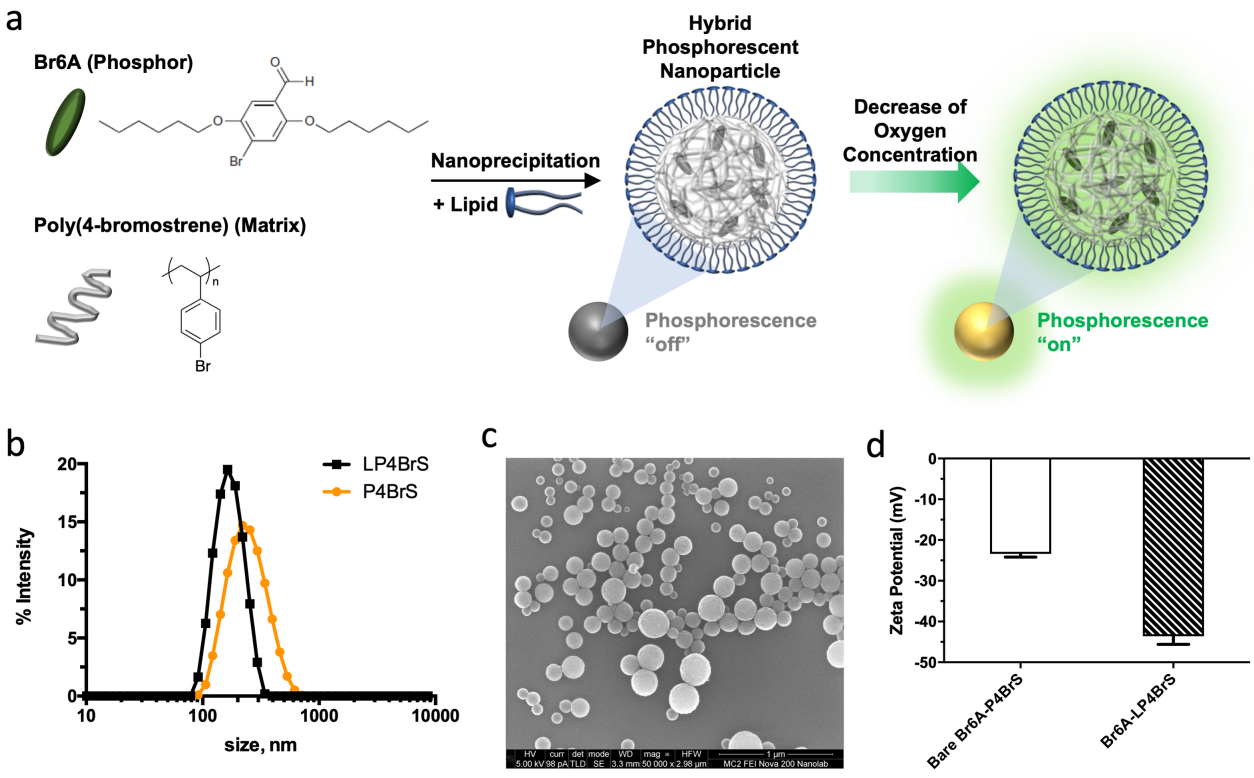

Figure 3.2 | Synthesis and chemophysical characterizations of lipid-polymer hybrid organic room-temperature phosphorescent nanoparticles Br6A-LP4BrS. a, Schematic illustration on nanoprecipitation process for the rapid generation of lipid-polymer hybrid nanoparticles having a metal-free organic phosphor, Br6A. **b,** Size distribution of phosphorescent lipid-polymer hybrid nanoparticles (LP4BrS, black line) compared to bare polymer nanoparticles without lipid coating (P4BrS, orange line). **c,** Scanning electron microscope image of phosphorescent lipid-polymer hybrid nanoparticles. **d,** Zeta potential of lipid polymer-hybrid nanoparticles (LP4BrS) and the control polymer nanoparticles prepared without lipid coating (P4BrS).

We then confirmed the RTP nature of the emission from the fabricated Br6A-LP4BrS nanoparticles, shown in Figure 3.3a. As expected, the nanoparticle solution exhibited bright green emission under 365 nm excitation after removal of the dissolved oxygen by the enzymatic reaction of GOx and glucose (the inset photograph in Figure 3.3a). Steady state photoluminescence spectroscopy data confirmed the emission and excitation spectra maxima at 525 nm and 365 nm, respectively. The gated emission spectrum acquired after 500 μs delay well overlapped with the steady state emission, confirming that the green emission is indeed of phosphorescent nature rather than fluorescent. Lifetime (τ) measurement of the green emission monitored at 525 nm resulted

4.0 ms (Figure 3.3b), further corroborating the phosphorescent emission. In summary, photophysical characteristics of these Br6A-LP4BrS nanoparticles are in good agreement with those of Br6A in the crystalline state[24] or embedded in isotactic poly(methyl methacrylate) film[25] reported previously, indicating the successful inclusion of Br6A into the nanoparticle matrix by the nanoprecipitation method.

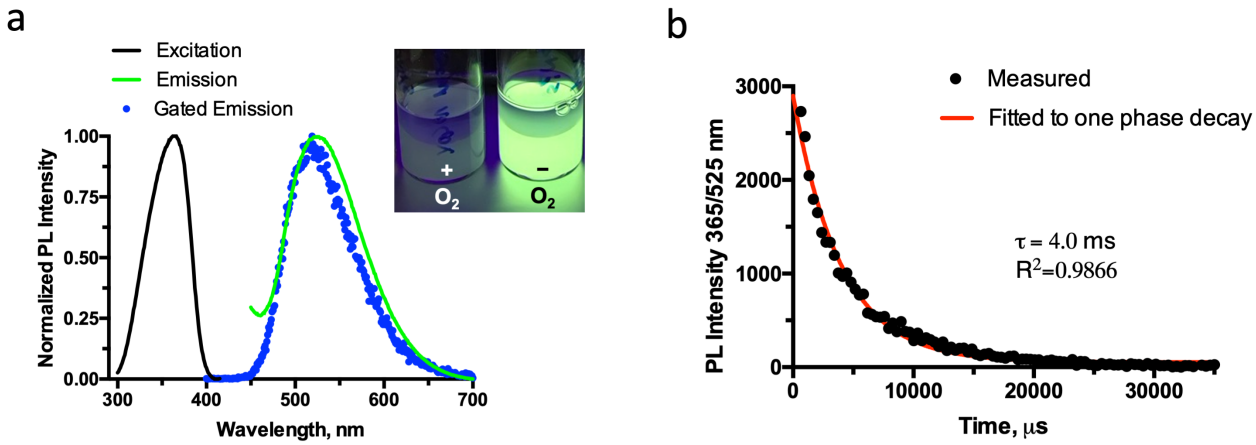

Figure 3.3 | Photophysical characterizations of lipid-polymer hybrid organic room-temperature phosphorescent nanoparticles Br6A-LP4BrS. a, Photoluminescent excitation (black line), steady-state emission (green line), and gated emission spectra (blue dots) of phosphorescent lipid-polymer hybrid nanoparticles. The inset photograph shows phosphorescent lipid-polymer hybrid nanoparticles dispersed in air-saturated (left) and oxygen-scavenged (right) aqueous solutions at room temperature under 365 nm UV irradiation. **b,** Phosphorescence emission decay profile of Br6A-LP4BrS nanoparticles suspended in an anoxic aqueous solution monitored at 525 nm (λ_{ex} = 365 nm), confirming the long-lived character of the green phosphorescence with a lifetime (τ) of 4.0 ms.

3.2.2 Phosphorescence-based detection of avidin-biotin interaction

We next constructed the novel organic RTP-based biodetection system using the phosphorescent lipid-polymer hybrid nanoparticles. The commercially available 96-well plate was selected as our biodetection platform since these plates have been widely used for various high-throughput biosensor systems such as enzyme-linked immunosorbent assay (ELISA) or DNA detection. Therefore, successful demonstration of organic RTP-based biosensors using the 96-well

plate will be beneficial for various biomedical applications. We first examined the feasibility of our design on a commercial biotin-coated plate by detecting the avidin-biotin interaction between glucose oxidase-conjugated streptavidin molecules (STA-GOx) and the surface-tethered biotin (Figure 3.4a). Various concentrations of STA-GOx were added to the biotin-coated plate, followed by one-hour incubation. Non-specifically bound STA-GOx molecules were removed by thorough washing, and finally the plate was filled with a solution containing Br6A-LP4BrS nanoparticles and glucose. In addition, we covered the top of the solution in the well with heavy mineral oil (density: 0.862 g/ml) to form an oxygen diffusion barrier that prevents rapid diffusion of atmospheric oxygen into the sample solutions during the course of the experiment (Figure 3.4c).[68] As expected, the oil-based oxygen barrier enhances the phosphorescence signal about 1.5 times, as compared with that of the uncovered pristine wells. This measure ensures that the resulting RTP signal truly correlates with the bound STA-GOx.

We confirmed the phosphorescence emission in the well by using a 365 nm handheld UV lamp (4W) as the excitation light source. Strong green phosphorescence signal was observed by the naked eye, within 30-min of incubation, suggesting that the organic RTP nanoparticles are capable of providing rapid biodetection. Both the camera image and the quantitative signal measurement by a plate reader showed that the phosphorescent emission was enhanced as the loaded concentration of STA-GOx increased, as a "turn-on" biodetection sensor (Figure 3.4b). These results assure the feasibility of our detection methodology, indicating that STA-GOx was immobilized onto the plate well through the specific avidin-biotin interaction, and subsequently the dissolved oxygen concentration in the well was reduced through the enzymatic oxygen scavenging reaction between the immobilized STA-GOx and glucose in the solution. It should be noted that the fluorescence emission peak of GOx[69] coincides with the RTP emission peak of

Br6A-LP4BrS nanoparticles. However, under our experimental conditions, the fluorescence emission from the immobilized STA-GOx, even at the highest working concentration (50 μg/ml), was negligible in comparison with the strong phosphorescence signal generated by RTP nanoparticles in the solution. The heavy mineral oil layer on top of sample solutions remarkably reduced the phosphorescent signal quenching by ambient oxygen (Figure 3.4c). In other words, stable monitoring of the oxygen consumption in response to the targeted analyte concentration using a 96-well plate platform was successfully achieved.

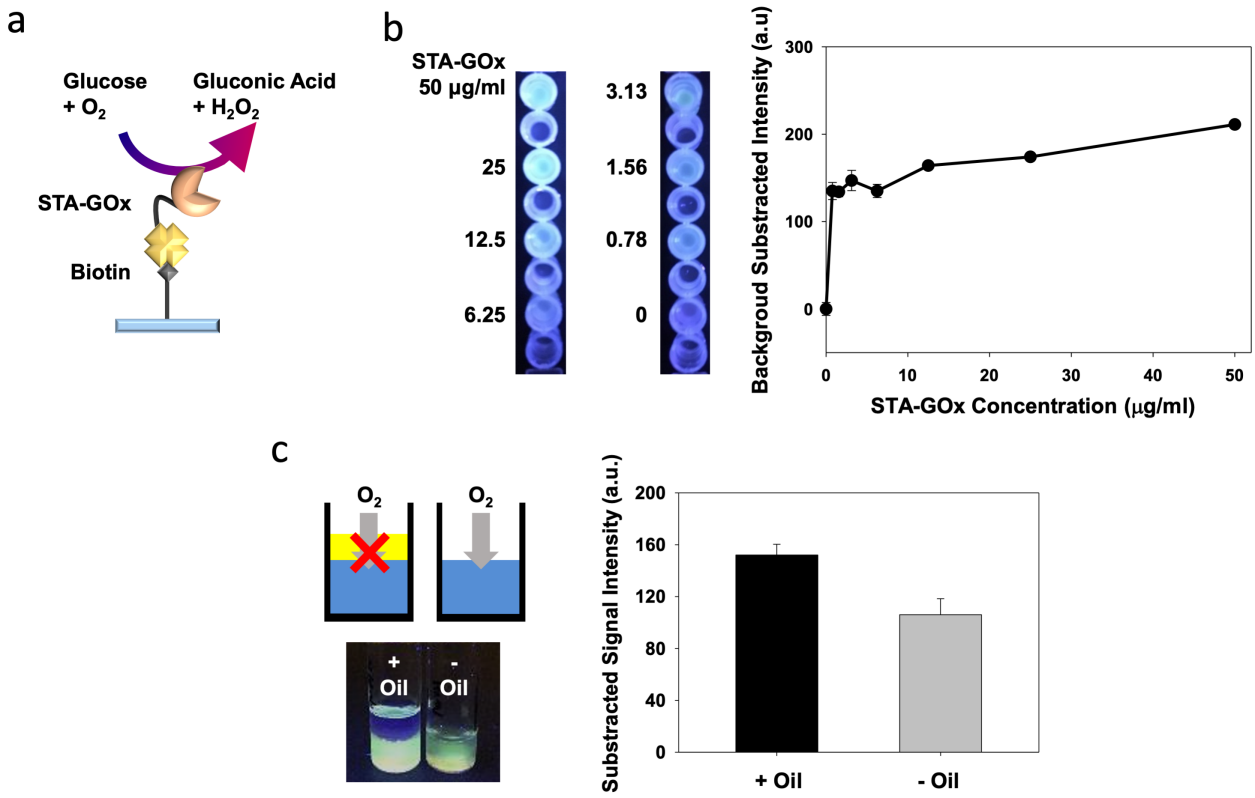

Figure 3.4 | Phosphorescence-based detection of avidin-biotin interaction. a, Schematic illustration on the phosphorescent detection of avidin-biotin interaction. For the development of phosphorescence signal by the phosphorescent nanoparticles, the dissolved oxygens are scavenged by glucose oxidase-conjugated streptavidin molecules (STA-GOx) combined with the surface-tethered biotin on the well plate. **b**, Smartphone camera image presenting the phosphorescent detection of avidin-biotin interaction, and the corresponding relative phosphorescent intensity graph. Each well having surface-tethered biotins were exposed to the various concentrations of STA-GOx respectively by 1hr incubation, and then the phosphorescent signals were developed. The middle well between the wells treated with two different concentrations of STA-GOx were intended to be empty to avoid the crosstalk of light emission by the adjacent wells. **c**, Phosphorescence signal enhancement by using a heavy mineral oil (density: 0.862 g/ml) as an oxygen diffusion barrier. The bar graph indicates that the phosphorescence emission from wells covered with oil barrier was 1.5 times greater than that from the uncovered wells. The wells were pre-incubated with 10 µg/ml of STA-GOx.

3.2.3 Phosphorescence-based cell-free DNA detection by sandwich hybridization

Based on the successful detection of avidin-biotin interaction using our turn-on sensor design, we further investigated a feasible detection scheme for a fragment of human TP53 gene to demonstrate the versatility of our detection system. The TP53 gene is a very important clinical

marker because its mutation has been found in many types of human cancers.[70,71] The p53 protein encoded by the TP53 gene functions as a tumor suppressor which can repair DNA damage or can initiate apoptosis to remove damaged DNA.[72,73] Therefore, the mutation of TP53 means that such tumor suppression pathways regulated by the p53 protein are not operating, and only one-base pair mismatch can deactivate the P53 protein function. Importantly, TP53 gene DNA can be extracted from blood plasma or other biofluids as cell-free DNAs, enabling convenient "liquid biopsy" instead of conventional invasive tumor tissue biopsies.[74-78]

We designed a sandwich type of DNA hybridization assay using two half-length DNA probes complimentary to the target DNA strand for selective detection. As shown in Figure 3.1c and Figure 3.5a, the first half-length DNA probe having an amine group at its 3'-end (5'-GAG AGA CCG GCG CAC-NH_2-3') was immobilized onto the epoxy-coated well plate through the amine-epoxy chemistry. The second half-length DNA probe strand has a biotin group conjugated at its 5'-end (5'-biotin-TTG TGC CTG TCC TGG-3') for further binding with STA-GOx. Through the sandwich hybridization, biotin groups can be immobilized on the plate surface only when the target DNA strand (5'-GTG CGC CGG TCT CTC CCA GGA CAG GCA CAA-3') is present in the sample. STA-GOx is then attached to the biotin groups, and subsequently induces the phosphorescence signal when Br6A-LP4BrS nanoparticles solution containing glucose is added (Figure 3.1b). As we anticipated, the green phosphorescence intensity was promoted gradually as the concentration of the target DNA strand increased (Figure 3.5b) within the tested concentration range (0.05 pM to 5 μM). Notably, the detection limit of our sensor design is around 0.5 pM, comparable to or better than that of the reported optical biosensors for TP53 gene detection, demonstrating its high sensitivity.[79-81] Furthermore, when an one-mismatch sequence (5'-GTG CG**T** CGG TCT CTC CCA GGA CAG GCA CAA-3') was introduced, there was no remarkable

phosphorescence emission generated. With a three-mismatch sequence (5'-GTG CG**T** CGG T**T**T CTC **T**CA GGA CAG GCA CAA-3'), the RTP signal showed more significant drop, verifying the detection selectivity (Figure 3.5c). We also tried to detect TP53 fragments spiked in human urine samples by using our phosphorescent assay (Figure 3.5d). Though the deviations become wider, our system still shows phosphorescent signals correlated with target DNA concentrations in the urine sample, presenting a similar level of detection limit (0.5 PM). The demonstrated sensitivity, selectivity, and suitability for detecting target biomolecules in body fluid samples indicates that our system could be suitable for various practical biodetection applications.

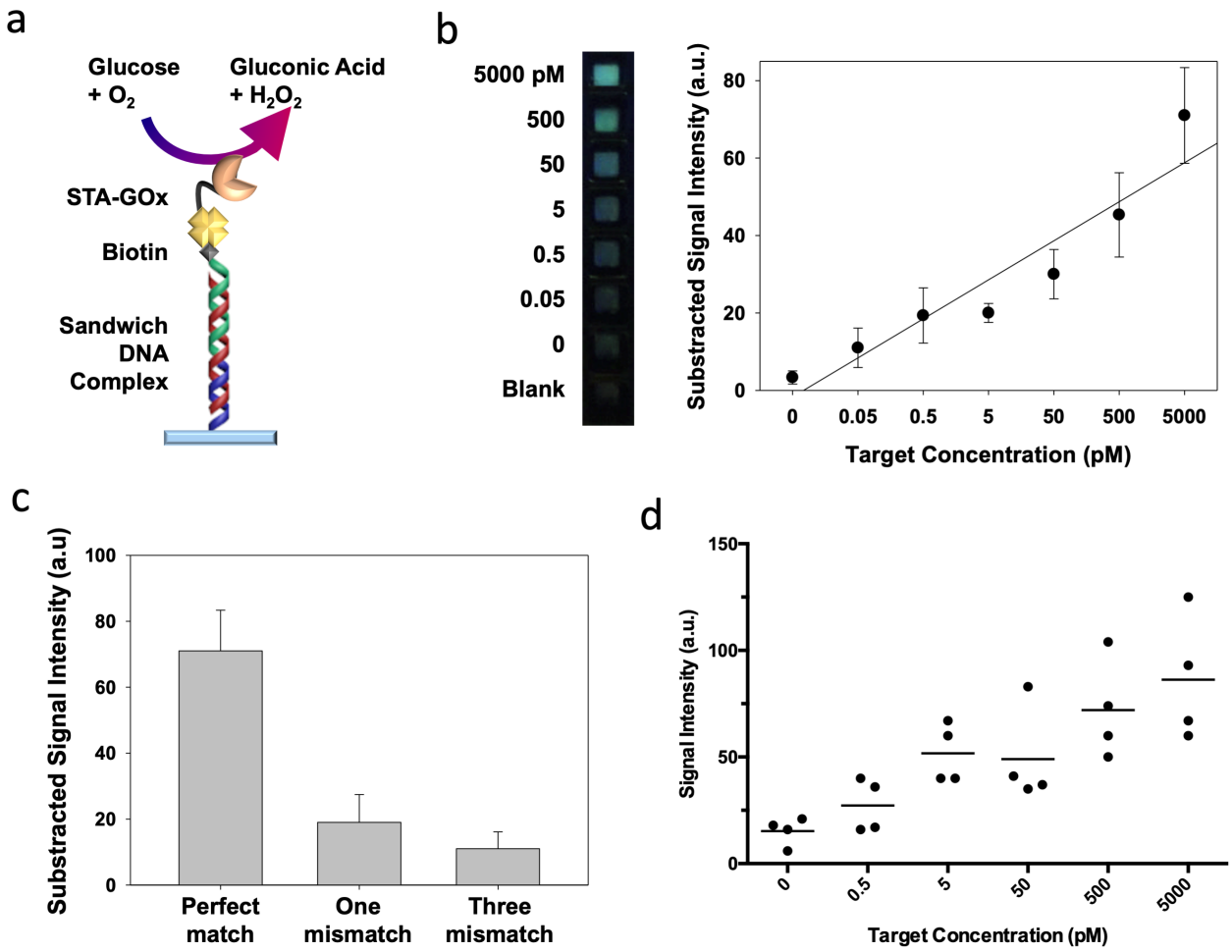

Figure 3.5 | Phosphorescence-based cell-free DNA detection by sandwich hybridization. a, Schematic illustration on phosphorescent detection of DNA fragment molecules. For the phosphorescence signal development by the nanoparticles, the dissolved oxygens are scavenged by STA-GOx combined with sandwich DNA complex having a biotin end group. **b**, Smartphone camera image presenting the phosphorescent detection of various concentrations of DNA fragments, and the corresponding relative phosphorescent intensity graph. **c**, Selectivity of this phosphorescence-based DNA assay to the one-mismatch and three-mismatch DNA fragments. **d**, Phosphorescence-based detection of various concentrations of target DNA fragments spiked in human urine samples.

3.3 Conclusion and Outlook

In summary, we have successfully demonstrated a new organic RTP-based biosensor platform based on the sensitive phosphorescence quenching of metal-free organic phosphors in the presence of oxygen. Phosphorescent lipid-polymer hybrid nanoparticles were fabricated by

nanoprecipitation of metal-free organic phosphorescent molecules, Br6A, and rigid and oxygen permeable poly(4-bromostyrene) in an aqueous solution having an anionic phospholipid, DMPA. The hybrid nanoparticle is used as a turn-on signal generation unit in connection with glucose oxidase enzyme (GOx) and glucose solution on the widely used 96-well plates. The sensory platform is rationally designed such a way that only target-specific recognition events can retain the hybrid nanoparticles and GOx in the glucose solution to produce sensitive phosphorescence turn-on signal. A cancer biomarker, a fragment of human TP53 gene, was successfully detected with a sub-picomolar detection limit owing to the oxygen sensitivity of metal-free organic phosphors and enzymatic signal amplification. Our unique methodology can be adapted to a broad range of biosensor applications requiring highly sensitive and quantitative optical biodetection with a high signal-to-noise ratio. Simply by re-programming the detection probe, our organic RTP-based sensor design has a strong potential to serve as a universal sensor platform for biomarkers of great clinical importance but difficult to detect due to their low abundance *in vivo*. The detection limit of this phosphorimetric assay is partly controlled by oxygen sensitivity of organic RTP NPs, and can be further improved (i.e., lowered) by choosing a polymer matrix or polymer blends with relatively lower oxygen permeability to encapsulate organic phosphor.

To realize point-of-care (POC) diagnostics,[82] future work could be to adapt the 96-well plate-based platform to more portable substrates, such as papers and capillary tubes. We envision that one day patients may apply their own urine or blood samples to a prefabricated test (an "off-the-shelf" product similar to a home pregnancy test), record the result with a smartphone and electronically submit the outcome to their healthcare team for interpretation and long-term monitoring (Figure 3.6). This technology could have a profound impact on patient compliances, as well as early diagnosis and prognosis of cancer in resource-limited settings.

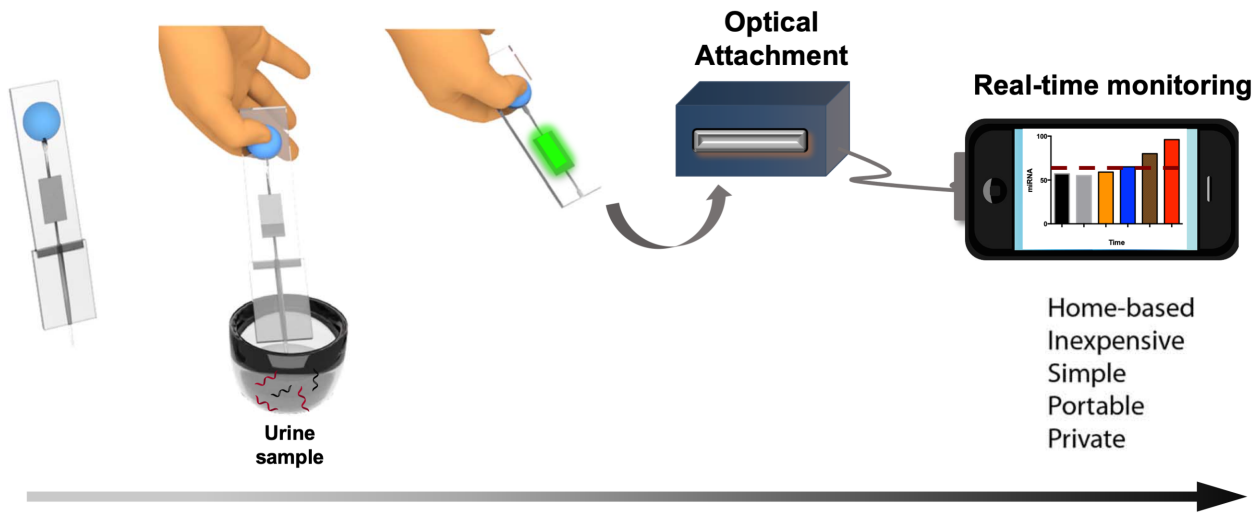

Figure 3.6 | Schematic illustration of point-of-care process flow for cell-free DNA analysis. a microfluidic device that has a capillary-based disposable tip at the inlet and a rubber bulb at the outlet to create negative pressure for sample loading and washing steps. A smartphone optical attachment is used for organic RTP signal readout and transmission. Adapted from reference 82.

3.4 Experimental Section

3.4.1 Materials

Poly(4-bromostyrene) (PS4Br, M_w ~65,000), glucose, bovine serum albumin, ethanolamine, solvents, buffers, heavy mineral oil, and reagents used to synthesize the organic phosphor Br6A were all purchased from Millipore Sigma and used without further purification. Phospholipid 1,2-dimyristoyl-sn-glycero-3-phosphate (DMPA) was purchased from Avanti Polar Lipids. FisherBrand™ disposable cuvettes (10 mm pathlength, PMMA) and Malvern Panalytical folded capillary zeta cells for dynamic light scattering measurements were purchased from Fisher Scientific. Amicon® Ultra-4 centrifugal filters (MWCO 30 kD) for nanoparticle purification were purchased from Millipore Sigma. The streptavidin-conjugated glucose oxidase (STA-GOx) was purchased from Fitzgerald. Biotin-coated 96 well plates were purchased from Thermo Fisher Scientific, and epoxy-modified 96 well plates were obtained from Arrayit technology.

All DNAs were obtained from Integrated DNA Technologies, Inc. and the sequences are as follows:

1) Complementary target strand: 5'-GTG CGC CGG TCT CTC CCA GGA CAG GCA CAA-3'
2) Three-base-mismatched strand: 5'-GTG CG**T** CGG T**T**T CTC **T**CA GGA CAG GCA CAA-3'
3) One-base-mismatched strand: 5'-GTG CG**T** CGG TCT CTC CCA GGA CAG GCA CAA-3'
4) Biotin-conjugated probe: 5'-biotin-TTG TGC CTG TCC TGG-3'
5) Amine-terminated probe: 5'-GAG AGA CCG GCG CAC-NH_2-3'

3.4.2 Preparation of lipid-polymer hybrid organic RTP NPs Br6A-LP4BrS

The metal-free organic phosphor Br6A was synthesized according to a published procedure from the Kim lab[39], and its purity was confirmed by ^{1}H NMR. The lipid-polymer hybrid nanoparticle containing metal-free organic phosphor, Br6A-LP4BrS, was fabricated by a single-step nanoprecipitation method. 1.5 mg of DMPA (15 wt% to P4BrS) was dispersed into 10 ml of 4 wt% ethanol-water solution to prepare the aqueous outer phase. The dispersion was then heated up to 65 °C until the solution became completely transparent to ensure that all the lipids were in the liquid phase. A stock solution of 10 mg/ml PS4Br mixed with 1 wt% Br6A was prepared in THF. Then 1 ml of this mixture solution was injected into the aqueous outer phase with vigorous stirring. The resulting suspension was subsequently sonicated for 10 minutes using a bath sonicator (Bransonic 2510-DTH) at a frequency of 42kHz and power of 100 W. It was then further stirred at room temperature overnight to allow for the complete evaporation of organic solvents. Purification was be done by washing nanoparticles in milli-Q water 3 times using Amicon® Ultra-4 centrifugal filters with a molecular weight cutoff of 30 kD. The purified Br6A-LP4BrS

nanoparticles were re-suspended in milli-Q water to make 1 mg/mL stock concentration. The suspension was stable for months stored under ambient condition.

3.4.3 Characterization of lipid-polymer hybrid organic RTP NPs Br6A-LP4BrS

Hydrodynamic Size (diameter, nm), surface charge (zeta potential ζ, mV), and PDI of the lipid-polymer hybrid NPs were measured in Milli-Q water on Malvern Zetasizer Nano ZSP (Model number: ZEN5600) using disposal cuvettes and folded capillary zeta cells, respectively. All measurements were conducted at a backscattering angle of 173° (NIBS default) at 25 °C. Size and polydispersity analyses were performed using Malvern Zetasizer software (Ver. 7.11). The average hydrodynamic diameters of NPs are reported using the Z-average of size distribution plots by intensity. Particle size and morphology were further examined by scanning electron microscope (SEM, FEI Nova 200 Nanolab) after carbon coating. Photophysical properties including steady state emission and excitation spectra, gated emission, lifetime, and absolute quantum yield were measured using a Photo Technologies International (PTI) QuantaMaster spectrofluorometer equipped with an integrating sphere. Anoxic aqueous suspensions of RTP NPs were prepared by bubbling argon gas through sample solutions placed in rubber septum-capped quartz cuvettes for 30 min. All experiments were performed in triplicate from freshly prepared samples (n = 3). Data are expressed as the mean ± standard deviation.

3.4.4 Phosphorescence-based detection of avidin-biotin interaction

To the wells of a biotin-coated 96-well plate, 100 µl of 1x PBS buffer containing various amount of streptavidin-conjugated glucose oxidase (STA-GOx) were added. After one-hour incubation, the wells were washed three times with 1x PBST Buffer (1x PBS containing 0.05%

Tween 20) and three times with 1x PBS, and then were dried carefully with air blowing. The nanoparticle solution for phosphorescent signal generation was prepared freshly in every experiment by mixing 1 mg/ml Br6A-LP4BrS nanoparticle suspension, 100 mg/ml glucose solution, and 10x PBS Buffer (8:1:1 volume ratio). The wells were filled with 200 µl of the phosphorescent nanoparticle solution, and then overlaid with 150 µl of heavy mineral oil to inhibit the oxygen diffusion from the outside. The phosphorescent signal generation in the wells was qualitatively monitored by the naked eye or iPhone camera, while being illuminated by the 365 nm UV light (4W handheld lamp) at a distance of 10 cm. Quantification of the phosphorescent signal was acquired on Biotek Synergy Neo plate reader.

3.4.5 Phosphorescence-based TP53 DNA detection in buffer by sandwich hybridization

(1) Immobilization of amine-probe onto 96-well plate: The wells of an epoxy-coated plate were incubated overnight with 100 µl of 150 mM sodium phosphate buffer (pH ~ 8.5) containing the amine-probe (1.0 µM). After washing four times with 1x PBST Buffer (1x PBS containing 0.05% Tween 20) and four times with 1x PBS, the wells were incubated for an hour with 200 µl of 10% (v/v) ethanolamine solution (the solution pH was adjusted to 9 using HCl). The wells were washed twice and were then dried carefully with air blowing.

(2) Sandwich DNA hybridization on 96-well plate: The biotin-conjugated DNA probe (20 nM) and various amount of target DNA (or mismatched DNAs) were dissolved in 5x saline sodium citrate (SSC) buffer separately. After mixing the biotin-probe solution and the target DNA solution (1:1 volume ratio), the mixture was incubated for 5 mins at 85 °C. Typically, to 100 µl of the biotin-probe solution, various concentrations of target DNA solutions (100 µl) were added and mixed. Afterward, 99 µl of the mixed solution were loaded into the wells of the amine-probe coated

plate, and then 1 μl of 10% SDS solution added to the solution in the wells directly. After 3-hour incubation at 60 °C, the plates were washed three times with 0.2x SSC buffer. The plates were further blocked by one-hour incubation with 20 mg/ml of bovine serum albumin solution (1x PBS, loading volume: 100 μl). The wells were washed two times with 1x PBST and two times with 1x PBS, and then were dried carefully with air blowing.

(3) Phosphorescent Signal Generation: Phosphorescent signals in the well were developed according to a similar way to the phosphorescent detection of avidin-biotin interaction. After the sandwich DNA hybridization, the wells were incubated with 10 μg/ml STA-GOx solution (1x PBS containing 1 mg/ml BSA, 100 μl) for one hour. Subsequently, the wells were washed four times with 1x PBST and four times with 1x PBS, and then were dried carefully with air blowing. The phosphorescent signal generation solution was prepared freshly by mixing 1 mg/ml Br6A-LP4BrS nanoparticle suspension, 100 mg/ml glucose solution, and 10x PBS Buffer (8:1:1 volume ratio). The STA-GOx-treated wells were added with 200 μl of the phosphorescent signal generation solution, and then covered directly with 200 μl of heavy mineral oil. The phosphorescent signal in the well were monitored by the protected naked eye, iPhone camera, or Biotek Synergy Neo plate reader.

3.4.6 Phosphorescence-based TP53 DNA detection in urine sample

Urine samples were collected from 2 healthy control subjects. Subjects provided signed informed consent to participate in research under University of Michigan Institutional Review Board protocol HUM00092161. Briefly, a single urine void was collected and immediately mixed with 100 mL of 0.5M EDTA as a preservative. Urine samples were centrifuged at 1,600 xg for 10 minutes at room temperature. Urine supernatant was transferred to a fresh tube and centrifuged

again at 3,000 xg for 10 minutes at room temperature. Urine supernatant was transferred to a fresh tube and frozen at -80 ℃. The collected urine samples were spiked with various concentrations of target DNAs. The target DNAs in the urine sample were detected in the same way as for the DNA detection in buffer.

3.5 References

1. Cooper, M. A. Optical biosensors in drug discovery. *Nature Reviews Drug Discovery* **2002,** *1* (7), 515-528.

2. Borisov, S. M.; Wolfbeis, O. S. Optical biosensors. *Chem. Rev.* **2008,** *108* (2), 423-461.

3. Yoo, S. M.; Lee, S. Y. Optical biosensors for the detection of pathogenic microorganisms. *Trends Biotechnol.* **2016,** *34* (1), 7-25.

4. Sha, R.; Badhulika, S. Recent advancements in fabrication of nanomaterial based biosensors for diagnosis of ovarian cancer: A comprehensive review. *Microchimica Acta* **2020,** *187* (3).

5. Hofferber, E. M.; Stapleton, J. A.; Iverson, N. M. Review-single walled carbon nanotubes as optical sensors for biological applications. *J. Electrochem. Soc.* **2020,** *167* (3).

6. Soler, M.; Lechuga, L. M. Boosting cancer immunotherapies with optical biosensor nanotechnologies. *Eur. Med. J.* **2019,** *4*, 124-132.

7. Garzon, V.; Pinacho, D. G.; Bustos, R. H.; Garzon, G.; Bustamante, S. Optical biosensors for therapeutic drug monitoring. *Biosensors-Basel* **2019,** *9* (4).

8. Lai, M. M.; Slaughter, G. Label-free microrna optical biosensors. *Nanomaterials-Basel* **2019,** *9* (11).

9. Ligler, F. S.; Gooding, J. J. Lighting up biosensors: Now and the decade to come. *Anal. Chem.* **2019,** *91* (14), 8732-8738.

10. Piriya, V. S. A.; Joseph, P.; Daniel, S. C. G. K.; Lakshmanan, S.; Kinoshita, T.; Muthusamy, S. Colorimetric sensors for rapid detection of various analytes. *Mater. Sci. Eng. C Mater. Biol. Appl.* **2017,** *78*, 1231-1245.

11. Jia, M.-Y.; Feng, L. Recent progresses in optical colorimetric/fluorometric sensor array. *Chinese Journal of Analytical Chemistry* **2013,** *41* (5), 795-802.

12. Nawrot, W.; Drzozga, K.; Baluta, S.; Cabaj, J.; Malecha, K. A fluorescent biosensors for detection vital body fluids' agents. *Sensors (Basel, Switzerland)* **2018,** *18* (8).

13. Aboul-Enein, H. Y.; Stefan, R. I.; van Staden, J. F.; Zhang, X. R.; Garcia-Campana, A. M.; Baeyens, W. R. G. Recent developments and applications of chemiluminescence sensors. *Crit. Rev. Anal. Chem.* **2000,** *30* (4), 271-289.

14. Yeh, H. W.; Ai, H. W. Development and applications of bioluminescent and chemiluminescent reporters and biosensors. *Annu Rev Anal Chem* **2019,** *12*, 129-150.

15. Hananya, N.; Green, O.; Blau, R.; Satchi-Fainaro, R.; Shabat, D. A highly efficient chemiluminescence probe for the detection of singlet oxygen in living cells. *Angew Chem Int Edit* **2017,** *56* (39), 11793-11796.

16. Yan, J. T.; Lee, S.; Zhang, A. F.; Yoon, J. Self-immolative colorimetric, fluorescent and chemiluminescent chemosensors. *Chem. Soc. Rev.* **2018,** *47* (18).

17. Kangas, M. J.; Burks, R. M.; Atwater, J.; Lukowicz, R. M.; Williams, P.; Holmes, A. E. Colorimetric sensor arrays for the detection and identification of chemical weapons and explosives. *Crit. Rev. Anal. Chem.* **2017,** *47* (2), 138-153.

18. Wu, S.; Pan, Z.; Chen, R.; Liu, X.; SpringerLink (Online service), Long afterglow phosphorescent materials. Springer International Publishing : Imprint: Springer: Cham, 2017. https://link.springer.com/10.1007/978-3-319-60421-3.

19. Rai, M.; Ingle, A. P.; Medici, S. *Biomedical applications of metals*. Springer: Cham, 2018; p xviii, 325 pages.

20. Zhang, G.; Chen, J.; Payne, S. J.; Kooi, S. E.; Demas, J. N.; Fraser, C. L. Multi-emissive difluoroboron dibenzoylmethane polylactide exhibiting intense fluorescence and oxygen-sensitive room-temperature phosphorescence. *J. Am. Chem. Soc.* **2007,** *129* (29), 8942-+.

21. Zhang, G.; Palmer, G. M.; Dewhirst, M. W.; Fraser, C. L. A dual-emissive-materials design concept enables tumour hypoxia imaging. *Nat. Mater.* **2009,** *8* (9), 747-51.

22. Nagl, S.; Baleizao, C.; Borisov, S. M.; Schaferling, M.; Berberan-Santos, M. N.; Wolfbeis, O. S. Optical sensing and imaging of trace oxygen with record response. *Angew Chem Int Edit* **2007,** *46* (13), 2317-2319.

23. Lehner, P.; Staudinger, C.; Borisov, S. M.; Klimant, I. Ultra-sensitive optical oxygen sensors for characterization of nearly anoxic systems. *Nat Commun* **2014,** *5*, 4460.

24. Koch, M.; Perumal, K.; Blacque, O.; Garg, J. A.; Saiganesh, R.; Kabilan, S.; Balasubramanian, K. K.; Venkatesan, K. Metal-free triplet phosphors with high emission efficiency and high tunability. *Angew Chem Int Edit* **2014,** *53* (25), 6378-6382.

25. Fermi, A.; Bergamini, G.; Roy, M.; Gingras, M.; Ceroni, P. Turn-on phosphorescence by metal coordination to a multivalent terpyridine ligand: A new paradigm for luminescent sensors. *J. Am. Chem. Soc.* **2014,** *136* (17), 6395-6400.

26. Yuan, W. Z.; Shen, X. Y.; Zhao, H.; Lam, J. W. Y.; Tang, L.; Lu, P.; Wang, C. L.; Liu, Y.; Wang, Z. M.; Zheng, Q.; Sun, J. Z.; Ma, Y. G.; Tang, B. Z. Crystallization-induced phosphorescence of pure organic luminogens at room temperature. *J Phys Chem C* **2010,** *114* (13), 6090-6099.

27. Gong, Y. Y.; Chen, G.; Peng, Q.; Yuan, W. Z.; Xie, Y. J.; Li, S. H.; Zhang, Y. M.; Tang, B. Z. Achieving persistent room temperature phosphorescence and remarkable mechanochromism from pure organic luminogens. *Adv. Mater.* **2015,** *27* (40), 6195-6201.

28. Xie, Y. J.; Ge, Y. W.; Peng, Q.; Li, C. G.; Li, Q. Q.; Li, Z. How the molecular packing affects the room temperature phosphorescence in pure organic compounds: Ingenious molecular design, detailed crystal analysis, and rational theoretical calculations. *Adv. Mater.* **2017,** *29* (17).

29. Yang, Z.; Mao, Z.; Zhang, X.; Ou, D.; Mu, Y.; Zhang, Y.; Zhao, C.; Liu, S.; Chi, Z.; Xu, J.; Wu, Y. C.; Lu, P. Y.; Lien, A.; Bryce, M. R. Intermolecular electronic coupling of organic units for efficient persistent room-temperature phosphorescence. *Angew Chem Int Ed Engl* **2016,** *55* (6), 2181-5.

30. Xu, J. J.; Takai, A.; Kobayashi, Y.; Takeuchi, M. Phosphorescence from a pure organic fluorene derivative in solution at room temperature. *Chem. Commun.* **2013,** *49* (76), 8447-8449.

31. Hirata, S.; Totani, K.; Zhang, J.; Yamashita, T.; Kaji, H.; Marder, S. R.; Watanabe, T.; Adachi, C. Efficient persistent room temperature phosphorescence in organic amorphous materials under ambient conditions. *Adv. Funct. Mater.* **2013,** *23* (27), 3386-3397.

32. Kabe, R.; Notsuka, N.; Yoshida, K.; Adachi, C. Afterglow organic light-emitting diode. *Adv. Mater.* **2016,** *28* (4), 655-60.

33. An, Z.; Zheng, C.; Tao, Y.; Chen, R.; Shi, H.; Chen, T.; Wang, Z.; Li, H.; Deng, R.; Liu, X.; Huang, W. Stabilizing triplet excited states for ultralong organic phosphorescence. *Nat Mater* **2015,** *14* (7), 685-90.

34. Zhen, X.; Tao, Y.; An, Z.; Chen, P.; Xu, C.; Chen, R.; Huang, W.; Pu, K. Ultralong phosphorescence of water-soluble organic nanoparticles for in vivo afterglow imaging. *Adv. Mater.* **2017,** *29* (33), 1606665.

35. Cai, S. Z.; Shi, H. F.; Li, J. W.; Gu, L.; Ni, Y.; Cheng, Z. C.; Wang, S.; Xiong, W. W.; Li, L.; An, Z. F.; Huang, W. Visible-light-excited ultralong organic phosphorescence by manipulating intermolecular interactions. *Adv. Mater.* **2017,** *29* (35).

36. Shoji, Y.; Ikabata, Y.; Wang, Q.; Nemoto, D.; Sakamoto, A.; Tanaka, N.; Seino, J.; Nakai, H.; Fukushima, T. Unveiling a new aspect of simple arylboronic esters: Long-lived room-temperature phosphorescence from heavy-atom-free molecules. *J. Am. Chem. Soc.* **2017,** *139* (7), 2728-2733.

37. Chen, X. F.; Xu, C.; Wang, T.; Zhou, C.; Du, J. J.; Wang, Z. P.; Xu, H. X.; Xie, T. Q.; Bi, G. Q.; Jiang, J.; Zhang, X. P.; Demas, J. N.; Trindle, C. O.; Luo, Y.; Zhang, G. Q. Versatile room-temperature-phosphorescent materials prepared from n-substituted naphthalimides: Emission enhancement and chemical conjugation. *Angew. Chem. Int. Ed.* **2016,** *55* (34), 9872-9876.

38. Mao, Z.; Yang, Z. Y.; Mu, Y. X.; Zhang, Y.; Wang, Y. F.; Chi, Z. G.; Lo, C. C.; Liu, S. W.; Lien, A. A.; Xu, J. R. Linearly tunable emission colors obtained from a fluorescent-phosphorescent dual-emission compound by mechanical stimuli. *Angew Chem Int Edit* **2015,** *54* (21), 6270-6273.

39. Bolton, O.; Lee, K.; Kim, H. J.; Lin, K. Y.; Kim, J. Activating efficient phosphorescence from purely organic materials by crystal design. *Nat. Chem.* **2011,** *3* (3), 205-10.

40. Lee, D.; Bolton, O.; Kim, B. C.; Youk, J. H.; Takayama, S.; Kim, J. Room temperature phosphorescence of metal-free organic materials in amorphous polymer matrices. *J. Am. Chem. Soc.* **2013,** *135* (16), 6325-6329.

41. Kwon, M. S.; Lee, D.; Seo, S.; Jung, J.; Kim, J. Tailoring intermolecular interactions for efficient room-temperature phosphorescence from purely organic materials in amorphous polymer matrices. *Angew Chem Int Ed* **2014,** *53* (42), 11177-81.

42. Bolton, O.; Lee, D.; Jung, J.; Kim, J. Tuning the photophysical properties of metal-free room temperature organic phosphors via compositional variations in bromobenzaldehyde/dibromobenzene mixed crystals. *Chem. Mater.* **2014,** *26* (22), 6644-6649.

43. Kwon, M. S.; Yu, Y.; Coburn, C.; Phillips, A. W.; Chung, K.; Shanker, A.; Jung, J.; Kim, G.; Pipe, K.; Forrest, S. R.; Youk, J. H.; Gierschner, J.; Kim, J. Suppressing molecular motions for enhanced room-temperature phosphorescence of metal-free organic materials. *Nat. Commun.* **2015,** *6*, 8947.

44. Yu, Y.; Kwon, M. S.; Jung, J.; Zeng, Y.; Kim, M.; Chung, K.; Gierschner, J.; Youk, J. H.; Borisov, S. M.; Kim, J. Room-temperature-phosphorescence-based dissolved oxygen detection by core-shell polymer nanoparticles containing metal-free organic phosphors. *Angew. Chem. Int. Ed.* **2017,** *56* (51), 16207-16211.

45. Chaudhuri, D.; Sigmund, E.; Meyer, A.; Rock, L.; Klemm, P.; Lautenschlager, S.; Schmid, A.; Yost, S. R.; Van Voorhis, T.; Bange, S.; Hoger, S.; Lupton, J. M. Metal-free oled triplet emitters by side-stepping kasha's rule. *Angew Chem Int Edit* **2013,** *52* (50), 13449-13452.

46. Reineke, S.; Baldo, M. A. Room temperature triplet state spectroscopy of organic semiconductors. *Sci. Rep.* **2014,** *4*.

47. Bowers, D. T.; Tanes, M. L.; Das, A.; Lin, Y.; Keane, N. A.; Neal, R. A.; Ogle, M. E.; Brayman, K. L.; Fraser, C. L.; Botchwey, E. A. Spatiotemporal oxygen sensing using dual emissive boron dye polylactide nanofibers. *ACS Nano* **2014,** *8* (12), 12080-12091.

48. Contreras, J.; Xie, J. S.; Chen, Y. J.; Pei, H.; Zhang, G. Q.; Fraser, C. L.; Hamm-Alvarez, S. F. Intracellular uptake and trafficking of difluoroboron dibenzoylmethane-polylactide nanoparticles in hela cells. *ACS Nano* **2010,** *4* (5), 2735-2747.

49. DeRosa, C. A.; Seaman, S. A.; Mathew, A. S.; Gorick, C. M.; Fan, Z.; Demas, J. N.; Peirce, S. M.; Fraser, C. L. Oxygen sensing difluoroboron beta-diketonate polylactide materials with tunable dynamic ranges for wound imaging. *ACS Sens.* **2016,** *1* (11), 1366-1373.

50. Mathew, A. S.; DeRosa, C. A.; Demas, J. N.; Fraser, C. L. Difluoroboron beta-diketonate materials with long-lived phosphorescence enable lifetime based oxygen imaging with a portable cost effective camera. *Anal Methods* **2016,** *8* (15), 3109-3114.

51. Samonina-Kosicka, J.; Weitzel, D. H.; Hofmann, C. L.; Hendargo, H.; Hanna, G.; Dewhirst, M. W.; Palmer, G. M.; Fraser, C. L. Luminescent difluoroboron beta-diketonate peg-pla oxygen nanosensors for tumor imaging. *Macromol. Rapid Commun.* **2015,** *36* (7), 694-9.

52. Zang, L.; Shao, W.; Kwon, M. S.; Zhang, Z.; Kim, J. Photoresponsive luminescence switching of metal-free organic phosphors doped polymer matrices. *Adv. Optical Mater.* **2020,** *8*, 2000654.

53. Aitken, C. E.; Marshall, R. A.; Puglisi, J. D. An oxygen scavenging system for improvement of dye stability in single-molecule fluorescence experiments. *Biophys. J.* **2008,** *94* (5), 1826-35.

54. Li, J. W. J.; Chu, Y. Z.; Lee, B. Y. H.; Xie, X. L. S. Enzymatic signal amplification of molecular beacons for sensitive DNA detection. *Nucleic Acids Res.* **2008,** *36* (6).

55. Zou, B. J.; Ma, Y. J.; Wu, H. P.; Zhou, G. H. Ultrasensitive DNA detection by cascade enzymatic signal amplification based on afu flap endonuclease coupled with nicking endonuclease. *Angew Chem Int Edit* **2011,** *50* (32), 7395-7398.

56. Fozooni, T.; Ravan, H.; Sasan, H. Signal amplification technologies for the detection of nucleic acids: From cell-free analysis to live-cell imaging. *Applied Biochemistry and Biotechnology* **2017,** *183* (4), 1224-1253.

57. Scrimin, P.; Prins, L. J. Sensing through signal amplification. *Chem. Soc. Rev.* **2011,** *40* (9), 4488-4505.

58. Schubert, S.; Delaney, J. T.; Schubert, U. S. Nanoprecipitation and nanoformulation of polymers: From history to powerful possibilities beyond poly(lactic acid). *Soft Matter* **2011,** *7* (5), 1581-1588.

59. Siracusa, V. Food packaging permeability behaviour: A report. *Int. J. Polym. Sci.* **2012**, 302029.

60. Miller, K. S.; Krochta, J. M. Oxygen and aroma barrier properties of edible films: A review. *Trends Food Sci. Technol.* **1997,** *8* (7), 228-237.

61. Shah, R.; Eldridge, D.; Palombo, E.; Harding, I. Physicochemical stability. In *Lipid nanoparticles: Production, characterization and stability*, Springer: Cham, 2015; pp 75-97.

62. Mandal, B.; Mittal, N. K.; Balabathula, P.; Thoma, L. A.; Wood, G. C. Development and in vitro evaluation of core-shell type lipid-polymer hybrid nanoparticles for the delivery of erlotinib in non-small cell lung cancer. *Eur. J. Pharm. Sci.* **2016,** *81*, 162-171.

63. Mandal, B.; Bhattacharjee, H.; Mittal, N.; Sah, H.; Balabathula, P.; Thoma, L. A.; Wood, G. C. Core-shell-type lipid-polymer hybrid nanoparticles as a drug delivery platform. *Nanomedicine* **2013,** *9* (4), 474-491.

64. Fang, R. H.; Aryal, S.; Hu, C. M. J.; Zhang, L. F. Quick synthesis of lipid-polymer hybrid nanoparticles with low polydispersity using a single-step sonication method. *Langmuir* **2010,** *26* (22), 16958-16962.

65. Zhang, L. F.; Chan, J. M.; Gu, F. X.; Rhee, J. W.; Wang, A. Z.; Radovic-Moreno, A. F.; Alexis, F.; Langer, R.; Farokhzad, O. C. Self-assembled lipid-polymer hybrid nanoparticles: A robust drug delivery platform. *ACS Nano* **2008,** *2* (8), 1696-1702.

66. Yamada, H.; Urata, C.; Higashitamori, S.; Aoyama, Y.; Yamauchi, Y.; Kuroda, K. Critical roles of cationic surfactants in the preparation of colloidal mesostructured silica nanoparticles: Control of mesostructure, particle size, and dispersion. *ACS Appl. Mater. Interfaces* **2014,** *6* (5), 3491-3500.

67. Morsy, S. M. I. Role of surfactants in nanotechnology and their applications. *Int. J. Curr. Microbiol. App. Sci.* **2014,** *3*, 237-260.

68. Prior, S.; Kim, A.; Yoshihara, T.; Tobita, S.; Takeuchi, T.; Higuchi, M. Mitochondrial respiratory function induces endogenous hypoxia. *PLoS One* **2014,** *9* (2), e88911.

69. Lepore, A.; Portaccio, M.; De Tommasi, E.; De Luca, P.; Bencivenga, U.; Maiuri, P.; Mita, D. G. Glucose concentration determination by means of fluorescence emission spectra of soluble and insoluble glucose oxidase: Some useful indications for optical fibre-based sensors. *J Mol Catal B-Enzym* **2004,** *31* (4-6), 151-158.

70. Olivier, M.; Hollstein, M.; Hainaut, P. Tp53 mutations in human cancers: Origins, consequences, and clinical use. *Cold Spring Harb. Perspect. Biol.* **2010,** *2* (1), a001008.

71. Kandoth, C.; McLellan, M. D.; Vandin, F.; Ye, K.; Niu, B. F.; Lu, C.; Xie, M. C.; Zhang, Q. Y.; McMichael, J. F.; Wyczalkowski, M. A.; Leiserson, M. D. M.; Miller, C. A.; Welch, J. S.; Walter, M. J.; Wendl, M. C.; Ley, T. J.; Wilson, R. K.; Raphael, B. J.; Ding, L. Mutational landscape and significance across 12 major cancer types. *Nature* **2013,** *502*, 333-339.

72. Zilfou, J. T.; Lowe, S. W. Tumor suppressive functions of p53. *Cold Spring Harb. Perspect. Biol.* **2009,** *1* (5).

73. Kastenhuber, E. R.; Lowe, S. W. Putting p53 in context. *Cell* **2017,** *170* (6), 1062-1078.

74. Bettegowda, C.; Sausen, M.; Leary, R. J.; Kinde, I.; Wang, Y. X.; Agrawal, N.; Bartlett, B. R.; Wang, H.; Luber, B.; Alani, R. M.; Antonarakis, E. S.; Azad, N. S.; Bardelli, A.; Brem, H.; Cameron, J. L.; Lee, C. C.; Fecher, L. A.; Gallia, G. L.; Gibbs, P.; Le, D.; Giuntoli, R. L.; Goggins, M.; Hogarty, M. D.; Holdhoff, M.; Hong, S. M.; Jiao, Y. C.; Juhl, H. H.; Kim, J. J.; Siravegna, G.; Laheru, D. A.; Lauricella, C.; Lim, M.; Lipson, E. J.; Marie, S. K. N.; Netto, G. J.; Oliner, K. S.; Olivi, A.; Olsson, L.; Riggins, G. J.; Sartore-Bianchi, A.; Schmidt, K.; Shih, I. M.; Oba-Shinjo, S. M.; Siena, S.; Theodorescu, D.; Tie, J. N.; Harkins, T. T.; Veronese, S.; Wang, T. L.; Weingart, J. D.; Wolfgang, C. L.; Wood, L. D.; Xing, D. M.; Hruban, R. H.; Wu, J.; Allen, P. J.; Schmidt, C. M.; Choti, M. A.; Velculescu, V. E.; Kinzler, K. W.; Vogelstein, B.; Papadopoulos, N.; Luis, A. J. Detection of circulating tumor DNA in early- and late-stage human malignancies. *Sci. Transl. Med.* **2014,** *6* (224).

75. Schwarzenbach, H.; Hoon, D. S.; Pantel, K. Cell-free nucleic acids as biomarkers in cancer patients. *Nat. Rev. Cancer* **2011,** *11* (6), 426-37.

76. Ou, Z. Y.; Li, K.; Yang, T.; Dai, Y.; Chandra, M.; Ning, J.; Wang, Y. L.; Xu, R.; Gao, T. J.; Xie, Y.; He, Q.; Li, Y. W.; Lu, Q.; Wang, L.; Song, Z. Detection of bladder cancer using urinary cell-free DNA and cellular DNA. *Clin Transl Med* **2020,** *9* (1).

77. Park, Y. R.; Kim, Y. M.; Lee, S. W.; Lee, H. Y.; Lee, G. E.; Lee, J. E.; Kim, Y. T. Optimization to detect tp53 mutations in circulating cell-free tumor DNA from patients with serous epithelial ovarian cancer. *Obstet Gynecol Sci* **2018,** *61* (3), 328-336.

78. Bronkhorst, A. J.; Ungerer, V.; Holdenrieder, S. The emerging role of cell-free DNA as a molecular marker for cancer management. *Biomolecular Detection and Quantification* **2019,** *17*, 100087.

79. Du, B. A.; Li, Z. P.; Liu, C. H. One-step homogeneous detection of DNA hybridization with gold nanoparticle probes by using a linear light-scattering technique. *Angew Chem Int Ed Engl* **2006,** *45* (47), 8022-5.

80. Altintas, Z.; Tothill, I. E. DNA-based biosensor platforms for the detection of tp53 mutation. *Sensor Actuat B-Chem* **2012,** *169*, 188-194.

81. Jiang, T. S.; Minunni, M.; Wilson, P.; Zhang, J.; Turner, A. P. F.; Mascini, M. Detection of tp53 mutation using a portable surface plasmon resonance DNA-based biosensor. *Biosens. Bioelectron.* **2005,** *20* (10), 1939-1945.

82. Kanakasabapathy, M. K.; Sadasivam, M.; Singh, A.; Preston, C.; Thirumalaraju, P.; Venkataraman, M.; Bormann, C. L.; Draz, M. S.; Petrozza, J. C.; Shafiee, H. An automated smartphone-based diagnostic assay for point-of-care semen analysis. *Sci. Transl. Med.* **2017,** *9* (382), eaai7863.

Chapter 4

Ambient Delayed Fluorescence via Triplet-to-Singlet Energy Transfer from Purely Organic Phosphor

Zeng, Y.; Kim, J. "Ambient Delayed Fluorescence via Triplet-to-Singlet Energy Transfer from Purely Organic Phosphor." **2021**, *manuscript in preparation.*

4.1 Introduction

Intramolecular or intermolecular energy transfer processes play pivotal roles in the functions of a wide range of material systems, including the interactions and biofunctions of proteins[1,2] and nucleic acids,[3,4] properties of luminescent materials,[5] performance of light-emitting devices.[6,7] Fundamental understandings of energy transfer processes can yield valuable insights and design principles to manipulate the probability, rate, and efficiency of these processes, which ultimately affects the properties of electronic materials and their applications.

Well-established classic energy transfer mechanisms include singlet-to-singlet (S-S) Förster energy transfer, triplet-to-triplet (T-T) Dexter energy transfer, and S-S Dexter energy transfer. The mechanism of S-S energy transfer was initially explained by Förster theory,[8-10] and Förster resonance energy transfer (FRET) strategy has since been explored extensively in multi-chromophore assemblies for probing donor-acceptor distance and molecular conformation change (spectroscopic molecular ruler), designing chemical sensors, or achieving tunable fluorescence.[11-13] FRET occurs via dipole-dipole coupling between donor and acceptor, and typically manifests in the range of 1-10 nm. The rate (k_{ET}) and efficiency (Φ_{ET}) of FRET are inversely proportional to

the 6th power of donor-acceptor distance (Equation (1)). r is the distance between the donor and acceptor; R_0 is the Förster radius, a donor-acceptor distance corresponding to 50% FRET efficiency; k_R is the rate constant of donor's radiative decay (fluorescence); k_{NR} is the rate constant of other non-radiative decay processes depopulating the excited singlet state of the donor (S_n).

$$\Phi_{ET} = \frac{R_0^6}{R_0^6 + r^6} = \frac{k_{ET}}{k_{ET}+k_R+k_{NR}} \qquad (1)$$

In contrast, Dexter-type energy transfers between triplets (T-T) or singlets (S-S) are via electron transfer to exchange both spin and energy, which require direct orbital overlap between donor and acceptor.[14,15] Therefore, efficient Dexter energy transfer processes take place in short ranges (< 1 nm) and the rate constant exponentially decays as the donor-acceptor distance increases.

Unlike FRET or Dexter process, triplet-to-singlet energy transfer (T-S ET) involves donor and acceptor electronic states of different spin multiplicity and has been relatively less explored, even though strategies derived from this T-S ET concept using organometallic phosphors as triplet photosensitizers has been considerably exploited in electroluminescence to enhance the efficiency of fluorescent organic light-emitting diodes (OLEDs).[16-21] There are even fewer literature reports studying T-S ET in purely organic luminescent materials in the context of photoluminescence.[22-25] This could be largely caused by the unclear underlying mechanism that governs such photophysical process, which in turn leads to the lack of design principles for various applications. In fact, there are divided opinions in the scientific community on the matter of spin angular momentum conservation during energy transfer. One school of thought follows Wigner's spin conservation rule,[26] which is also presented in classic textbooks on molecular photochemistry of organic molecules[27], whereby a photochemical or a photophysical process is spin-allowed if the spin angular momentum space spanned by the reactants intersects the spin angular momentum

space spanned by the products. In the context of energy transfer, the process is thermodynamically viable if the total electron spin does not change before and after. Both Förster and Dexter energy transfer mechanisms observe this rule. However, in the process of T-S ET, an excited triplet (T_n) interacts with a ground singlet (S_0) and subsequently produces a ground singlet (S_0) and an excited singlet (S_n), and hence the total spin multiplicity is not conserved, and such process is supposed to be quantum-mechanically forbidden. Guo *et al.* experimentally investigated intramolecular dipolar energy transfer in organometallic complexes where the donor and acceptor moieties were linked together, and found that the dipolar energy transfer only occurs in the material system where the spin conservation condition is satisfied.[28] One caveat the authors stated was the spin constraint would likely manifest more strictly in inorganic materials rather than organic systems. Another school of thought supports the notion that T-S ET can occur via FRET without conserving the spin angular momentum. Since the resonance energy transfer mechanism is based on oscillating dipole-dipole coupling, which is essentially electrostatic interaction, the total spin angular momentum of the involved electronic states should have no influence on the probability or efficiency of the energy transfer process. Cravcenco *et al.*[29] described a donor (Ir^{III} complex)-bridge-acceptor (perylene) dyad molecule in which intramolecular T-S ET was observed and the rate constant of energy transfer matched well with the Förster model. The requirement for T-S ET to efficiently occur is a strong oscillation strength from the excited triplet state of the donor, i.e., the donor is efficiently phosphorescent.[16] This can be realized by increasing the spin-orbit coupling (SOC) strength in the donor, such as incorporating heavy atoms or aromatic carbonyls into donor structures.[30-32]

In this chapter, we show that it is possible to achieve efficient intermolecular T-S ET in purely organic chromophore systems through a pseudo-FRET pathway. A phosphor donor with

long-lived, strong organic room-temperature phosphorescence and an organic fluorescence acceptor were co-assembled and embedded in rigid polymeric nanoparticles. The intermolecular energy transfer from the donor phosphor to the acceptor fluorophore was investigated by spectroscopic methods. Such T-S ET process quenches the RTP emission from the excited donor triplet state and sensitizes the excited singlet state of the acceptor, which induces ambient delayed fluorescence (DF). The efficiency of T-S ET in the demonstrated donor-acceptor pair was as high as 75.5% under our experimental conditions, and is tunable by varying the encapsulation ratio of donor and acceptor in the nanoparticles. The rate of T-S ET (k_{ET}) and the lifetime of the resulting ambient DF is modulated by donor's SOC strength, with stronger donor SOC leading to faster k_{ET} and shorter DF lifetime. The T-S ET process studied here can be employed as a material system design strategy to harvest the energy of excited triplet state tailored toward different applications, which includes increasing the rate of light extraction from the excited triplet states to boost OLED efficiency, and achieving persistent delayed red/NIR luminescence with high quantum efficiency.

4.2 Results and Discussion

4.2.1 Chromophores co-assembly in rigid nanoparticles

To demonstrate the concept and investigate the underlying mechanism of T-S, we co-assembled the organic phosphor donor and the fluorophore acceptor into a single NP. This represents an effective strategy to ensure chromophores are in close proximity to each other, a factor that drives high energy transfer efficiency. Specifically, through a facile one-step nanoprecipitation protocol utilizing a sharp solubility change of host materials in miscible dissimilar solvents,[33] the organic phosphor donors and the fluorophore acceptors are co-embedded homogenously in rigid polymeric NPs.

We chose poly(4-bromostyrene) (PS4Br) or isotactic poly(methyl methacrylate) (iPMMA) as the polymer matrix to host the chromophores (Figure 4.1a) because of their optical inertness, high rigidity, and different oxygen permeability. The high rigidity of the host polymer is required to effectively suppress the vibrational energy dissipation of the metal-free phosphor[34-36] hence the triplet state of the donor is preserved for the subsequent T-S ET. Additionally, while iPMMA is an excellent oxygen barrier, PS4Br on the other hand is oxygen permeable.[37-39] As we discussed in Chapter 2 and Chapter 3, the phosphorescence emission (i.e., triplet state energy) of purely organic phosphors is highly susceptible to oxygen quenching. Therefore, comparing the photophysical processes between the phosphor donor and the fluorophore acceptor in PS4Br and iPMMA NPs systems will provide insight into the effect of oxygen quenching of triplet state on T-S ET efficiency.

A synthetic purely organic phosphor Br6A and a commercially available red fluorescent dye Nile red (NR) with a decent quantum efficiency[40] were chosen as the pseudo-FRET pair (Figure 4.1). Br6A is a green RTP emitter (λ_{em} = 530 nm) with strong spin-orbit coupling (SOC) reported by the Kim lab previously[41], was used as the organic phosphor donor in the NP assembly. The absorption of the acceptor NR has a good spectral overlap with Br6A's RTP emission, i.e., a small energy gap between the triplet state of Br6A and the singlet state of NR, which is a prerequisite for efficient ET processes.

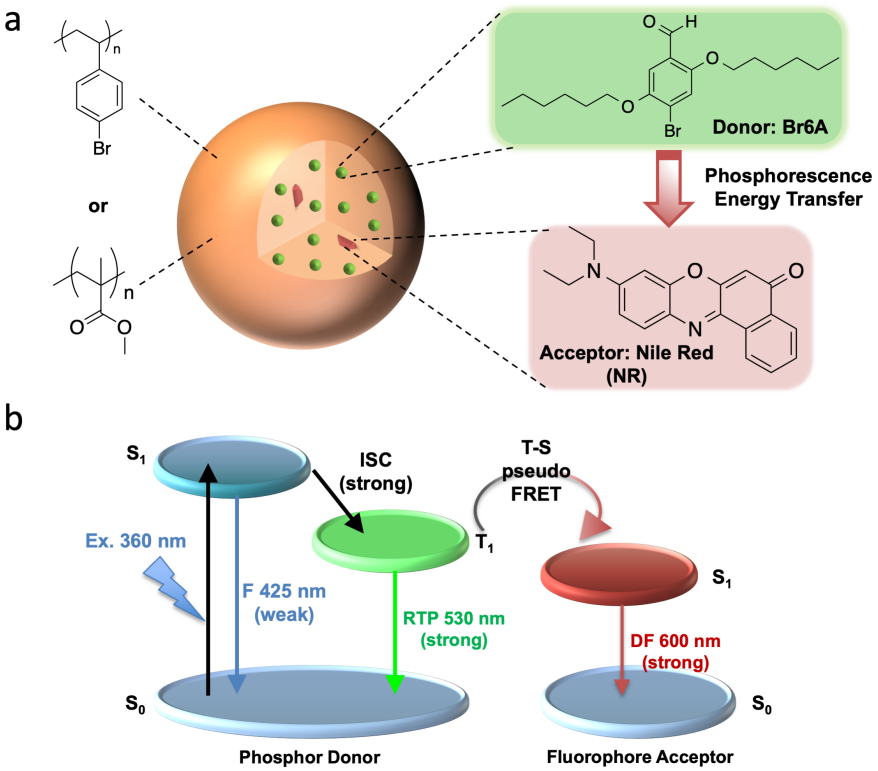

Figure 4.1 | Donor-Acceptor co-assembly and proposed triplet-to-singlet energy transfer pathway. **a**, Schematic illustration of the rigid nanoparticle assembly where the phosphorescence energy transfer takes place and molecular structures of the donor phosphor Br6A, acceptor fluorophore NR, and host polymer matrices. **b,** Simplified Jablonski diagram showing the photophysical processes in the pair of donor phosphor Br6A and acceptor fluorophore NR after photoexcitation at 360 nm. S_0, S_1, and T_1 are the singlet ground state, first excited singlet state, and excited triplet state of the chromophores, respectively. ISC = intersystem crossing. T-S pseudo-FRET = triplet-to-singlet pseudo Förster Resonance Energy Transfer. F, RTP, and DF are prompt fluorescence, room-temperature phosphorescence, and delayed fluorescence, respectively.

At a polymer concentration of 1mg/mL in the internal organic phase for nanoprecipitation, a series of narrow-dispersed Br6A-NR-PS4Br NPs with various donor Br6A and acceptor NR encapsulation ratio can be produced. Dynamic light scattering (DLS) data indicate that these NPs have an average hydrodynamic diameter of approximately 150 nm and polydispersity index (PDI) of 0.1 in Milli-Q water (Figure 4.2a). The similarity in NP sizes and PDIs for a broad range of donor and acceptor composition allows us to readily tune donor-acceptor distance by varying the

encapsulation ratio. Furthermore, we kept the total chromophore loadings in the polymer matrix under 2 wt% to eliminate potential Dexter energy transfer.[21]

4.2.2 Br6A-NR triplet-singlet energy transfer in PS4Br NPs

Steady state emission spectrum of Br6A-PS4Br NPs confirmed an intense RTP peak at 530 nm and a weak fluorescence peak around 425 nm (Figure 4.2b). The UV-Vis spectrum of NR in tetrahydrofuran (THF) solution at 5 μg/ml shows a major absorption band in the 450-600 nm region with maxima at 530 nm, which confirms the good spectral overlap with the RTP emission of Br6A but negligible overlap with the fluorescence emission of Br6A. Therefore, S-S FRET from Br6A to NR would be unlikely. Due to its broad absorption bands, NR can be excited by both 530 nm and 360 nm light, and fluoresce at around 592 nm (peak maxima). While it was highly fluorescent under 530 nm excitation, NR's emission was very minimal under 360 nm.

When 1 wt% Br6A was doped with 0.1 wt% NR in the PS4Br NPs, steady state emission spectrum (λ_{ex} = 360 nm) under argon (Ar) atmosphere showed a decrease of Br6A RTP peak around 530 nm and a concurrent drastic enhancement of NR fluorescence peak around 592 nm compared to ambient conditions (Figure 4.2c). This was also evident from the visible color change from green (pure RTP of Br6A) to orange (combination of minor green RTP and major red fluorescence) in PS4Br NPs solutions (Figure 4.2e). Time-resolved emission spectrum (500 μs delay) further supports the energy shift from the long-lived green RTP to the red DF. Notably, under ambient conditions, there was no significant RTP peak of Br6A nor red DF peak of NR (inset of Figure 4.2c), largely due to the predominant oxygen quenching of Br6A triplet energy competing with intermolecular energy transfer.[39,42] These results indicate that the energy transfer

process in the present study involves the oxygen-sensitive triplet state of the donor and the singlet state of the acceptor, i.e., T-S ET.

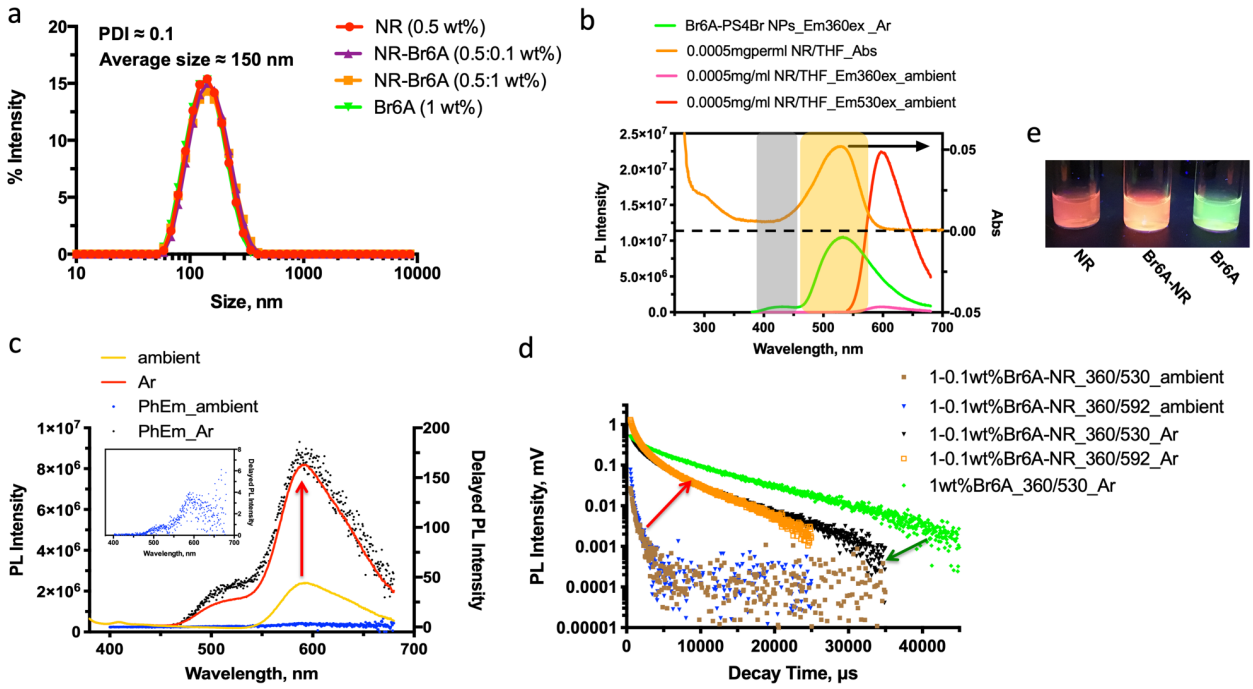

Figure 4.2 | Chemophysical and photophysical characterizations of triplet-to-singlet energy transfer in Br6A-NR-PS4Br NPs. **a**, Hydrodynamic size (diameter, nm) distribution of Br6A-NR-PS4Br NPs measured by dynamic light scattering. NPs with various donor Br6A and acceptor NR were fabricated from a single-step nanoprecipitation process, with average hydrodynamic diameters of ~150 nm (PDI: ~0.1). **b**, Absorption spectrum of NR in THF, steady state emission of Br6A-PS4Br NPs (λ_{ex} = 360 nm) and NR in THF (λ_{ex} = 360 nm and 530 nm). The absorption of acceptor shows a good spectral overlap with the emission of donor Br6A. **c,** Steady state, and time-resolved emission (PhEm) of 1-0.1 wt% Br6A-NR-PS4Br NPs under ambient and Ar conditions (λ_{ex} = 360 nm). The decreased peak around 530 nm is the green RTP of Br6A and the enhanced peak around 592 nm matches with the red fluorescence of NR and is of delayed nature. **d,** Emission decay profiles of 1 wt%Br6A alone and further doped with 0.1 wt% NR in PS4Br NPs monitored at 530 nm (RTP) or 592 nm (DF), showing a quenching of the donor Br6A's triplet lifetime along with a prolonging in the acceptor NR's singlet lifetime. **e,** Photographs of NR alone, Br6A-NR co-assembled, and Br6A alone in PS4Br NPs suspensions under a 365 nm UV-lamp, showing a ref shift in the emission compared to Br6A alone when it is doped with NR.

Lifetime (τ) measurement (Figure 4.2d) of the green RTP of Br6A in PS4Br NPs under Ar monitored at 530 nm showed a decrease in the average lifetime (τ_{avg}) from 5.60 ms (pure Br6A) to

2.22 ms (1 wt% Br6A doped with 0.1 wt% NR), yielding a non-radiative T-S ET efficiency Φ_{ET} of 60.4% (Table 4.1). As expected, the average lifetime of the red DF of NR monitored at 592 nm was prolonged to 0.959 ms under Ar. It is important to note that, even under ambient conditions, an increase in the average lifetime of the red DF can already be observed, from 3.8 ns reported in the literature[43] to 188 μs in our study. This suggests that such T-S ET process from donor Br6A to acceptor NR is fast enough to compete with the oxygen quenching of the triplet state in Br6A with the caveat that its efficiency is much higher in oxygen-free environments. These decay profiles also indicate that the non-radiative T-S ET is the predominant energy transfer pathway in our materials system rather than an emission-reabsorption process, where donor's lifetime is not expected to change.

Table 4.1 | Summary of lifetime τ components and energy transfer efficiency Φ_{ET} in Br6A-NR-PS4Br NPs

wt% in PS4Br NPs	τ fast (μs)	τ slow (μs)	% fast	τ_{avg}[a] (ms)	Energy Transfer Efficiency Φ_{ET}[b] (%)
1 Br6A_360/530_Ar				5.60	
1-0.1 Br6A-NR_360/530_ambient	274.8	1291	94.37	0.332	
1-0.1 Br6A-NR_360/592_ambient	169.9	759.8	96.96	0.188	
1-0.1 Br6A-NR_360/530_Ar	944.5	4703	66.18	2.22	60.4
1-0.1 Br6A-NR_360/592_Ar	512	3027	82.22	0.959	

[a]The average lifetime τ_{avg} was calculated according to τ_{avg} = τ fast * percent fast + τ slow * (1-percent fast).
[b]Energy transfer efficiency was calculated according to $\Phi_{ET} = 1-\tau_{DA}/\tau_{D0}$.[44] τ_{DA}: donor lifetime in the presence of acceptor. τ_{D0}: pure donor lifetime without any acceptor.

4.2.3 Br6A-NR triplet-singlet energy transfer in iPMMA NPs

To further suppress oxygen quenching of donor's triplet exciton and promote T-S ET efficiency, we then used iPMMA as the polymer matrix to incorporate donor Br6A and acceptor NR into nanoparticles by a similar means of nanoprecipitation. When 1 wt% Br6A was co-

encapsulated with 1 wt% NR in the iPMMA NPs (~150 nm), steady state emission spectra (λ_{ex} = 360 nm) under both ambient and argon (Ar) atmosphere showed a substantial decrease of Br6A RTP peak around 530 nm and a concomitant significant enhancement of a peak centered around 608 nm (Figure 4.3a). The 608 nm peak matches with the fluorescence emission of NR alone in the iPMMA NPs excited by either 360 nm or 530 nm. The normalized time-resolved emission spectra (500 μs delay) further support the gradually increasing energy migration from the green RTP to the red DF as the doping ratio of acceptor NR increases (Figure 4.3b). This also confirms the long-lived character of the red DF. Furthermore, the normalized time-resolved excitation spectra revealed the same 360 nm excitation peak that contributes to the 530 nm RTP emission in Br6A-iPMMA NPs and the 608 nm DF emission in Br6A-NR-iPMMA NPs (1:1 wt%). As discussed in the previous section, NR's prompt red fluorescence emission is mainly attributed to the 530 nm absorption band. Steady state excitation scan further corroborated the increased contribution of 360 nm excitation to the red 608 nm fluorescence (Figure 4.3c). Taking these results into consideration, it is evident that the long-lived triplet excitons of donor Br6A are the only source of the delayed population of the singlet state of the acceptor NR via an efficient T-S ET pathway. Notably, while the RTP emission of Br6A alone in iPMMA NPs exhibited an increase under Ar compared to ambient conditions, the intensity of the RTP peak of Br6A and the DF peak of NR in Br6A-NR-iPMMA NPs were almost the same in both conditions. This suggests that at 1 wt%: 1wt% Br6A:NR in the iPMMA NPs, the T-S ET process is so efficient that the effect from the competing oxygen quenching pathway is almost negligible.

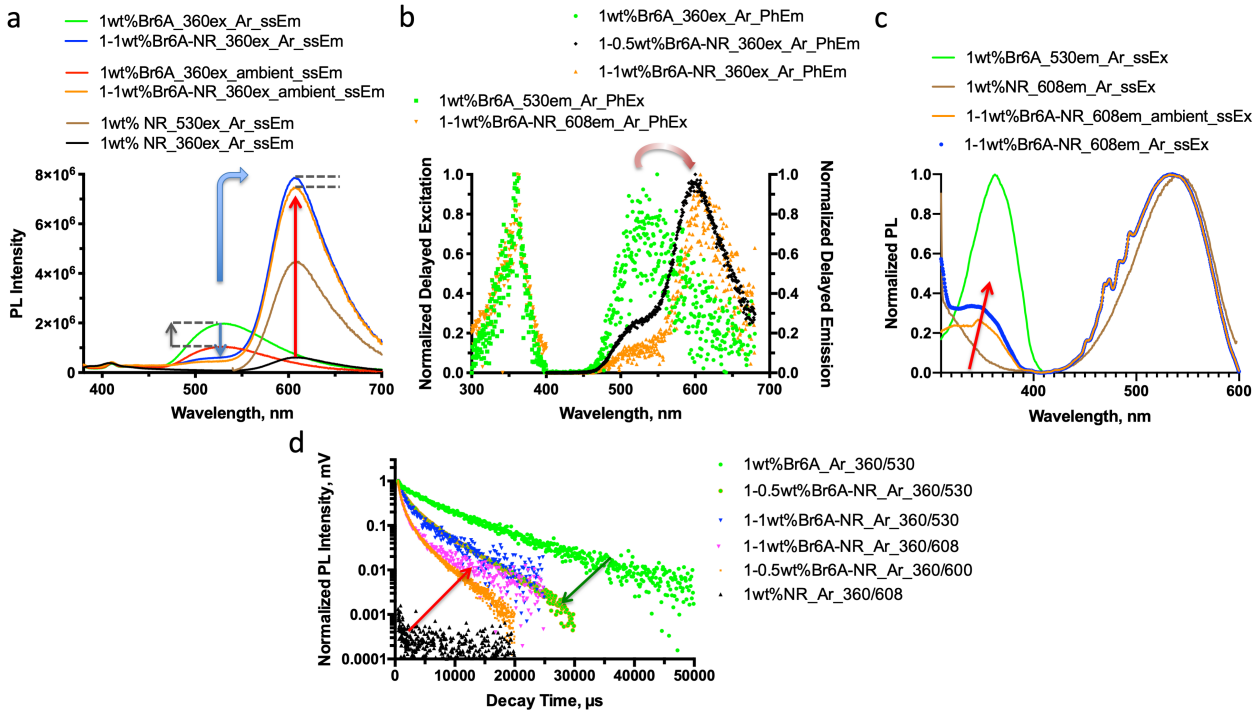

Figure 4.3 | Photophysical characterizations of triplet-to-singlet energy transfer in Br6A-NR-iPMMA NPs. a, Steady state emission spectra of 1 wt% Br6A alone, 1-1 wt% Br6A-NR co-encapsulated, and 1 wt% NR alone in iPMMA NPs under ambient and Ar conditions (360ex and 530ex denote λ_{ex}). A quenching in the green RTP band of Br6A and a concurrent boost of the red fluorescence band of NR was clearly observed, indicating a non-radiative energy transfer from Br6A triplet to NR singlet. **b,** Normalized time-resolved emission and excitation spectra of Br6A-NR-iPMMA NPs with different weight percent of acceptor NR, showing further red shift in the delayed emission with higher doping ratio of acceptor. The delayed red fluorescence of NR at 608 nm was contributed by 360 nm excitation, the same excitation that contributed to the RTP band of Br6A, indicating Br6A triplet excitons were the source that populated the excited singlet state of NR. **c,** Normalized steady state excitation spectra of 1 wt% Br6A alone, 1-1 wt% Br6A-NR co-encapsulated, and 1 wt% NR alone in iPMMA NPs, further confirmed the increased contribution of 360 nm excitation to the red 608 nm fluorescence in the donor-acceptor co-assembled NPs, most prominent under Ar condition. **d,** Emission decay profiles of Br6A-NR-iPMMA NPs with different weight percent of acceptor NR monitored at 530 nm (RTP) or 608 nm (DF), showing a gradual quenching of the donor Br6A's triplet lifetime along with a increasing in the acceptor NR's singlet lifetime.

Lifetime (τ) measurement (Figure 4.3d) of the green RTP of Br6A in iPMMA NPs under Ar monitored at 530 nm showed a gradual decrease in τ_{avg} from 6.20 ms (pure 1 wt% Br6A) to 1.87 ms in the presence of 0.5 wt% NR, and further down to 1.52 ms with 1 wt% NR doped in. These resulted in non-radiative T-S ET efficiencies of 69.8% and 75.5%, respectively (Table 4.2).

To the best of our knowledge, this materials system demonstrates one of the highest energy transfer efficiencies in intermolecular T-S ET processes reported for purely organic systems. The τ_{avg} of the red DF of NR monitored at 600 nm was prolonged to about 0.64 ms for both the 0.5 wt% and 1 wt% NR doped NPs. This lifetime is relatively shorter compared to that of Br6A-NR-PS4Br NPs at a doping ratio of 1wt%:0.1wt%. We think this is likely caused by the shortened distance between the donor and the acceptor at a higher loading ratio in the iPMMA NPs system, which in turn increases the rate of T-S ET process (k_{ET}). Additionally, this further confirms that the long-lived triplet excitons of donor Br6A are the source of the delayed population of the singlet state of the acceptor NR.

Table 4.2 | Summary of lifetime τ components and energy transfer efficiency Φ_{ET} in Br6A-NR-iPMMA NPs

wt% in iPMMA NPs_Ar	τ fast (μs)	τ slow (μs)	% fast	τ_{avg}[a] (ms)	Energy Transfer Efficiency Φ_{ET}[b] (%)
1 Br6A_360/530				6.20	
1-1 Br6A-NR_360/530	785.5	4049	77.52	1.52	75.5
1-1 Br6A-NR_360/608	417.1	2502	89.63	0.633	
1-0.5 Br6A-NR_360/530	804.5	4122	67.77	1.87	69.8
1-0.5 Br6A-NR_360/600	396.4	2114	85.5	0.65	

[a]The average lifetime τ_{avg} was calculated according to τ_{avg} = τ fast * percent fast + τ slow * (1-percent fast). [b]Energy transfer efficiency was calculated according to $\Phi_{ET} = 1-\tau_{DA}/\tau_{D0}$.[44] τ_{DA}: donor lifetime in the presence of acceptor. τ_{D0}: pure donor lifetime without any acceptor.

Although the decay profiles in our co-assembled materials system indicate a predominant non-radiative T-S ET pathway rather than a trivial energy transfer based on reabsorption, we next sought out to rule out the possibility of emission-reabsorption process. As a control, we encapsulated 1 wt% Br6A and 1 wt% NR in separate iPMMA NPs and then probed the photophysical processes in the mixture of the two corresponding NPs suspension at a volume ratio

of 2:1. As shown in Figure 4.4a, steady state emission scans displayed a physical addition of two separate emission profiles of Br6A and NR. Time-resolved emission spectra suggests that the delayed emission from the mixture is predominately the RTP peak of Br6A, and the red fluorescence emission is mainly of prompt character rather than long-lived. Therefore, the physical separation of the two chromophores shuts off the T-S ET pathway and Br6A undergoes phosphorescent radiative decay. Lifetime analyses (Figure 4.4b and Table 4.3) revealed a similar τ_{avg} of Br6A of the mixture compared to that of Br6A-iPMMA NPs alone. Interestingly, the lifetime of NR of the mixed suspension was prolonged to 2.86 ms, even longer than that of the co-encapsulated Br6A-NR-iPMMA (1wt%:0.5wt%) where there was efficient T-S ET present. We think this is likely due to emission-reabsorption in the mixed NPs suspension with an overall acceptor NR concentration at 0.3 wt%, when there is no T-S ET pathway available. In such a case, the apparent lifetime of acceptor's fluorescence is dictated by the combination of donor's phosphorescence lifetime and acceptor's inherent prompt fluorescence lifetime. However, in the previous donor-acceptor co-assembled NPs, the T-S ET pathway is readily available and occurs at a much faster rate than the reabsorption process in which the long-lived phosphorescent photon needs to be emitted first. Thus, it is reasonable to rule out the possibility of reabsorption in Br6A-NR co-encapsulated NPs. The calculated Φ_{ET} is based on acceptor's contribution to donor's lifetime reduction, hence it is only considering the predominant non-radiative T-S ET and not the trivial radiative emission-reabsorption process since the later does not affect donor's lifetime.

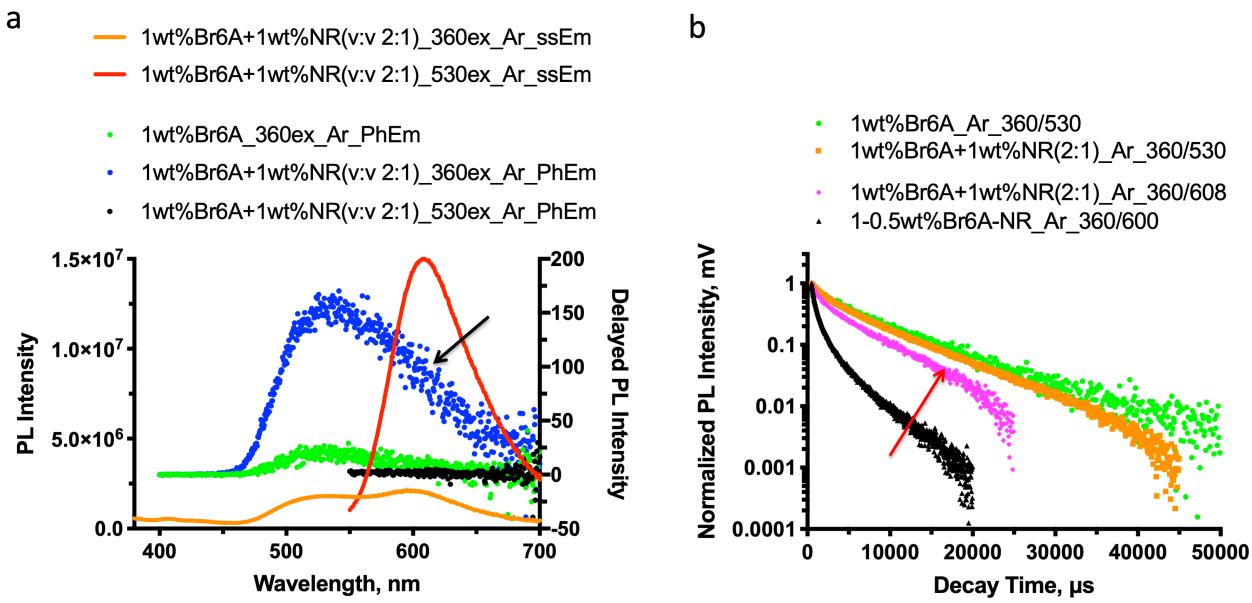

Figure 4.4 | Photophysical characterizations of iPMMA-NPs mixture with donors and acceptors encapsulated separately. 1 wt% Br6A-iPMMA NPs and 1 wt% NR-iPMMA NPs mixture at a 2:1 volume ratio. **a**, Steady state (ssEm) and time-resolved emission (PhEm) of the mixture under Ar (360ex and 530ex denote λ_{ex}). Br6A underwent phosphorescent radiative decay, and the absence of delayed red fluorescence from the mixture indicates the T-S ET pathway was shut off. **b**, Emission decay profiles (λ_{ex} = 360 nm) of the NPs mixture. No significant change in donor Br6A lifetime suggests no non-radiative energy transfer. The substantial increase in the acceptor NR's lifetime (ms regime) in the mixture compared to that in the co-assembled NPs is likely caused by emission-reabsorption.

Table 4.3 | Summary of lifetime τ components in the mixture suspension of 1 wt% Br6A-PS4Br NPs and 1wt% NR-iPMMA NPs (v:v 2:1)

wt% in iPMMA NPs_Ar	τ fast (µs)	τ slow (µs)	% fast	τ_{avg}[a] (ms)
1 Br6A NPs + 1 NR NPs_360/530	1501	7535	42.12	4.99
1 Br6A NPs + 1 NR NPs_360/608	784.3	5812	58.64	2.86

[a]The average lifetime τ_{avg} was calculated according to τ_{avg} = τ fast * percent fast + τ slow * (1-percent fast).

4.2.4 Effect of donor spin-orbit coupling strength on triplet-singlet energy transfer efficiency

T-S ET is essentially an outlier in the classic energy transfer mechanisms landscape. We hypothesized that strong SOC and consequently efficient RTP in the donor molecules can override the spin constraints governed by Wigner spin conservation law. In such cases, the strong oscillation

strength of the donor's phosphorescence emission often indicates some singlet character in the donor's excited triplet state, which facilitates dipole–dipole coupling between the excited donor and ground singlet state of the acceptor. We termed this T-S ET process pseudo-FRET. Organometallic phosphors such as Tris(2-phenylpyridine)iridium (III) ($Ir(ppy)_3$) are known to have strong SOC due to the heavy metal effect.[45,46] $Ir(ppy)_3$ and its derivatives have been widely used as phosphorescent sensitizers in fluorescent OLEDs[16-21], in which the electrically excited triplet exciton of $Ir(ppy)_3$ undergoes energy transfer to the ground singlet state of a fluorophore. However, the mechanism of such intermolecular energy transfer process has rarely been elucidated in the context of photoluminescence.[29]

To investigate how the donor phosphor's SOC strength plays a role in pseudo-FRET efficiency, we co-assembled $Ir(ppy)_3$ and NR in narrow-dispersed (PDI: 0.1) ~118 nm PS4Br NPs (Figure 4.5a,c). $Ir(ppy)_3$ emits strong green RTP in THF solution under ambient conditions, with its absorption and emission bands in similar regions compared to those of Br6A. This result experimentally confirmed that $Ir(ppy)_3$ has a much stronger SOC than Br6A, and as a consequence, its RTP is not as sensitive to molecular vibration or oxygen quenching. UV-Vis spectrum of NR showed a good spectral overlap with the RTP emission of $Ir(ppy)_3$ (Figure 4.5b). These are good indicators of a high T-S pseudo-FRET efficiency in $Ir(ppy)_3$-NR-PS4Br NPs.

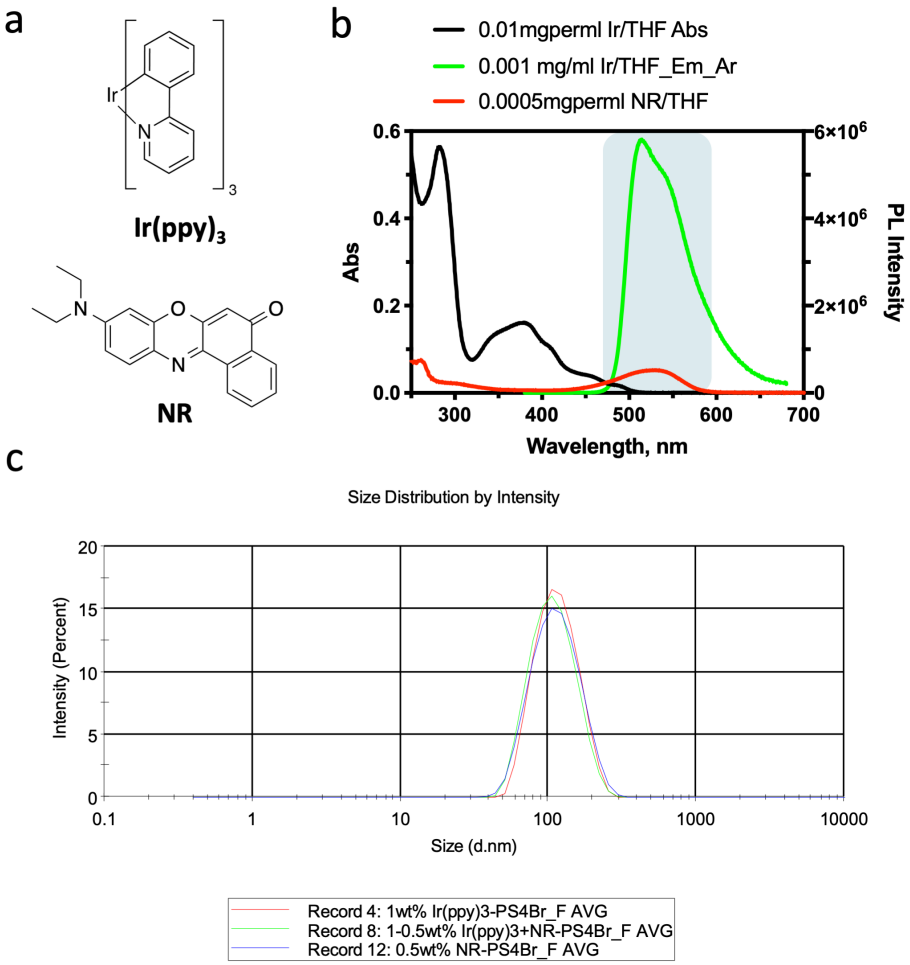

Figure 4.5 | Ir(ppy)$_3$-NR as the donor-acceptor pair for triplet-to-singlet energy transfer in PS4Br NPs. **a**, Molecular structures of the donor organometallic phosphor Ir(ppy)$_3$ and fluorescent acceptor NR. **b**, Absorption spectrum of NR, Ir(ppy)$_3$, and steady state emission of Ir(ppy)$_3$ (λ_{ex} = 360 nm) in THF solutions, showing a good spectral overlap between NR absorption and Ir(ppy)$_3$ emission. The major absorption band of Ir(ppy)$_3$ around 360 nm is not expected to excite NR effectively. **c,** Hydrodynamic size (diameter, nm) distribution of Ir(ppy)$_3$-NR-PS4Br NPs measured by dynamic light scattering. NPs with various donor Br6A and acceptor NR compositions were fabricated via nanoprecipitation, with average hydrodynamic diameters of ~118 nm (PDI: ~0.1).

Comparing steady state emissions (λ_{ex} = 360 nm) between Ir(ppy)$_3$ alone, NR alone, and Ir(ppy)$_3$-NR at 1 wt%:0.5 wt% in PS4BR NPs revealed a similar trend of red shift, a decrease at the green RTP peak of Ir(ppy)$_3$ and enhancement at the red fluorescence peak of NR (Figure 4.6a). In contrast, the mixture of separate 1wt% Ir(ppy)$_3$-PS4Br NPs and 0.5 wt% NR-PS4Br NPs (v:v =

2:1) did not show a red shift in the emission spectra (Figure 4.6b) but a physical addition of the two corresponding chromophores' emission profiles, indicating there was no pseudo-FRET process once the donor and the acceptor were separated at a long distance. These results were evident from the visible color change in PS4Br NPs solutions (Figure 4.6c), green from pure RTP of $Ir(ppy)_3$, to orange from a combination of minor green RTP and major red DF, and to yellow from an addition of green RTP and red fluorescence of almost equal intensity. Lifetime measurement using Time-Correlated Single Photon Counting (TCSPC) method (Figure 4.6d) further confirmed that the non-radiative pseudo-FRET from $Ir(ppy)_3$ to NR contributes to the reduction of donor's τ_{AVG} from 1.3 μs to 0.5 μs, yielding an energy transfer efficiency Φ_{ET} of 61.5%. Interestingly, this is on a similar magnitude compared to those of the material systems where the purely organic Br6A was used as the phosphor donor. This suggests pseudo-FRET efficiency does not scale with donor phosphor's SOC strength, but once a threshold enough to overcome the spin conservation is reached, pseudo-FRET can happen efficiently. However, donor phosphor's SOC strength for $T_1 \rightarrow S_0$ does dictate the rate of pseudo-FRET k_{ET} and in turn the DF lifetime of the acceptor. In $Ir(ppy)_3$-NR-PS4Br NPs, NR's fluorescence lifetime was increased to 140 ns whereas in Br6A-NR-PS4Br NPs, it was prolonged to nearly 1 ms.

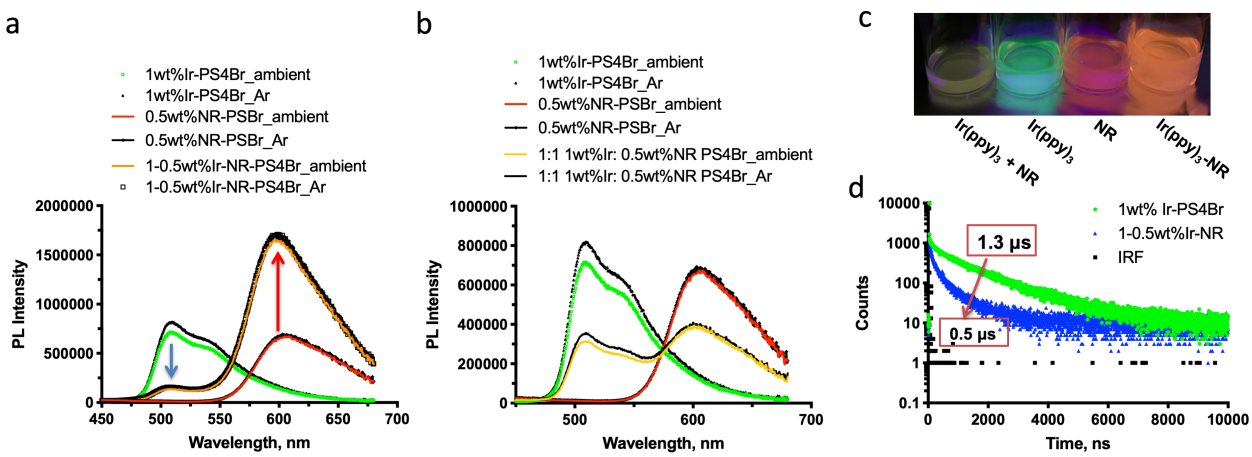

Figure 4.6 | Photophysical characterizations of triplet-to-singlet energy transfer in Ir(ppy)$_3$-NR-PS4Br NPs. a, Steady state emission spectra of 1 wt% Ir(ppy)$_3$ alone, further doped with 0.5 wt% NR, and 0.5 wt % NR alone in PS4Br NPs under ambient and Ar conditions (λ_{ex} =360 nm). A quenching in the green RTP band of Ir(ppy)$_3$ along with a boost in the red fluorescence band of NR was observed, indicating a non-radiative energy transfer from Ir(ppy)$_3$ triplet to NR singlet. **b,** Steady state emissions (λ_{ex} =360 nm) of separate and mixture of Ir(ppy)$_3$-PS4Br NPs and NR-PS4Br NPs under both ambient and Ar conditions. The absence of a red shift in the emission profile of the NPs mixture indicates the lack of non-radiative T-S ET. **c,** Photographs of Ir(ppy)$_3$-PS4Br and NR-PS4Br NPs mixture, Ir(ppy)$_3$-PS4Br NPs alone, NR-PS4Br NPs alone, and co-assembled Ir(ppy)$_3$-NR-PS4Br NPs (from left to right) under a 365 nm UV-lamp. In the donor-acceptor co-assembled NPs, there was a red shift in emission color due to efficient T-S ET, yielding an overall color of orange, whereas the mixture showed yellow which is the addition of the inherent colors from the two separate NPs. **d,** Emission decay profiles of Ir(ppy)$_3$ alone and doped with NR in PS4Br NPs measured by Time-Correlated Single Photon Counting. λ_{ex} =360 nm and monitored at 530 nm (RTP of Ir(ppy)$_3$). A significant reduction in donor Ir(ppy)$_3$ lifetime implies an efficient T-S ET pathway.

4.3 Conclusion and Outlook

In summary, we have demonstrated efficient T-S ET via pseudo-FRET mechanism in purely organic materials, expanding the conventional energy transfer pathways. T-S ET from long-lived triplet excitons in a metal-free organic phosphor donor to the ground singlet state of a fluorescent acceptor in a co-assembled rigid polymeric NPs system results in ambient DF, with an energy transfer efficiency as high as 75.5%. Such T-S ET process also induces an unprecedentedly large Stokes shift of 240 nm. The energy transfer efficiency can be tuned by the encapsulation ratio of donor and acceptor. At higher acceptor loading ratios, the average distance between the

donor and the acceptor is shorter in NPs of a defined size, and donor molecules are surrounded by more acceptor molecules, hence higher T-S ET efficiencies. Donor's $T_1 \rightarrow S_0$ SOC strength influences the rate of pseudo-FRET and in turn the lifetime of the induced ambient DF. Stronger SOC leads to faster k_{ET} and shorter DF lifetime. Further studies such as a systematic investigation of T-S ET efficiencies over a range of controlled donor-acceptor distances would allow us to gain more insight into how the pseudo-FRET mechanism deviates from the classic Förster model. Atom transfer radical polymerization (ATRP) and Langmuir-Blodgett (LB) are attractive approaches to construct polymer layers of well-defined length as space rulers between the donor and acceptor.

Purely organic RTP materials have been around for about a decade since the pioneering work from the Kim group[41] and the Tang group,[47] yet it is still challenging to achieve organic long-lived emission and high quantum efficiency simultaneously through molecular design, especially toward the red and NIR region.[31,32,48] By utilizing T-S ET, we can envision that an organic phosphor with a long RTP lifetime paired with a highly fluorescent red or NIR dye can result in bright afterglow red or NIR fluorescence. The concept of T-S ET also serves as an effective strategy to achieve DF with narrow emission when the acceptor fluorophore has a sharp emission profile, an alternative to thermally activated delayed fluorescence (TADF) which is difficult to molecular engineer and often has color purity issues.[49,50] The presence of the acceptor fluorophore essentially speeds up the rate of light extraction from the long-lived triplet excitons, which can be exploited to relieve the long-standing efficiency roll-off issue in OLEDs,[51,52] particularly in deep blue-emitting devices. Therefore, the T-S ET process studied here can be employed as a material system design strategy and be readily tailored toward different end applications.

4.4 Experimental Section

4.4.1 Materials

Poly(4-bromostyrene) (PS4Br, M_w ~65,000), isotactic poly(methyl methacrylate) (iPMMA, > 80% isotactic), Nile red (NR), Tris(2-phenylpyridine)iridium (III) ($Ir(ppy)_3$), solvents, reagents used to synthesize the organic phosphor Br6A were all purchased from Millipore Sigma and used without further purification. 0.8 μm Millex-AA sterile syringe filters (mixed cellulose esters membrane, 33 mm) and LUDOX® CL colloidal silica (30 wt% suspension in water) were also purchased from Millipore Sigma. FisherBrand™ disposable cuvettes (10 mm pathlength, PMMA) for dynamic light scattering measurements were purchased from Fisher Scientific.

4.4.2 Synthesis of RTP and fluorescent dye co-encapsulated NPs

The metal-free organic phosphor, Br6A was synthesized according to a published procedure from our lab[41], and its purity was confirmed by ^{1}H NMR. All NPs used in this study were fabricated by a single-step nanoprecipitation method using Milli-Q water as the aqueous outer phase. To prepare Br6A-PS4Br NPs, a stock solution of 1 mg/mL PS4Br mixed with the desired amount of Br6A (wt% to PS4Br) was prepared in tetrahydrofuran (THF) as the organic internal phase. The solution was sonicated to ensure homogenous dissolution. Then 1 mL of this THF mixture solution was slowly injected into the aqueous outer phase under vigorous stirring. It was then further stirred at room temperature overnight to allow for the complete evaporation of organic solvent THF. Purification of Br6A-PS4Br NPs was done by slowly passing them through 0.8 μm Millex-AA sterile syringe filters to remove potential aggregation. The filtered Br6A-PS4Br NPs suspension was then used for further photophysical characterizations. The fluorescent dye co-encapsulated Br6A-NR-PS4Br NPs were synthesized using a similar procedure except when

mixing PS4Br with organic phosphor Br6A, Nile red (stock solution prepared in THF at 1mg/mL) was also added at a corresponding weight ratio (wt% to PS4Br). $Ir(ppy)_3$-containing PS4Br NPs were fabricated using the same procedure and replacing Br6A with $Ir(ppy)_3$. To prepare Br6A-iPMMA and Br6A-NR-iPMMA NPs, similar protocols were followed with the exception that iPMMA was used as the polymer host matrix instead of PS4Br.

4.4.3 Size characterization of RTP and fluorescent dye co-encapsulated NPs

Hydrodynamic size (diameter, nm), and PDI of the lipid-polymer hybrid NPs were measured in Milli-Q water on Malvern Zetasizer Nano ZSP (Model number: ZEN5600) using disposable cuvettes. All measurements were conducted at a backscattering angle of 173° (NIBS default) at 25 °C. Size and polydispersity analyses were performed using Malvern Zetasizer software (Ver. 7.11). The average hydrodynamic diameters of NPs are reported using the peak means of size distribution plots by intensity. All experiments were performed in triplicate from freshly prepared samples (n = 3).

4.4.4 Photophysical characterizations of RTP and fluorescent dye co-encapsulated NPs

Electronic absorption spectra were collected on Varian Cary 50 Bio UV/Vis spectrophoto meter with solution samples in quartz cuvettes (10 mm path length). Steady state emission and excitation spectra, time-resolved emission scan, and lifetime were measured using a Photo Technologies International (PTI) QuantaMaster spectrofluorometer (QM-400) equipped with a Horiba DeltaDiodes Time-Correlated Single Photon Counting (TCSPC) instrument. Lifetime of purely organic phosphor-containing NPs were measured under the phosphorescence mode (Single-Shot Transient Digitizer) using a Xenon flash lamp as the light source. Lifetime values were

obtained by fitting the decay profiles to one-phase or two-phase exponential decay using GraphPad Prism 8. Lifetime of $Ir(ppy)_3$-encapsulated NPs were measured using the TCSPC method. A 360 nm LED head with a maximum pulse repetition rate of 10 MHz was used as the light source. The instrument response function (IRF) was collected using very diluted LUDOX® CL colloidal silica as the scatterer. Lifetime fitting was performed using the FelixGX software. Anoxic aqueous suspensions of NPs were prepared by bubbling argon gas through sample solutions placed in rubber septum-capped quartz cuvettes for 30 min. All experiments were performed in triplicate from freshly prepared samples (n = 3).

4.5 References

1. Augenstein, L.; Nag-Chaudhuri, J. Energy transfer in proteins. *Nature* **1964,** *203* (4950), 1145-1147.

2. Taylor, E. L.; Metcalf, K. J.; Carlotti, B.; Lai, C.-T.; Modica, J. A.; Schatz, G. C.; Mrksich, M.; Goodson, T. Long-range energy transfer in protein megamolecules. *J. Am. Chem. Soc.* **2018,** *140* (46), 15731-15743.

3. Vekshin, N. L. Energy transfer in nucleic acids. In *Photonics of biopolymers*, Vekshin, N. L., Ed. Springer Berlin Heidelberg: Berlin, Heidelberg, 2002; pp 111-121.

4. Zavyalova, E.; Kopylov, A. Energy transfer as a driving force in nucleic acid–protein interactions. *Molecules (Basel, Switzerland)* **2019,** *24* (7), 1443.

5. Liu, X.; Qiu, J. Recent advances in energy transfer in bulk and nanoscale luminescent materials: From spectroscopy to applications. *Chem. Soc. Rev.* **2015,** *44* (23), 8714-46.

6. Fukagawa, H.; Shimizu, T.; Iwasaki, Y.; Yamamoto, T. Operational lifetimes of organic light-emitting diodes dominated by förster resonance energy transfer. *Sci. Rep.* **2017,** *7* (1), 1735.

7. Karunathilaka, B. S. B.; Balijapalli, U.; Senevirathne, C. A. M.; Yoshida, S.; Esaki, Y.; Goushi, K.; Matsushima, T.; Sandanayaka, A. S. D.; Adachi, C. Suppression of external quantum efficiency rolloff in organic light emitting diodes by scavenging triplet excitons. *Nat Commun* **2020,** *11* (1), 4926.

8. Förster, T. Zwischenmolekulare energiewanderung und fluoreszenz. *Annalen der Physik* **1948,** *437* (1-2), 55-75.

9. Förster, T. 10th spiers memorial lecture - transfer mechanisms of electronic excitation. *Discuss. Faraday Soc.* **1959,** (27), 7-17.

10. Förster, T. Transfer mechanisms of electronic excitation energy. *Radiation Research Supplement* **1960,** *2*, 326-339.

11. Kaur, A.; Kaur, P.; Ahuja, S. Förster resonance energy transfer (fret) and applications thereof. *Analytical Methods* **2020,** *12* (46), 5532-5550.

12. Sahoo, H. Förster resonance energy transfer – a spectroscopic nanoruler: Principle and applications. *Journal of Photochemistry and Photobiology C: Photochemistry Reviews* **2011,** *12* (1), 20-30.

13. van der Meer, B. W., van der Meer, D.M. and Vogel, S.S. *Fret - förster resonance energy transfer-from theory to applications*. Wiley-VCH Verlag GmbH & Co. KGaA: 2013.

14. Tanner, P. A.; Zhou, L.; Duan, C.; Wong, K. L. Misconceptions in electronic energy transfer: Bridging the gap between chemistry and physics. *Chem. Soc. Rev.* **2018,** *47* (14), 5234-5265.

15. Zhao, W.; Cheung, T. S.; Jiang, N.; Huang, W.; Lam, J. W. Y.; Zhang, X.; He, Z.; Tang, B. Z. Boosting the efficiency of organic persistent room-temperature phosphorescence by intramolecular triplet-triplet energy transfer. *Nat Commun* **2019,** *10* (1), 1595.

16. Baldo, M. A.; Thompson, M. E.; Forrest, S. R. High-efficiency fluorescent organic light-emitting devices using a phosphorescent sensitizer. *Nature* **2000,** *403* (6771), 750-753.

17. He, G.; Chang, S.-C.; Chen, F.-C.; Li, Y.; Yang, Y. Highly efficient polymer light-emitting devices using a phosphorescent sensitizer. *Appl. Phys. Lett.* **2002,** *81* (8), 1509-1511.

18. Lei, G. T.; Wang, L. D.; Qiu, Y. Blue phosphorescent dye as sensitizer and emitter for white organic light-emitting diodes. *Appl. Phys. Lett.* **2004,** *85* (22), 5403-5405.

19. Ye, T.; Shao, S.; Chen, J.; Chen, Z.; Wang, L.; Ma, D. Detailed studies on energy loss mechanism in phosphor-sensitized fluorescent polymer light-emitting devices. *J. Appl. Phys.* **2010,** *107* (5), 054515.

20. Zhao, J.; Wu, W.; Sun, J.; Guo, S. Triplet photosensitizers: From molecular design to applications. *Chem. Soc. Rev.* **2013,** *42* (12), 5323-51.

21. Lee, K. H.; Lee, J. Y. Phosphor sensitized thermally activated delayed fluorescence organic light-emitting diodes with ideal deep blue device performances. *Journal of Materials Chemistry C* **2019,** *7* (28), 8562-8568.

22. Kuila, S.; George, S. J. Phosphorescence energy transfer: Ambient afterglow fluorescence from water-processable and purely organic dyes via delayed sensitization. *Angew. Chem. Int. Ed.* **2020,** *59* (24), 9393-9397.

23. Jõgela, J.; Uri, A.; Pålsson, L.-O.; Enkvist, E. Almost complete radiationless energy transfer from excited triplet state of a dim phosphor to a covalently linked adjacent fluorescent dye in purely organic tandem luminophores doped into pva matrix. *Journal of Materials Chemistry C* **2019,** *7* (22), 6571-6577.

24. Kirch, A.; Gmelch, M.; Reineke, S. Simultaneous singlet-singlet and triplet-singlet forster resonance energy transfer from a single donor material. *J. Phys. Chem. Lett.* **2019,** *10* (2), 310-315.

25. Shen, F. F.; Chen, Y.; Dai, X.; Zhang, H. Y.; Zhang, B.; Liu, Y.; Liu, Y. Purely organic light-harvesting phosphorescence energy transfer by beta-cyclodextrin pseudorotaxane for mitochondria targeted imaging. *Chem. Sci.* **2020,** *12* (5), 1851-1857.

26. Wigner, E. In *Nachr. Akad. Wiss. Goettingen math. Phys.*, 1927; Vol. K1-2A, p 375.

27. Turro, N. J.; Ramamurthy, V.; Scaiano, J. C. Energy and electron transfer. In *Modern molecular photochemistry of organic molecules*, University Science Books: Sausalito, Calif., 2010.

28. Guo, D.; Knight, T. E.; McCusker, J. K. Angular momentum conservation in dipolar energy transfer. *Science* **2011,** *334* (6063), 1684-7.

29. Cravcenco, A.; Hertzog, M.; Ye, C.; Iqbal, M. N.; Mueller, U.; Eriksson, L.; Borjesson, K. Multiplicity conversion based on intramolecular triplet-to-singlet energy transfer. *Sci. Adv.* **2019,** *5* (9).

30. Zhao, W.; He, Z.; Tang, B. Z. Room-temperature phosphorescence from organic aggregates. *Nat. Rev. Mater.* **2020**.

31. Ma, H.; Lv, A.; Fu, L.; Wang, S.; An, Z.; Shi, H.; Huang, W. Room-temperature phosphorescence in metal-free organic materials. *Annalen der Physik* **2019,** *531* (7), 1800482.

32. Kenry; Chen, C.; Liu, B. Enhancing the performance of pure organic room-temperature phosphorescent luminophores. *Nat. Commun.* **2019,** *10* (1), 2111.

33. Schubert, S.; Delaney, J. T.; Schubert, U. S. Nanoprecipitation and nanoformulation of polymers: From history to powerful possibilities beyond poly(lactic acid). *Soft Matter* **2011,** *7* (5), 1581-1588.

34. Kwon, M. S.; Yu, Y.; Coburn, C.; Phillips, A. W.; Chung, K.; Shanker, A.; Jung, J.; Kim, G.; Pipe, K.; Forrest, S. R.; Youk, J. H.; Gierschner, J.; Kim, J. Suppressing molecular motions for enhanced room-temperature phosphorescence of metal-free organic materials. *Nat. Commun.* **2015,** *6*, 8947.

35. Kwon, M. S.; Lee, D.; Seo, S.; Jung, J.; Kim, J. Tailoring intermolecular interactions for efficient room-temperature phosphorescence from purely organic materials in amorphous polymer matrices. *Angew Chem Int Ed* **2014,** *53* (42), 11177-81.

36. Lee, D.; Bolton, O.; Kim, B. C.; Youk, J. H.; Takayama, S.; Kim, J. Room temperature phosphorescence of metal-free organic materials in amorphous polymer matrices. *J. Am. Chem. Soc.* **2013,** *135* (16), 6325-6329.

37. Siracusa, V. Food packaging permeability behaviour: A report. *Int. J. Polym. Sci.* **2012**, 302029.

38. Miller, K. S.; Krochta, J. M. Oxygen and aroma barrier properties of edible films: A review. *Trends Food Sci. Technol.* **1997,** *8* (7), 228-237.

39. Yu, Y.; Kwon, M. S.; Jung, J.; Zeng, Y.; Kim, M.; Chung, K.; Gierschner, J.; Youk, J. H.; Borisov, S. M.; Kim, J. Room-temperature-phosphorescence-based dissolved oxygen detection by core-shell polymer nanoparticles containing metal-free organic phosphors. *Angew. Chem. Int. Ed.* **2017,** *56* (51), 16207-16211.

40. Jose, J.; Burgess, K. Syntheses and properties of water-soluble nile red derivatives. *The Journal of Organic Chemistry* **2006,** *71* (20), 7835-7839.

41. Bolton, O.; Lee, K.; Kim, H. J.; Lin, K. Y.; Kim, J. Activating efficient phosphorescence from purely organic materials by crystal design. *Nat. Chem.* **2011,** *3* (3), 205-10.

42. Zang, L.; Shao, W.; Kwon, M. S.; Zhang, Z.; Kim, J. Photoresponsive luminescence switching of metal-free organic phosphors doped polymer matrices. *Adv. Optical Mater.* **2020,** *8*, 2000654.

43. Li, J.; Krasavin, A. V.; Webster, L.; Segovia, P.; Zayats, A. V.; Richards, D. Spectral variation of fluorescence lifetime near single metal nanoparticles. *Sci. Rep.* **2016,** *6*, 21349.

44. Gong, Y. Y.; Chen, G.; Peng, Q.; Yuan, W. Z.; Xie, Y. J.; Li, S. H.; Zhang, Y. M.; Tang, B. Z. Achieving persistent room temperature phosphorescence and remarkable mechanochromism from pure organic luminogens. *Adv. Mater.* **2015,** *27* (40), 6195-6201.

45. Marian, C. M. Spin-orbit coupling and intersystem crossing in molecules. *Wiley Interdisciplinary Reviews: Computational Molecular Science* **2012,** *2* (2), 187-203.

46. Hofbeck, T.; Yersin, H. The triplet state of fac-ir(ppy)3. *Inorg. Chem.* **2010,** *49* (20), 9290-9.

47. Yuan, W. Z.; Shen, X. Y.; Zhao, H.; Lam, J. W. Y.; Tang, L.; Lu, P.; Wang, C. L.; Liu, Y.; Wang, Z. M.; Zheng, Q.; Sun, J. Z.; Ma, Y. G.; Tang, B. Z. Crystallization-induced phosphorescence of pure organic luminogens at room temperature. *J Phys Chem C* **2010,** *114* (13), 6090-6099.

48. Jia, W.; Wang, Q.; Shi, H.; An, Z.; Huang, W. Manipulating the ultralong organic phosphorescence of small molecular crystals. *Chemistry (Easton)* **2020,** *26* (20), 4437-4448.

49. Chan, C.-Y.; Tanaka, M.; Lee, Y.-T.; Wong, Y.-W.; Nakanotani, H.; Hatakeyama, T.; Adachi, C. Stable pure-blue hyperfluorescence organic light-emitting diodes with high-efficiency and narrow emission. *Nature Photonics* **2021**.

50. Ansari, R.; Shao, W.; Yoon, S.-J.; Kim, J.; Kieffer, J. Charge transfer as the key parameter affecting the color purity of thermally activated delayed fluorescence emitters. *ACS Appl. Mater. Interfaces* **2021,** *13* (24), 28529-28537.

51. Murawski, C.; Leo, K.; Gather, M. C. Efficiency roll-off in organic light-emitting diodes. *Adv. Mater.* **2013,** *25* (47), 6801-27.

52. Schmidbauer, S.; Hohenleutner, A.; Konig, B. Chemical degradation in organic light-emitting devices: Mechanisms and implications for the design of new materials. *Adv. Mater.* **2013,** *25* (15), 2114-29.

Chapter 5

Efficient High-Temperature Organic Phosphorescence from Metal-Organic Phosphor Frameworks

Zeng, Y.[§]; Ma, J.[§]; Matzger, A. J.; Kim, J. "Efficient High-Temperature Organic Phosphorescence from Metal-Organic Phosphor Frameworks." **2021**, *manuscript in preparation*. ([§]Both authors contributed equally to this work.)

5.1 Introduction

Materials with room temperature phosphorescence (RTP) have demonstrated great potentials in a large variety of advanced applications that can hardly be realized by short-lived fluorescence, such as phosphorescence organic light emitting diodes (OLEDs), optical recording, anti-counterfeiting, chemical sensing, bioimaging, and information encryption and decryption.[1-9] Efficient RTP is conventionally limited to organometallic complexes containing heavy metals to promote spin-orbit-coupling (SOC) and intersystem crossing (ISC) for abundant triplet state generation and to facilitate radiative decay.[10,11] While this strategy allows for bright and efficient phosphorescence, it also presents problems that have greatly limited practical applications of organometallic complexes. These include high cost and potential toxicity of noble/rare-earth metals, instability toward blue phosphorescence, and color fade, *etc.* The long-standing efficiency roll-off issue at high brightness levels in OLEDs,[12,13] particularly in deep blue-emitting devices

due to deteriorating metal-ligand bonds, is detrimental to device operation lifetime and have yet to be resolved.

In the past decade, metal-free purely organic RTP materials[14-17] have been extensively explored as greener and more cost-effective alternatives to organometallic complexes. However, they usually have dark triplet states with weak organic RTP due to slow, spin-forbidden transitions between singlet and triplet states in the absence of heavy atoms and strong SOC. Non-radiative relaxations by molecular vibrations typically deactivate the triplet excitons before the material can phosphoresce. Researchers have developed several strategies to mitigate these challenges, including crystallization,[18-22] embedment in host matrices such as steroids,[23,24] glassy polymers,[16,25-27] and metal-organic frameworks (MOFs),[28] and formation of ionic crystals.[29] However, crystal qualities can significantly affect materials' RTP performance; there are also stringent requirements for selecting a proper host matrix such as solubility, energy levels, rigidity, and optical inertness. Moreover, the guest-host confinement approaches tend to fail rapidly above room temperature since the weak secondary bonding (< 10 kcal/mol) is not sufficient to suppress the non-radiative vibrational loss caused by stronger molecular vibrations at higher temperatures. More importantly, these approaches mostly aimed at suppressing the adversary molecular motions of organic phosphors hence reducing non-radiative decay[30] while leaving the issue of inherent weak SOC in purely organic emitters largely unaddressed. Thus, although these methods have extended phosphorescence lifetime, very few material systems have desirable quantum efficiency for practical photofunctional applications. Therefore, promoting SOC and suppressing molecular motions simultaneously in the material system is the key to achieving high performance organic phosphorescence for applications in optoelectrical devices. Yet this aspect has rarely been thoroughly investigated and remains a demanding task.

One approach to achieve this is to coordinate organic phosphors with metal ions and form metal-organic frameworks (MOFs). MOFs are a class of attractive materials of great importance in both fundamental research and industrial applications, with highly ordered, porous three-dimensional network consisting of isolated organic linker connected by metal clusters.[31-35] We envision that metals act as structure-directing elements in MOFs and be positioned in close proximity (typically < 1 nm) to the coordinated organic phosphor. This potentially facilitates the enhancement of SOC in the organic phosphor via an external heavy atom effect from the metal centers, similar to the external heavy halogen effect found in conjugated organic salt-based phosphorescence materials.[36,37] Additionally, the strong coordination bond (~100 kcal/mol in crystals) and framework rigidity can effectively suppress non-radiative deactivations by restricting molecular motions of the incorporated organic phosphors. Yang et al. have reported a few examples of RTP MOFs by coordinating phthalic acids with Group 12 metals (Zn^{2+} and Cd^{2+}).[38,39] However, the resulted RTP emission typically involves metal-to-ligand or ligand-to-metal charge transfer (MLCT or LMCT) processes,[40] which makes the color tuning challenging since metal ions can modify the electronic structures of the organic phosphors (emitters). It is also unclear whether heavy atom effect from transition metals is involved in this material system by comparing the Zn^{2+}-based MOFs to the Cd^{2+}-based counterparts since the MOF crystal architecture changed simultaneously when the metal ions were changed.

With this in mind, we herein describe a new design strategy to achieve efficient organic RTP and even high-temperature phosphorescence (HTP) by coordinating organic phosphors as ligand linkers to Zr^{4+} and Hf^{4+}metal ions and assembling them into highly ordered and rigid metal-organic phosphor frameworks, isostructural to UiO-67. The organic emitting center is not directly conjugated to the metal clusters to ensure that the phosphorescence emission of the UiO-67-type

MOF material stems from the organic phosphor without the influence of the metal ions. The obtained MOF materials exhibit strong long-lived RTP under ambient conditions and stable HTP that persists at temperatures as high as 400K, whereas the organic phosphor precursor has dark triplet states at room temperature, confirming effective molecular vibration restriction via strong coordination bonding and rigid UiO-67 framework. The heavier UiO-67 (Hf) provides an even stiffer scaffold to withhold the coordinated organic phosphor and hence is more efficient at facilitating phosphorescence emission. Although it is unclear if significant external heavy atom effect from metal clusters is present in our MOF system, the results from our study can aid in the identification of critical design parameters and structural basis for organic phosphorescence of high brightness and desirable stability.

5.2 Results and Discussion

5.2.1 Materials design rationale

It has been previously reported by the Kim lab that G1 embedded in polyvinyl alcohol (PVA) demonstrates greatly enhanced organic RTP.[26] The hydrogen bonding between the rigid polymer matrix PVA and G1 restrict the molecular motion of the organic phosphor and suppressed non-radiative decay. We hypothesized that if stronger rigidifying force such as coordination bonding with metal clusters were applied to fix G1 in a highly ordered framework and isolated from each other, collision-based molecular vibration should be further suppressed even under conditions with high thermal energy, e.g., above room temperature. The close proximity of metal clusters to the organic phosphor within the framework, specifically the triplet exciton generating benzaldehyde group[20] can also potentially exert heavy atom effect through space and enhance SOC. Thus, it is anticipated that strong HTP can be achieved.

Zirconium-based UiO-type MOFs show exceptional chemical and thermal stabilities, and isostructural materials can be synthesized with hafnium.[41-43] Hafnium (atomic number 72) is a significantly heavier metal element than zirconium (atomic number 40), and both are earth-abundant metals. As such, these systems are ideal for probing the external heavy atom effect of metal clusters on organic phosphorescence enhancement. Zirconium-based UiO-67 is a highly porous three-dimensional network formed by connecting $Zr_6O_4(OH)_4$ clusters with 4, 4'-biphenyldicarboxylic acid (BPDC) struts.[42,44] G1 has two carboxylic acid groups on its side chains, and geometry optimized G1 and BPDC show similar carboxylate distances, 10.0 Å and 9.67 Å, respectively, which makes G1 a suitable UiO-67-type MOF ligand linker (Figure 5.1). Importantly, the methylene spacer in G1 structure between the bromobenzaldehyde core and the carboxylate group effectively intercept orbital mixing between the phosphorescence-emitting unit and the metal, hence preventing MLCT or LMCT processes. Additionally, both Zr^{4+} and Hf^{4+} lack d-electrons for possible MLCT process. Therefore, the role of the metal element in the MOF scaffold is different from that in conventional organometallic compounds.

In the first study, we attempted to use G1 in replacement of BPDC to coordinate with Zr^{4+} and form UiO-67-type structure Zr-G1 **(**Figure 5.1a**)**. However, the presence of broad diffraction features at low angles on powder X-ray diffraction (PXRD) spectrum (Figure 5.1b) indicates the lack of long-range order in the synthesized material. This is likely due to the much higher flexibility in G1 structure in comparison to that in BPDC.[45] Given the similarity in their geometries, we used a mixed ligand approach (Figure 5.2) which allows for the incorporation of G1 into UiO-67 forming Zr-G1-BPDC without altering its framework topology.

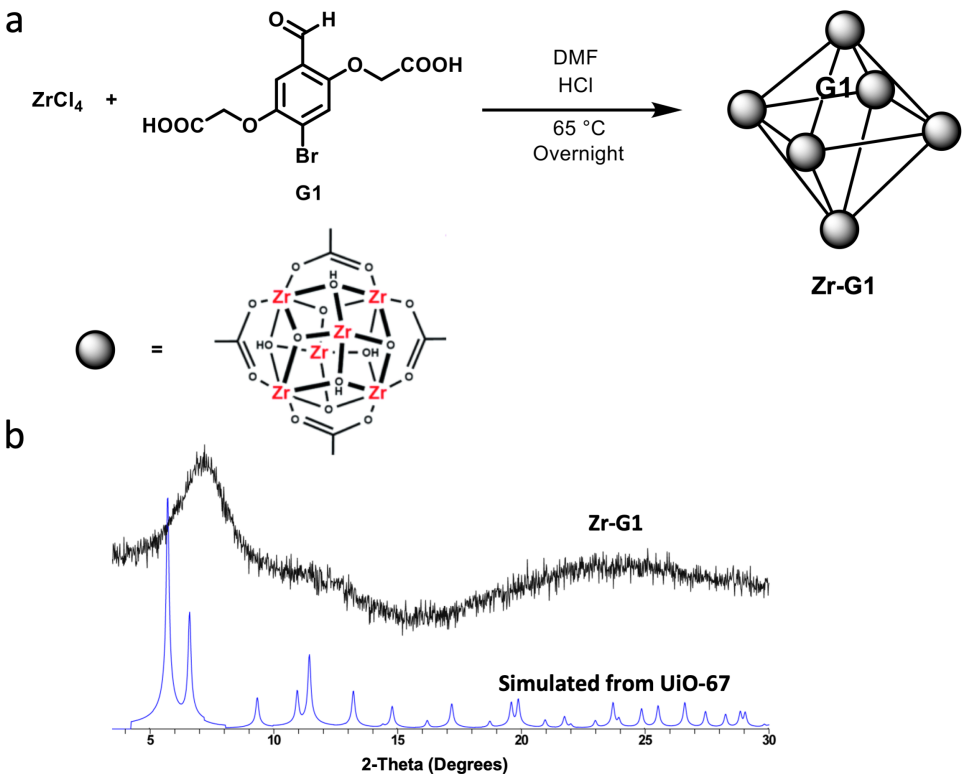

Figure 5.1 | Synthetic scheme and powder X-ray diffraction of Zr-G1 MOF. a, Synthetic procedure of Zr-G1 MOF and structure of Zr_6 metal cluster in UiO-type MOF. **b**, Powder X-ray diffraction of obtained Zr-G1. The presence of broad diffraction features at low angles indicates the lack of long ranger order, likely due to the structural flexibility in G1.

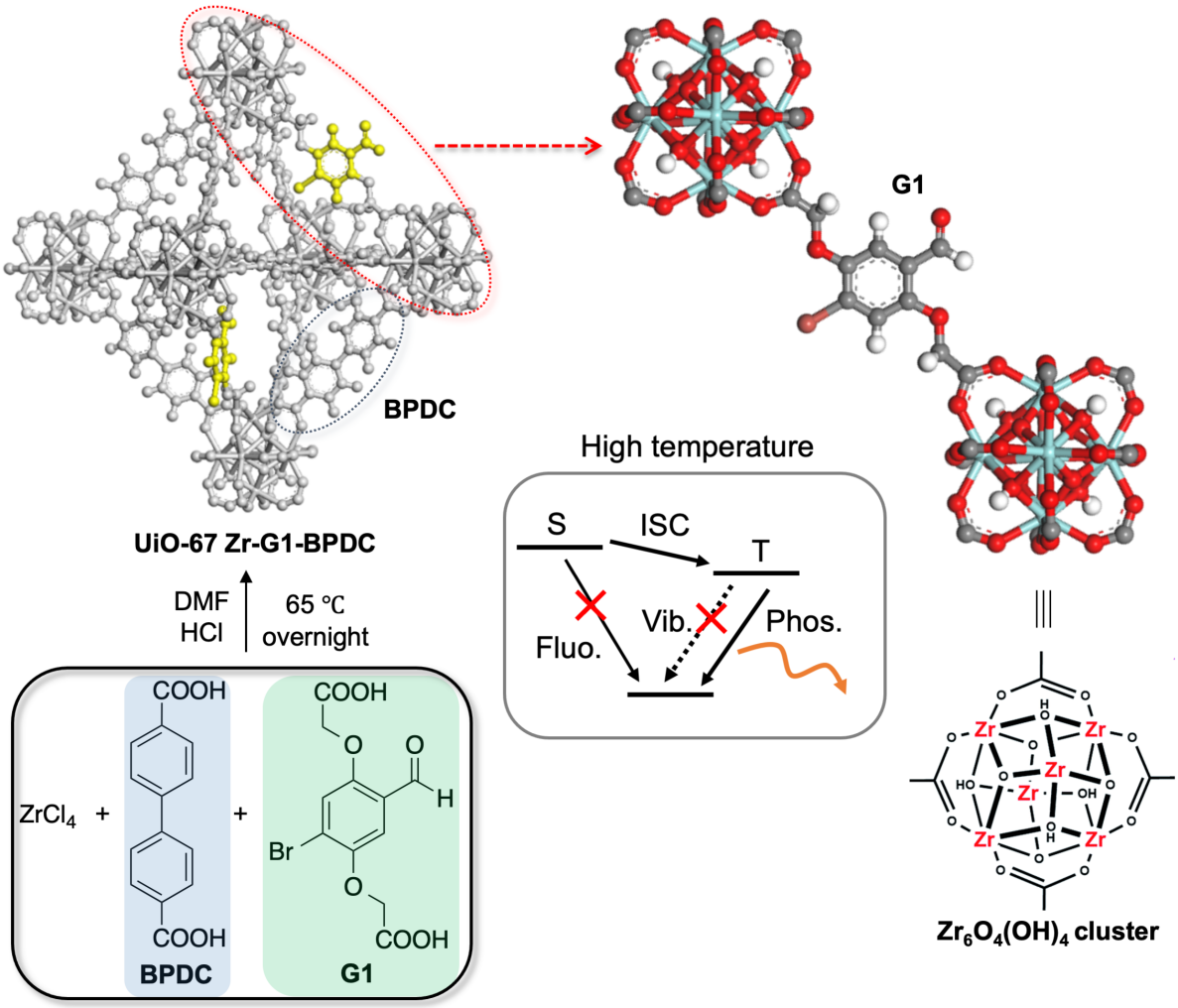

Figure 5.2 | Synthetic scheme and structure of UiO-67 Zr-G1-BPDC. G1 is incorporated into UiO-67 framework through coordination bonding with Zr_6 metal clusters. The simplified Jablonski diagram shows possible photophysical processes of G1 ligand in UiO-67 Zr-G1-BPDC, generating high-temperature organic phosphorescence.

5.2.2 Synthesis and structural characterizations of UiO-67 Zr-G1-BPDC

Zr-G1-BPDC was synthesized via solvothermal processes similar to the methods reported for UiO-67,[46] using a mixture of G1 and BPDC as ligand linkers at a molar ratio of 2:1. The reaction was carried out at a lower temperature (65℃) compared to conditions reported in the literature considering the thermal stability of G1. To prevent G1 from being physically adsorbed or entrapped within the framework, the synthesized materials were thoroughly washed with DMF,

which readily dissolves G1. The resulting material shows high crystallinity as evidenced by its PXRD data (Figure 5.3 a). The PXRD pattern matches well with that of simulated from UiO-67, confirming that the obtained MOF material indeed possesses UiO-type structure. Furthermore, the activated Zr-G1-BPDC sample exhibited high porosity evidenced by its BET surface area similar to the reported values of UiO-67. G1 passively trapped inside framework pores would largely reduce the BET surface area, contradicting our observation here. To determine the amount of G1 incorporated, ^{1}H NMR after acid digestion (concentrated DCl and DMSO-*d6* at 1:1 volume ratio) of the obtained powder reveals a 2:3 molar ratio between G1 and BPDC (Figure 5.3b). Moreover, Fourier-transform infrared spectroscopy (FTIR) data were acquired, and no peaks were observed in the region of 2500 cm^{-1} and 3000 cm^{1} corresponding to –OH in the free carboxylic acid form of G1. Therefore, these results indicate successful incorporation of G1 into UiO-67 framework as a ligand linker through coordination bonding with metal clusters. We next investigated phosphorescence properties of the obtained UiO-67-type MOF to test our previous hypotheses on structure-rigidifying effect and heavy atom effect from the framework.

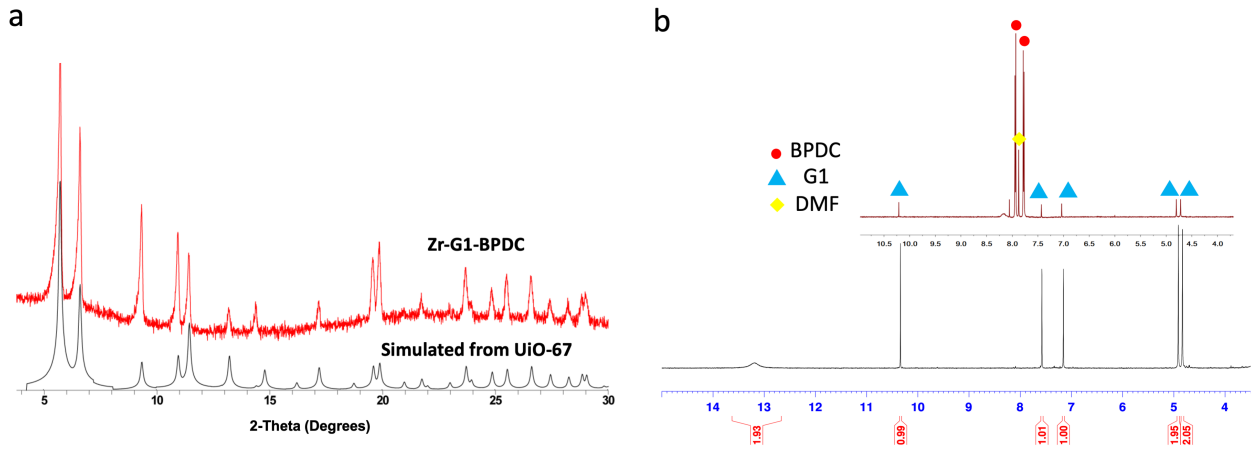

Figure 5.3 | Powder X-ray diffraction and ligand composition analysis of UiO-67 Zr-G1-BPDC. a, Powder X-ray diffraction pattern of synthesized Zr-G1-BPDC compared to that simulated from UiO-67, confirming Zr-G1-BPDC MOF possesses UiO-type structure. **b**, ^{1}H NMR of UiO-67 Zr-G1-BPDC after acid digestion, indicating a 2:3 molar ratio between G1 and BPDC.

5.2.3 Phosphorescence properties of UiO-67 Zr-G1-BPDC under ambient conditions

Under daylight, Zr-G1-BPDC powder exhibits pale yellow color. As expected, under ambient conditions, its gated emission spectrum (500 μs delay, λ_{ex} = 360 nm) shows strong RTP peaked around 610 nm, remarkably brighter than the G1 precursor (Figure 5.4a). This was also evident from on photograph (inset in Figure 5.4a) of the samples under 365 nm illumination where Zr-G1-BPDC displays a bright blueish green color (a mixture of the blue fluorescence of BPDC and the orange phosphorescence of G1) whereas G1 powder alone is hardly emissive. The gated emission spectrum of G1 alone was acquired under vacuum at 250K under which condition the phosphorescence of G1 was detectable. The data shows a similar emission profile compared to that of Zr-G1-BPDC, indicating that the RTP of Zr-G1-BPDC arises from the G1 ligand within the framework without the influence of the co-ligand BPDC or the metal clusters. To further verify this, UiO-67 (Zr-BPDC) was synthesized and studied as a control material. Compared to Zr-G1-BPDC, UiO-67 is not phosphorescent under ambient conditions (Figure 5.4b). Interestingly, the gated excitation spectrum of Zr-G1-BPDC reveals that the 610 nm RTP band is contributed about equally from 360 nm and 420 nm excitation. In the previously published G1-PVA blend film system ,[26] Kwon *et al.* reported an absorption band around 350 nm for G1 in aqueous solution at room temperature. The additional 420 nm gated excitation band we observed for Zr-G1-BPDC is likely attributed to an H-aggregated[47] form of G1 ligand in the MOF scaffold. To test this theory, the gated emission spectrum of Zr-G1-BPDC was collected using 420 nm excitation, which shows a slightly red-shifted emission profile (peaked around 625 nm) compared to 360 nm excitation (Figure 5.4c). This is consistent with characteristics associated with H-aggregation. Lifetime (τ) measurements of Zr-G1-BPDC reveal 911.2 μs and 1085 μs under 360 nm and 420 nm excitation, respectively (Figure 5.4d), indicating the long-lived character of the observed RTP bands. The

slightly longer phosphorescence decay under 420 nm excitation is likely due to intermolecular exciton coupling involved in H-aggregation. These photoluminescence properties of Zr-G1-BPDC confirmed our hypothesis that the strong coordination bonding and rigid MOF scaffold are very effective at suppressing molecular vibrations at room temperature and hence promoting the phosphorescence decay pathway. Notably, the lifetime observed in our MOF system falls slightly under the typical millisecond regime for purely organic phosphors. This could be caused by potential heavy atom effect from Zr_6 clusters in the framework, accelerating the RTP decay. Additionally, given the high porosity of the framework, significant phosphorescence quenching by oxygen is anticipated under ambient conditions, leading to a shorter RTP lifetime.

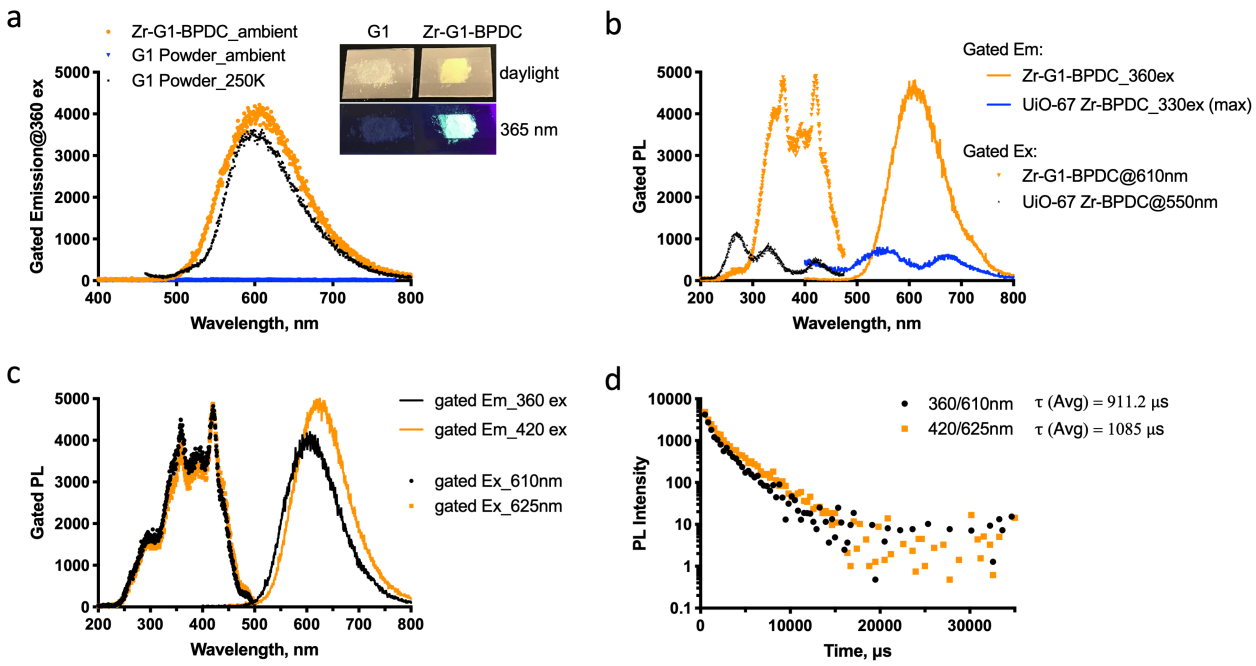

Figure 5.4 | Phosphorescence properties of UiO-67 Zr-G1-BPDC under ambient conditions. **a**, Gated emission spectra of Zr-G1-BPDC (ambient condition, orange line), G1 (ambient condition, blue line), and G1 (250K, high vacuum, black line). λ_{ex} = 360 nm. The inset photograph in **a** shows G1 and Zr-G1-BPDC samples under daylight and 365 nm UV-lamp. **b,** Gated photoluminescence (emission and excitation) of Zr-G1-BPDC compared to UiO-67 Zr-BPDC. Gated emission of Zr-G1-BPDC and UiO-67 Zr-BPDC were acquired with λ_{ex} = 360 nm and 330 nm, respectively. Slit was maximized for UiO-67 Zr-BPDC since the sample's RTP is very weak. **c,** Gated emission spectra of Zr-G1-BPDC collected under 360 nm and 420 nm excitation, respectively. Gated excitation spectra were measured at the corresponding emission band peaks. **d,** Phosphorescence emission decay profiles of Zr-G1-BPDC monitored at 610 nm when λ_{ex} = 360 nm (black dots) and at 625 nm when λ_{ex} = 420 nm (yellow dots). All measurements were collected with 500 µs delay.

5.2.4 Phosphorescence properties of UiO-67 Zr-G1-BPDC at high temperatures

To evaluate the strength of the framework's rigidifying effect without the interference of oxygen quenching and potential oxidation, temperature-dependent (295–375K) phosphorescence properties of Zr-G1-BPDC were studied under high vacuum (< 10^{-4} Torr). Gated emission spectra (500 µs delay, λ_{ex} = 360 nm) demonstrate that the phosphorescence signal persists at temperatures as high as 375K, with gradually decreased intensity at higher temperatures due to stronger molecular vibrations (Figure 5.5a). Consistent gated emission profiles across the entire

temperature range suggests that the MOF material possesses high thermal and optical stability (Figure 5.5b upon 360 nm excitation and Figure 5.5c upon 420 nm excitation). Interestingly, while the 420 nm excitation primarily contributes to both the 610 nm and 625 nm emission bands, the normalized gated excitation spectra show decreased contribution from 360 nm excitation and concurrent increased contribution from 480 nm excitation. We think that the porous framework could potentially collapse under high vacuum at higher temperatures, leading to a different form of aggregated G1 which further shifted the excitation band to the longer wavelength. However, more structural investigations at high temperatures are necessary to elucidate this phenomenon.

As a comparison, a G1-PVA thin film (doped with 1 wt% G1) was prepared according to the reported procedure.[26] The drop-casted thin film exhibits blue fluorescence only when heated up to 375 K, indicating the interaction between G1 and PVA is not sufficient enough to suppress molecular motion once the temperature is raised along with thermal agitation.

Temperature-dependent phosphorescence decay profiles of Zr-G1-BPDC monitored at 610 nm (λ_{ex} = 360 nm) further corroborated the long-lived nature of the orange-colored RTP and HTP emission as well as the rigidity of the framework. Lifetime (τ) values were summarized in Table 5.1, demonstrating shorter lifetimes at higher temperatures where the non-radiative decay is more prominent. Notably, the τ_{avg} of Zr-G1-BPDC at room temperature under vacuum is ~1.3 ms, shorter than the reported value (4.7 ms) of G1 in PVA films.[26] This could be an indicator of the heavy atom effect G1 encountered in the framework which increases phosphorescence decay rate (i.e., shorter lifetime). The phosphorescence quantum efficiency of Zr-G1-BPDC would need to be measured to further verify this. Since the heavy atom effect of Zr_6 clusters would enhance SOC and ISC, more triplet excitons would be generated in the framework compared to that in G1-PVA, resulting in a higher quantum efficiency.

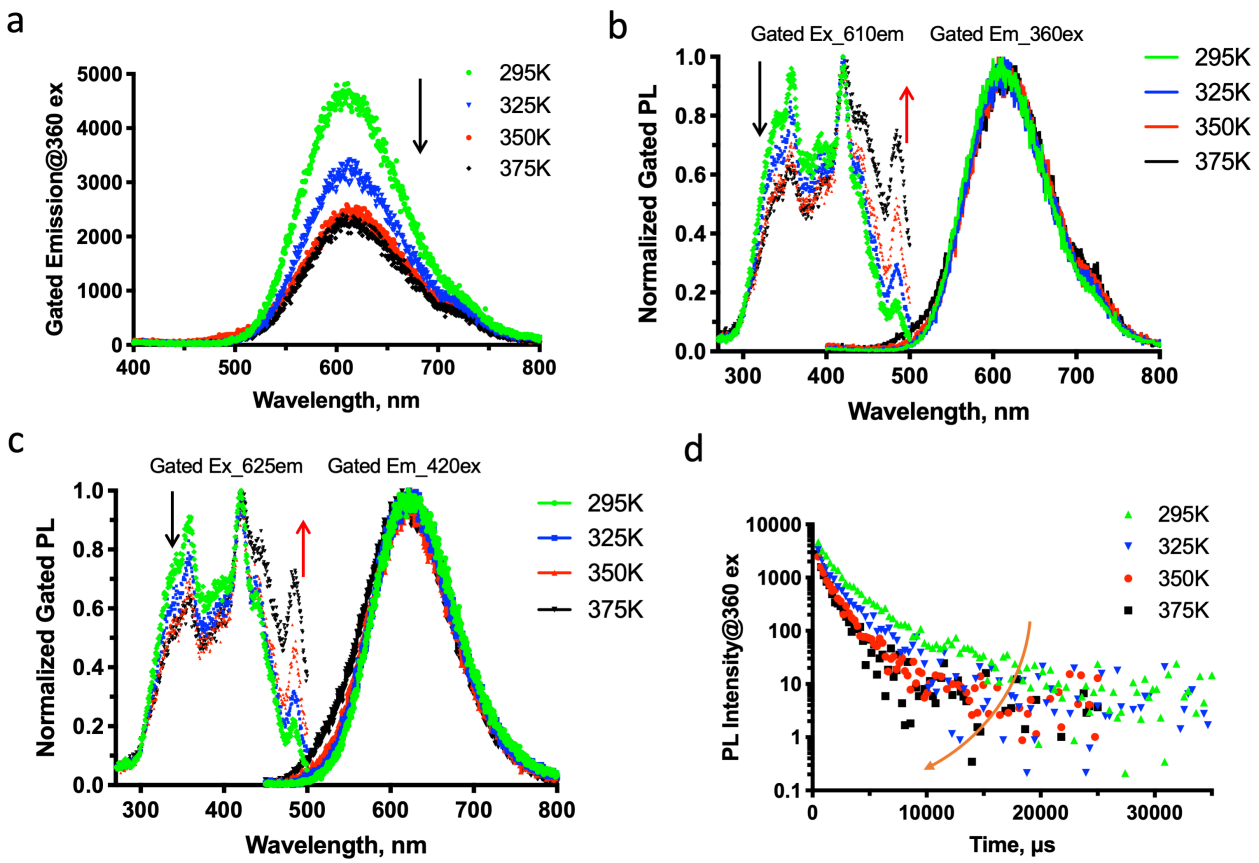

Figure 5.5 | Phosphorescence properties of UiO-67 Zr-G1-BPDC at high temperatures (295–375K). a, Temperature-dependent gated emission spectra of Zr-G1-BPDC. λ_{ex} = 360 nm. **b,c,** Temperature-dependent normalized gated photoluminescence (emission and excitation) of Zr-G1-BPDC under 360 nm (**b**) and 420 nm (**c**) excitation. Gated excitation spectra were measured at the corresponding emission band peaks, 610 nm (**b**) and 625 nm (**c**), respectively. 500 µs delay. **d,** Temperature-dependent phosphorescence emission decay profiles monitored at 610 nm with λ_{ex} = 360 nm. All measurements were collected under high vacuum (< 10^{-4} Torr) with 500 µs delay.

Table 5.1 | Summary of phosphorescence lifetime τ components and average lifetime τ_{avg} in UiO-67 Zr-G1-BPDC at different temperatures (λ_{ex} = 360 nm, λ_{em} = 610 nm)

T (K)	295	325	350	375
τ fast (µs)	722.1	446.3	289.6	205.6
τ slow (µs)	2676	1952	1444	1171
percent fast (%)	69.8	72.8	76.8	86.6
τ_{avg}[a] (µs)	1312	855.9	557.4	335.0

[a]The average lifetime τ_{avg} was calculated according to τ_{avg} = τ fast * percent fast + τ slow * (1-percent fast).

5.2.5 Potential spin-orbit coupling enhancement in UiO-67 Hf-G1-BPDC

To further probe the potential external heavy atom effect mediated by metal clusters in the framework, we extended the strategy incorporating G1 into UiO-67 (Zr) structure to UiO-67 (Hf). As we discussed before, Zr^{4+} and Hf^{4+}-based UiO-type MOFs are known to be isostructural, and given Hf is significantly heavier than Zr, UiO-67 (Hf) was anticipated to impart even more prominent SOC and ISC enhancement as well as phosphorescence decay facilitation. Indeed, the synthesized Hf-G1-BPDC is isostructural to UiO-67 although it is slightly less crystalline based on PXRD data. Composition analysis by ^{1}H NMR reveals a higher G1 incorporation ratio in the framework compared to that in Zr-G1-BPDC, with the same feeding molar ratio of G1:BPDC at 2:1. Since we don't expect to see any optical interference from the co-ligand BPDC, the slightly different G1 incorporation ratio should not affect its RTP or HTP performance in the framework. Indeed, under ambient conditions, similar RTP characteristics were observed in Hf-G1-BPDC (Figure 5.6) compared to those in Zr-G1-BPDC, except that the RTP band is primarily excited by 420 nm instead of 360 nm. This is likely due to a higher percent presence of H-aggregated G1 in the Hf-G1-BPDC framework since more G1 was incorporated. It should be noted that, the average lifetime (τ_{avg}) of Hf-G1-BPDC is longer than that of Zr-G1-BPDC, ~1 ms and ~1.4 ms under 360 nm and 420 nm excitation, respectively (Figure 5.6b). This suggests that the heavier UiO-67 (Hf) framework suppresses molecular vibrations more effectively than its Zr counterpart.

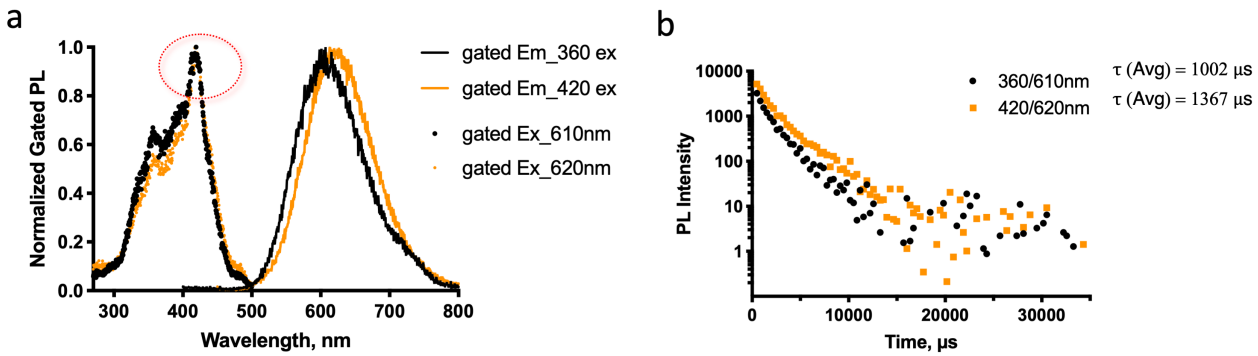

Figure 5.6 | Phosphorescence properties of UiO-67 Hf-G1-BPDC under ambient conditions. **a**, Normalized gated photoluminescence (emission and excitation) spectra of Hf-G1-BPDC under 360 nm (black trace) and 420 nm (orange trace) excitation, respectively. Gated excitation spectra were measured at the corresponding emission band peaks, 610 nm (black dots) and 620 nm (orange dots), respectively. **b,** Phosphorescence emission decay profiles of Hf-G1-BPDC monitored at 610 nm under 360 nm excitation (black dots) and at 620 nm under 420 nm excitation (yellow dots). All measurements were collected with 500 µs delay.

Temperature-dependent gated photoluminescence spectra of Hf-G1-BPDC reveal that the phosphorescence signal persists at even higher temperatures (as high as 400K) compared to Zr-G1-BPDC (Figure 5.7). Similar red shifts in phosphorescence excitation bands from 360 nm to 480 nm were also observed here. Phosphorescence lifetime decay profiles show similar trends to those of Zr-G1-BPDC, except for longer lifetime components at each corresponding temperature point (Table 5.2). These results further confirmed that the heavier UiO-67 (Hf) framework provides more significant ligand rigidifying effect than UiO-67 (Zr), resulting in longer phosphorescence lifetimes of the coordinated organic phosphor ligand G1. However, it is uncertain if the Hf_6 clusters exert additional heavy atom effect on the coordinated G1, compared to the Zr_6 clusters since it is difficult to deconvolute the lifetime-prolonging rigidifying effect and the lifetime-shortening heavy atom effect. One potential solution to this problem is measuring phosphorescence lifetimes of UiO (Zr or Hf) G1-BPDC at 77K where molecular vibration is negligible and hence the difference in framework rigidifying effect is of no significant consideration, allowing us to solely analyze the heavy atom effect. One caveat of this approach is

that the co-ligand BPDC would likely phosphoresce at 77K, interfering with G1 phosphorescence. Alternatively, RTP quantum efficiencies of UiO (Zr or Hf) G1-BPDC can be measured and compared since heavy atom effect is expected to generate more triplet excitons and facilitate more efficient phosphorescence decay.

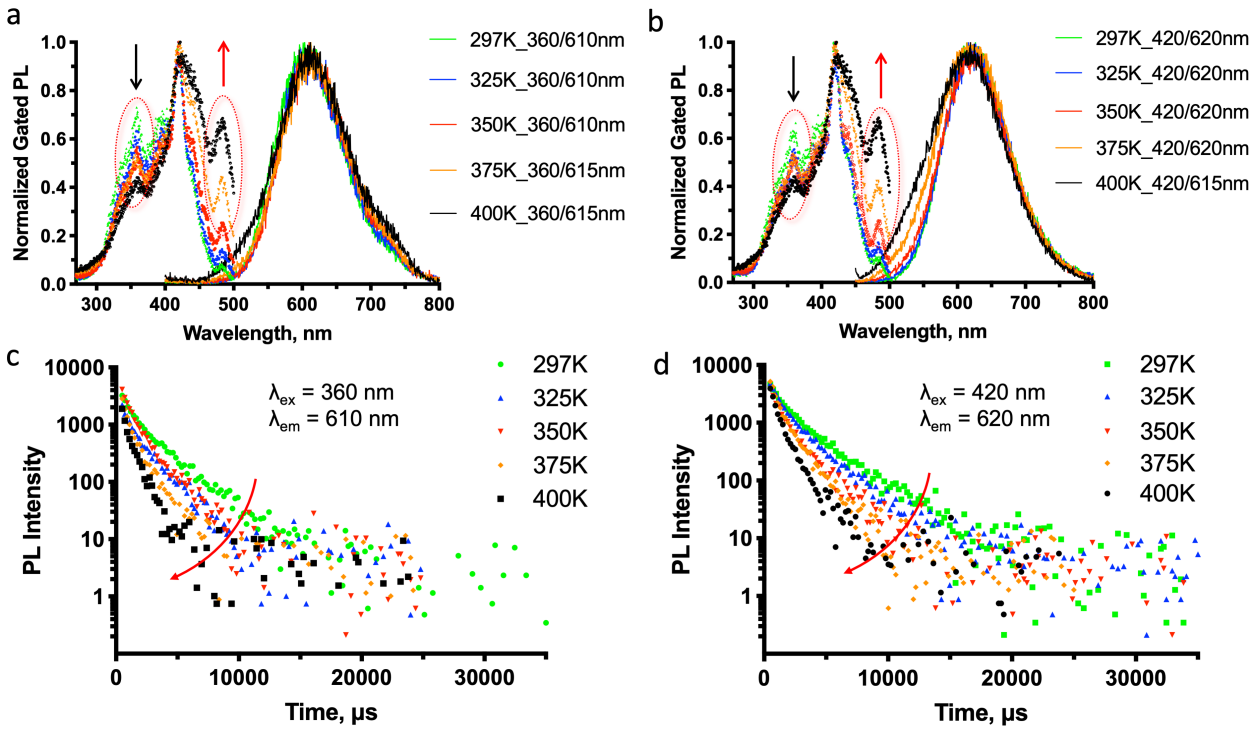

Figure 5.7 | Phosphorescence properties of UiO-67 Hf-G1-BPDC at high temperatures (295–400K). a,b, Temperature-dependent normalized gated emission spectra of Hf-G1-BPDC under 360 nm (**a**) and 420 nm (**b**) excitation. Normalized gated excitation spectra were measured at the corresponding emission band peaks. **c**,**d,** Temperature-dependent phosphorescence emission decay profiles monitored at 610 nm with λ_{ex} = 360 nm (**c**) and at 620 nm with λ_{ex} = 420 nm (**d**). All measurements were collected under high vacuum (< 10^{-4} Torr) with 500 µs delay.

Table 5.2 | Summary of phosphorescence lifetime τ components and average lifetime τ_{avg} in UiO-67 Hf-G1-BPDC at different temperatures

T (K)	297		325		350		375		400	
λ_{ex}[a] (nm)	360	420	360	420	360	420	360	420	360	420
τ fast (μs)	637.5	614.4	524	676.6	450.5	618	328.3	538.1	229.1	447.1
τ slow (μs)	2525	2602	2010	2405	1544	1981	1240	1794	991.5	1380
percent fast (%)	68.1	60.7	72.2	70.4	70.4	73.4	80.7	83.1	85.2	83.4
τ_{avg}[b] (μs)	1240	1396	937.1	1188	774.2	980.6	504.2	750.3	341.9	602.0

[a]Phosphorescence decay profiles were monitored at 610 nm and 620 nm when λ_{ex} of 360 nm and 420 nm were used, respectively.
[b]The average lifetime τ_{avg} was calculated according to τ_{avg} = τ fast * percent fast + τ slow * (1-percent fast).

5.3 Conclusion and Outlook

In this work, we sought to test two hypotheses in the context of metal-organic phosphor framework, (1) the strong coordination bonding between organic phosphor and metal clusters along with the rigid MOF scaffold can substantially suppress molecular vibrations surrounding the coordinated organic phosphor and hence subdue non-radiative deactivation of triplet excitons, and (2) metal clusters in the framework can impart heavy atom effect on the coordinated organic phosphors and promote triplet electron population and phosphorescence decay via enhanced SOC.

By adopting a mixed ligand approach, we successfully coordinated the organic phosphor G1 to Zr_6 and Hf_6 clusters and constructed metal-organic phosphor frameworks isostructural to UiO-67. The obtained MOF materials are highly phosphorescent under ambient conditions whereas the G1 precursor has dark triplet states. We also confirmed that the observed MOF RTP originates from the intrinsic photophysical property of G1 ligand in the framework without the influence of the co-ligand BPDC or the metal clusters. Impressively, both UiO-67 Zr-G1-BPDC

and Hf-G1-BPDC exhibit stable HTP that persists at temperatures as high as 400K, attesting to the strong molecular vibration restriction via coordination bonding and the rigid UiO-67 framework. However, since the heavier Hf_6 clusters also result in a stiffer MOF scaffold, which in turn leads to longer-lived organic RTP and HTP, it is unclear if there is additional heavy atom effect at play by comparing the phosphorescence lifetimes of Zr-G1-BPDC and Hf-G1-BPDC.

Additional structural studies such as thermogravimetric analysis, temperature-dependent PXRD and ligands spatial arrangement will provide more insight into thermostabilities and the interesting red shifts in the excitation bands of the synthesized UiO-67 MOF materials. Further photophysical characterizations such as phosphorescence quantum efficiencies and diffuse reflectance UV-vis absorption will help quantify potential heavy atom effect in the framework and elucidate its nature. While the organic RTP lifetimes of the developed MOFs in this study are close to 1 ms and still too long to be ideal for phosphorescence OLED applications, more structural optimization can be carried out to enhance SOC and shorten the phosphorescence lifetime. For example, from the material architecture perspective, a shorter distance and stronger interaction between the phosphorescence-emitting benzaldehyde group (i.e., the triplet exciton generation center) and the metal cluster is the key to promoting substantial 'direct heavy atom effect'.[20,37]

Nonetheless, the metal-organic phosphor framework concept presented in this work represents a new promising design strategy to restrict molecular vibration and promote SOC simultaneously for generating strong organic phosphorescence. Structural parameters such as metal mass, interaction energy and distance between metal clusters and triplet state generation center, as well as ligand configuration all affect the luminescence characteristics of the MOF material, including quantum yield, phosphorescence lifetime, and color. With the right balance,

the MOF strategy still holds the promise to maximize triplet exciton utilization in purely organic emitters and solve the efficiency roll-off issue in phosphorescence OLEDs.

MOFs are highly robust and modular material platforms in which metal clusters and organic ligand linkers of the same connectivity can be used to tailor materials with a wide variety of luminescent properties for applications in light-emitting devices and sensors. We envision that phosphorescent color tuning could readily be achieved by changing the organic phosphor ligand linker since metal clusters have no influence on the band gaps (electronic structures). Additionally, MOF's high porosity and surface area, together with organic phosphor's sensitivity toward oxygen quenching make metal-organic phosphor frameworks attractive candidates for phototheranostic applications such as photodynamic therapy (PDT).[48] PDT involves the generation of cytotoxic reactive singlet oxygen ($^1O_2$) from ground state triplet oxygen ($^3O_2$), which can be achieved by oxygen quenching of organic RTP. However, the efficacy of PDT is often impeded by tumor hypoxia where oxygen ($^3O_2$) is deficient. This can be overcome by oxygen storage and transport capability of MOFs. Therefore, this could potentially serve as a novel strategy to enhance immunogenic PDT and cancer immunotherapy.

5.4 Experimental Section

5.4.1 Materials

Zirconium tetrachloride ($ZrCl_4$, 98%) were purchased from Acros. Concentrated HCl, acetone and dimethylformamide (DMF) (ACS reagent grade) were all purchased from Fisher Scientific. Biphenyl-4,4'-dicarboxylic acid (BPDC, 98%) were purchased from Alfa Aesar. Polyvinyl alcohol (PVA) and other solvents and reagents used to synthesize the organic phosphor

G1 were all purchased from Millipore Sigma. All chemicals were used as received without further purification.

5.4.2 Synthesis and structural characterization of UiO-67-type MOFs

The metal-free organic phosphor G1 was synthesized according to a published procedure from the Kim lab,[26] and its purity was confirmed by ^{1}H NMR on 500 MHz Varian Inova NMR spectrometer. All UiO-67-type MOFs studied in this chapter were prepared via solvothermal processes according to a modified method reported for UiO-67[46] by my collaborator Jialiu Ma in Professor Adam Matzger's group. UiO-67 Zr-G1-BPDC and Hf-G1-BPDC were synthesized using a mixture of G1 and BPDC as the ligand linkers, at a feeding molar ratio of 2:1. The synthesized materials were thoroughly washed with DMF, which was then exchanged with acetone and activated under vacuum. The obtained MOF powders were stored in a glovebox under a nitrogen atmosphere. Structural characterizations of the synthesized MOFs including ^{1}H NMR, powder X-ray diffraction (PXRD), BET surface area analysis, and FT-IR were also carried out by Jialiu Ma.

5.4.3 Photoluminescence measurements of UiO-67-type MOFs

Photophysical properties including gated (500 μs delay) emission and excitation spectra and lifetime were measured using a Photo Technologies International (PTI) QuantaMaster spectrofluorometer (QM-40). Temperature-dependent photoluminescence profiles under high vacuum were collected using Janis VPF-1000 cryostat equipped with a LakeShore 335 Temperature Controller and a Turbo pump (Agilent Technologies). MOF samples were taped on quartz slides and equilibrated for 30 min after the set temperature point was reached. Lifetime

measurements were collected under the phosphorescence mode using a Xenon flash lamp as the light source. Lifetime values were obtained by fitting the decay profiles to one-phase or two-phase exponential decay using GraphPad Prism 8.

5.5 References

1. Zhao, J.; Wu, W.; Sun, J.; Guo, S. Triplet photosensitizers: From molecular design to applications. *Chem. Soc. Rev.* **2013,** *42* (12), 5323-51.

2. Xiang, H.; Cheng, J.; Ma, X.; Zhou, X.; Chruma, J. J. Near-infrared phosphorescence: Materials and applications. *Chem. Soc. Rev.* **2013,** *42* (14), 6128-85.

3. Baldo, M. A.; Thompson, M. E.; Forrest, S. R. High-efficiency fluorescent organic light-emitting devices using a phosphorescent sensitizer. *Nature* **2000,** *403* (6771), 750-753.

4. He, G.; Chang, S.-C.; Chen, F.-C.; Li, Y.; Yang, Y. Highly efficient polymer light-emitting devices using a phosphorescent sensitizer. *Appl. Phys. Lett.* **2002,** *81* (8), 1509-1511.

5. Lei, G. T.; Wang, L. D.; Qiu, Y. Blue phosphorescent dye as sensitizer and emitter for white organic light-emitting diodes. *Appl. Phys. Lett.* **2004,** *85* (22), 5403-5405.

6. Ye, T.; Shao, S.; Chen, J.; Chen, Z.; Wang, L.; Ma, D. Detailed studies on energy loss mechanism in phosphor-sensitized fluorescent polymer light-emitting devices. *J. Appl. Phys.* **2010,** *107* (5), 054515.

7. Lee, K. H.; Lee, J. Y. Phosphor sensitized thermally activated delayed fluorescence organic light-emitting diodes with ideal deep blue device performances. *Journal of Materials Chemistry C* **2019,** *7* (28), 8562-8568.

8. Wu, S.; Pan, Z.; Chen, R.; Liu, X.; SpringerLink (Online service), Long afterglow phosphorescent materials. Springer International Publishing : Imprint: Springer: Cham, 2017. https://link.springer.com/10.1007/978-3-319-60421-3.

9. Su, Y.; Phua, S. Z. F.; Li, Y.; Zhou, X.; Jana, D.; Liu, G.; Lim, W. Q.; Ong, W. K.; Yang, C.; Zhao, Y. Ultralong room temperature phosphorescence from amorphous organic materials toward confidential information encryption and decryption. *Sci Adv* **2018,** *4* (5), eaas9732.

10. Marian, C. M. Spin-orbit coupling and intersystem crossing in molecules. *Wiley Interdisciplinary Reviews: Computational Molecular Science* **2012,** *2* (2), 187-203.

11. Hofbeck, T.; Yersin, H. The triplet state of fac-ir(ppy)3. *Inorg. Chem.* **2010,** *49* (20), 9290-9.

12. Murawski, C.; Leo, K.; Gather, M. C. Efficiency roll-off in organic light-emitting diodes. *Adv. Mater.* **2013,** *25* (47), 6801-27.

13. Schmidbauer, S.; Hohenleutner, A.; Konig, B. Chemical degradation in organic light-emitting devices: Mechanisms and implications for the design of new materials. *Adv. Mater.* **2013,** *25* (15), 2114-29.

14. Ma, H.; Lv, A.; Fu, L.; Wang, S.; An, Z.; Shi, H.; Huang, W. Room-temperature phosphorescence in metal-free organic materials. *Annalen der Physik* **2019,** *531* (7), 1800482.

15. Zhao, W.; He, Z.; Tang, B. Z. Room-temperature phosphorescence from organic aggregates. *Nat. Rev. Mater.* **2020**.

16. Ma, X.; Wang, J.; Tian, H. Assembling-induced emission: An efficient approach for amorphous metal-free organic emitting materials with room temperature phosphorescence. *Acc. Chem. Res.* **2019,** *52* (3), 738-748.

17. Kenry; Chen, C.; Liu, B. Enhancing the performance of pure organic room-temperature phosphorescent luminophores. *Nat. Commun.* **2019,** *10* (1), 2111.

18. Jia, W.; Wang, Q.; Shi, H.; An, Z.; Huang, W. Manipulating the ultralong organic phosphorescence of small molecular crystals. *Chemistry (Easton)* **2020,** *26* (20), 4437-4448.

19. Wang, X. F.; Xiao, H.; Chen, P. Z.; Yang, Q. Z.; Chen, B.; Tung, C. H.; Chen, Y. Z.; Wu, L. Z. Pure organic room temperature phosphorescence from excited dimers in self-assembled nanoparticles under visible and near-infrared irradiation in water. *J. Am. Chem. Soc.* **2019,** *141* (12), 5045-5050.

20. Bolton, O.; Lee, K.; Kim, H. J.; Lin, K. Y.; Kim, J. Activating efficient phosphorescence from purely organic materials by crystal design. *Nat. Chem.* **2011,** *3* (3), 205-10.

21. Yuan, W. Z.; Shen, X. Y.; Zhao, H.; Lam, J. W. Y.; Tang, L.; Lu, P.; Wang, C. L.; Liu, Y.; Wang, Z. M.; Zheng, Q.; Sun, J. Z.; Ma, Y. G.; Tang, B. Z. Crystallization-induced phosphorescence of pure organic luminogens at room temperature. *J Phys Chem C* **2010,** *114* (13), 6090-6099.

22. An, Z.; Zheng, C.; Tao, Y.; Chen, R.; Shi, H.; Chen, T.; Wang, Z.; Li, H.; Deng, R.; Liu, X.; Huang, W. Stabilizing triplet excited states for ultralong organic phosphorescence. *Nat Mater* **2015,** *14* (7), 685-90.

23. Hirata, S.; Totani, K.; Zhang, J.; Yamashita, T.; Kaji, H.; Marder, S. R.; Watanabe, T.; Adachi, C. Efficient persistent room temperature phosphorescence in organic amorphous materials under ambient conditions. *Adv. Funct. Mater.* **2013,** *23* (27), 3386-3397.

24. Bhattacharjee, I.; Hirata, S. Highly efficient persistent room-temperature phosphorescence from heavy atom-free molecules triggered by hidden long phosphorescent antenna. *Adv. Mater.* **2020**, e2001348.

25. Zhang, Z. Y.; Xu, W. W.; Xu, W. S.; Niu, J.; Sun, X. H.; Liu, Y. A synergistic enhancement strategy for realizing ultralong and efficient room-temperature phosphorescence. *Angew Chem Int Ed Engl* **2020,** *59* (42), 18748-18754.

26. Kwon, M. S.; Lee, D.; Seo, S.; Jung, J.; Kim, J. Tailoring intermolecular interactions for efficient room-temperature phosphorescence from purely organic materials in amorphous polymer matrices. *Angew Chem Int Ed* **2014,** *53* (42), 11177-81.

27. Lee, D.; Bolton, O.; Kim, B. C.; Youk, J. H.; Takayama, S.; Kim, J. Room temperature phosphorescence of metal-free organic materials in amorphous polymer matrices. *J. Am. Chem. Soc.* **2013,** *135* (16), 6325-6329.

28. Mieno, H.; Kabe, R.; Notsuka, N.; Allendorf, M. D.; Adachi, C. Long-lived room-temperature phosphorescence of coronene in zeolitic imidazolate framework zif-8. *Adv. Optical Mater.* **2016,** *4* (7), 1015-1021.

29. Cheng, Z.; Shi, H.; Ma, H.; Bian, L.; Wu, Q.; Gu, L.; Cai, S.; Wang, X.; Xiong, W. W.; An, Z.; Huang, W. Ultralong phosphorescence from organic ionic crystals under ambient conditions. *Angew Chem Int Ed Engl* **2018,** *57* (3), 678-682.

30. Kwon, M. S.; Yu, Y.; Coburn, C.; Phillips, A. W.; Chung, K.; Shanker, A.; Jung, J.; Kim, G.; Pipe, K.; Forrest, S. R.; Youk, J. H.; Gierschner, J.; Kim, J. Suppressing molecular motions for enhanced room-temperature phosphorescence of metal-free organic materials. *Nat. Commun.* **2015,** *6*, 8947.

31. Yuan, S.; Feng, L.; Wang, K.; Pang, J.; Bosch, M.; Lollar, C.; Sun, Y.; Qin, J.; Yang, X.; Zhang, P.; Wang, Q.; Zou, L.; Zhang, Y.; Zhang, L.; Fang, Y.; Li, J.; Zhou, H. C. Stable metal-organic frameworks: Design, synthesis, and applications. *Adv. Mater.* **2018,** *30* (37), e1704303.

32. Cui, Y.; Li, B.; He, H.; Zhou, W.; Chen, B.; Qian, G. Metal-organic frameworks as platforms for functional materials. *Acc. Chem. Res.* **2016,** *49* (3), 483-93.

33. Silva, P.; Vilela, S. M.; Tome, J. P.; Almeida Paz, F. A. Multifunctional metal-organic frameworks: From academia to industrial applications. *Chem. Soc. Rev.* **2015,** *44* (19), 6774-803.

34. Wang, J.; Li, D.; Ye, Y.; Qiu, Y.; Liu, J.; Huang, L.; Liang, B.; Chen, B. A fluorescent metal-organic framework for food real-time visual monitoring. *Adv. Mater.* **2021,** *33* (15), e2008020.

35. Suresh, K.; Matzger, A. J. Enhanced drug delivery by dissolution of amorphous drug encapsulated in a water unstable metal–organic framework (mof). *Angew. Chem. Int. Ed.* **2019,** *58* (47), 16790-16794.

36. Wang, J.; Gu, X.; Ma, H.; Peng, Q.; Huang, X.; Zheng, X.; Sung, S. H. P.; Shan, G.; Lam, J. W. Y.; Shuai, Z.; Tang, B. Z. A facile strategy for realizing room temperature phosphorescence and single molecule white light emission. *Nat. Commun.* **2018,** *9* (1), 2963.

37. Mu, Y.; Wang, J. Q.; Han, S. D.; Pan, J.; Li, J. H.; Wang, G. M. Enhanced room-temperature phosphorescence of an organic ligand in 3d hybrid materials assisted by adjacent halogen atom. *Inorg. Chem.* **2020,** *59* (2), 972-975.

38. Yang, X.; Yan, D. Strongly enhanced long-lived persistent room temperature phosphorescence based on the formation of metal-organic hybrids. *Adv. Optical Mater.* **2016,** *4* (6), 897-905.

39. Yang, X.; Yan, D. Long-afterglow metal-organic frameworks: Reversible guest-induced phosphorescence tunability. *Chem. Sci.* **2016,** *7* (7), 4519-4526.

40. Gong, Q.; Hu, Z.; Deibert, B. J.; Emge, T. J.; Teat, S. J.; Banerjee, D.; Mussman, B.; Rudd, N. D.; Li, J. Solution processable mof yellow phosphor with exceptionally high quantum efficiency. *J. Am. Chem. Soc.* **2014,** *136* (48), 16724-7.

41. Bai, Y.; Dou, Y.; Xie, L. H.; Rutledge, W.; Li, J. R.; Zhou, H. C. Zr-based metal-organic frameworks: Design, synthesis, structure, and applications. *Chem. Soc. Rev.* **2016,** *45* (8), 2327-67.

42. Cavka, J. H.; Jakobsen, S.; Olsbye, U.; Guillou, N.; Lamberti, C.; Bordiga, S.; Lillerud, K. P. A new zirconium inorganic building brick forming metal organic frameworks with exceptional stability. *J. Am. Chem. Soc.* **2008,** *130* (42), 13850-13851.

43. Zhong, G.; Liu, D.; Zhang, J. Incorporation of functional groups expands the applications of uio-67 for adsorption, catalysis and thiols detection. *ChemistrySelect* **2018,** *3* (25), 7066-7080.

44. Øien, S.; Wragg, D.; Reinsch, H.; Svelle, S.; Bordiga, S.; Lamberti, C.; Lillerud, K. P. Detailed structure analysis of atomic positions and defects in zirconium metal–organic frameworks. *Crystal Growth & Design* **2014,** *14* (11), 5370-5372.

45. Bueken, B.; Vermoortele, F.; Cliffe, M. J.; Wharmby, M. T.; Foucher, D.; Wieme, J.; Vanduyfhuys, L.; Martineau, C.; Stock, N.; Taulelle, F.; Van Speybroeck, V.; Goodwin, A. L.; De Vos, D. A breathing zirconium metal-organic framework with reversible loss of crystallinity by correlated nanodomain formation. *Chemistry (Easton)* **2016,** *22* (10), 3264-3267.

46. Katz, M. J.; Brown, Z. J.; Colon, Y. J.; Siu, P. W.; Scheidt, K. A.; Snurr, R. Q.; Hupp, J. T.; Farha, O. K. A facile synthesis of uio-66, uio-67 and their derivatives. *Chem. Commun. (Camb.)* **2013,** *49* (82), 9449-51.

47. Zhao, Y.; Yang, X. G.; Lu, X. M.; Yang, C. D.; Fan, N. N.; Yang, Z. T.; Wang, L. Y.; Ma, L. F. {zn6} cluster based metal-organic framework with enhanced room-temperature phosphorescence and optoelectronic performances. *Inorg. Chem.* **2019,** *58* (9), 6215-6221.

48. Lan, G.; Ni, K.; Xu, Z.; Veroneau, S. S.; Song, Y.; Lin, W. Nanoscale metal-organic framework overcomes hypoxia for photodynamic therapy primed cancer immunotherapy. *J. Am. Chem. Soc.* **2018,** *140* (17), 5670-5673.

Chapter 6

Conclusions and Future Directions

6.1 Thesis Summary

Metal-free purely organic phosphors have unique properties such as long lifetime (milliseconds to seconds) and large Stokes shift (wavelength difference between the absorption and emission peak maxima). These features endow organic phosphorescence-based sensors several advantages over traditional optical sensor design for hypoxia detection and imaging in biological systems. First, purely organic phosphorescence signal from the long-lived triplet excited state is highly susceptible to molecular oxygen quenching through triplet energy transfer, whereas conventional fluorescent probes have short-lived emission (nanoseconds), and thus are typically insensitive to oxygen tension change. This allows them to be applied as ultra-sensitive oxygen sensors. Second, the large Stokes shift effectively eliminates the interference of the excitation light source or the background autofluorescence by wavelength-based deconvolution, enabling high signal-to-noise ratio measurements. Last, unlike conventional inorganic or organometallic-based phosphorescent materials containing precious rare-earth and transition metals with potential toxicity or stability issues in bio-applications, purely organic phosphors are more cost-effective, robust, and biocompatible.

In chapters 2 and 3, a versatile oxygen-sensing platform technology based on lipid-polymer hybrid core-shell organic room-temperature phosphorescence (RTP) nanoparticles (NPs) was developed and applied toward *in vivo* tissue hypoxia imaging and *in vitro* phosphorimetric

biodetection. The organic RTP NPs were synthesized via a facile one-step nanoprecipitation process and consist of (1) a rigid and oxygen-permeable polymer core for the effective activation of bright RTP from the embedded organic phosphor in hypoxic environments, and (2) an amphiphilic phospholipid shell, allowing for excellent water dispersity, biocompatibility, and colloidal stability. The fabricated lipid-polymer hybrid NPs exhibit long-lived bright RTP with milliseconds decay time, high sensitivity toward oxygen quenching, and desirable colloidal and optical stability, which enables them to be exploited as "turn-on" nanosensors under oxygen-deficient conditions.

Chapter 2 reports that these organic RTP NPs effectively visualize chorioretinal tissue hypoxia in clinically relevant living animal models in real-time and with high signal-to-noise ratio. Ischemia-induced hypoxia is a common complication associated with numerous retinopathies and is the most important pathogenic and prognostic factor in retinal vein occlusions (RVO). RVO is the 2nd most common retinal vascular disorder and represents a major cause of vision loss, affecting more than 16 million people worldwide. Early detection and long-term visualization of retinal tissue hypoxia is essential to understand the pathophysiology and treatment of ischemic retinopathies. Currently available techniques to evaluate retinal tissue hypoxia, such as oxygen-sensitive microelectrodes and MRI, have limitations including tissue destruction and insufficient resolution. This necessitates a critical clinical need for a new effective and non-destructive method to measure oxygen tension in the retinal tissue microenvironment. We demonstrated that organic RTP NPs can be a solution to this problem and allow for targeted biocompatible detection of chorioretinal tissue hypoxia. When tested as a hypoxia imaging probe *in vivo* using rabbit RVO and choroidal vascular occlusion models via intravitreal and intravenous injection respectively, RTP NPs' phosphorescence signal is exclusively turned on where tissue hypoxia is present with a

signal-to-noise ratio of 12.5, and persists for at least 7 days. This RTP NP platform is also compatible with multimodal imaging. No ocular or systemic complications were observed with either administration route. Future studies including *in vitro* oxygen sensitivity calibration, *in vivo* oxygen tension determination, as well as pharmacokinetics and biodistributions of the developed organic RTP NPs will be conducted to fully assess their clinical translatability. This work lays a solid foundation demonstrating that this organic RTP nanosensor has a great potential to serve as a general tissue hypoxia tracking probe via minimally invasive systemic delivery. This has both scientific and translational impact at many levels and will enable improved understanding of the pathophysiology, and early diagnosis and prognosis research of diseases involving ischemia-induced hypoxia, beyond the retina and choroid.

Chapter 3 describes the integration of organic RTP-based biosensor with a sandwich-DNA hybridization assay on 96-well plates for highly sensitive and quantitative detection of cell-free nucleic acids. The signal transduction design involves combining oxygen-sensitive RTP nanoparticles with a signal-amplifying enzymatic oxygen scavenging reaction. Glucose oxidase enzyme (GOx) is a well-known oxygen scavenger that efficiently consumes dissolved oxygen (DO) in the process of oxidizing glucose to gluconic acid. Our unique methodology for the phosphorimetric biodetection consists of the following three steps: (1) the targeted bioanalyte binds to the probe and bioreceptor through specific interaction such as nucleic acid hybridization; (2) the bound bioreceptor will then be labeled with GOx through another specific binding event such as avidin-biotin interaction; and finally (3) a solution containing glucose and oxygen-sensitive RTP nanoparticles will be introduced to the target-bioreceptor-GOx complex. As the GOx scavenges the DO in the surrounding environment, the signal transducing organic RTP NPs emit the “turn-on” phosphorescence signal, and the intensity correlates to the concentration of

target bioanalytes. As a proof of concept, a cell-free TP53 gene fragment was tested as the target DNA analyte. Our phosphorimetric assay demonstrates sequence-specific detection with sub-picomolar (0.5 pM) sensitivity. Importantly, this assay is compatible with detecting cell-free nucleic acids in human urine samples without extensive pre-treatment and the green phosphorescence readout can be captured by a smartphone camera. Simply by re-programming the detection probe, our methodology can be adapted to a broad range of biosensor applications for biomarkers of great clinical importance but difficult to detect due to their low abundance *in vivo*. The detection limit of this phosphorimetric assay could be further improved (i.e., lowered) by increasing the amount of organic phosphor embedded in the RTP NPs. Alternatively, it could be achieved by choosing a polymer matrix or polymer blends with relatively lower oxygen permeability to encapsulate organic phosphor. Future work could also include extending the 96-well plate-based detection platform to more portable substrates, such as papers and capillary tubes, leading to the development of affordable point-of-care diagnostics. Therefore, this technology has significant implications for resolving the important practical limitations to the deployment of cancer theragnostic in resource-limited setting.

Next, chapters 4 and 5 shift the focus from exploiting oxygen-sensitive triplet excitons for biosensing and bioimaging applications to investigating fundamental photophysical transitions of triplet excitons in the context of photoluminescence. Chapter 4 details an efficient intermolecular triplet-to-singlet energy transfer (T-S ET) process in purely organic luminescent materials through a pseudo-Förster resonance energy transfer (pseudo-FRET) mechanism, challenging the scientific community to rethink the notion of spin angular momentum conservation observed in conventional energy transfer pathways. An organic phosphor donor with long-lived strong RTP and an organic fluorescent acceptor were co-assembled in rigid polymeric nanoparticles, which was then used as

a model system to study the intermolecular energy transfer using various spectroscopic methods. The T-S ET process quenches the RTP emission from the excited donor triplet state and sensitizes the excited singlet state of the acceptor, which ultimately induces ambient delayed fluorescence (DF). The energy transfer efficiency was measured to reach as high as 75.5% and can be further tuned by the encapsulation ratio of donor and acceptor in NPs. We also found that donor's $T_1 \rightarrow S_0$ spin-orbit coupling (SOC) strength influences the rate of T-S ET (k_{ET}) and in turn the lifetime of the induced ambient DF, with stronger SOC leading to faster k_{ET} and shorter DF lifetime. Further studies such as a systematic investigation of T-S ET efficiency and rate over a range of well-defined donor-acceptor distances would allow us to benchmark the pseudo-FRET mechanism we discovered here against the classic Förster model. The results of this work have multiple implications on material design strategies for manipulating the fate of triplet excitons for photo generation in purely organic molecules. For instance, achieving organic long-lived emission and high quantum efficiency simultaneously through rational molecular design is still a challenging task, especially toward the red and NIR region. The T-S ET concept can be utilized to produce bright afterglow red or NIR fluorescence by pairing an organic phosphor with a long RTP lifetime as the donor with a highly fluorescent red or NIR dye as the acceptor. DF with narrow emission can be realized when the chosen acceptor fluorophore has a sharp emission profile. This serves as an attractive alternative to thermally activated delayed fluorescence (TADF) which is difficult to engineer on a molecular level and often has color purity issues. Lastly, the light extraction rate from triplet excitons is accelerated through the T-S ET process. Therefore, this concept can be exploited in electroluminescence to mitigate against the long-standing efficiency roll-off issue in phosphorescence organic light-emitting devices (OLEDs).

Two key challenges in the field of developing efficient organic RTP materials are (1) weak SOC and intersystem crossing (ISC) in the absence of heavy atom effect, and (2) energy loss to non-radiative molecular vibrations. Chapter 5 aims to address these issues simultaneously in a single material system—metal-organic framework (MOF). Through a mixed ligand approach, organic phosphors were successfully coordinated to zirconium (Zr)- and hafnium (Hf)-based metal clusters as ligand linkers, and MOF materials isostructural to UiO-67 were synthesized. Two hypotheses were tested using this model system: (1) the strong coordination bonding between organic phosphor and metal clusters along with the rigid MOF matrix can substantially suppress molecular vibrations surrounding the organic phosphor and hence subdue non-radiative deactivation of triplet excitons, and (2) metal clusters in the framework can exert external heavy atom effect on the coordinated organic phosphors and promote triplet electron population as well as phosphorescence decay via enhanced SOC. Strong RTP was observed for these MOF materials in comparison to the dark pristine organic phosphor ligand. The origin of the MOF RTP was confirmed to be the coordinated organic phosphor rather than the co-ligand or framework itself. This differentiates our MOF design from that of conventional organometallic compounds where metal elements are part of the emitting centers. Notably, stable high-temperature phosphorescence (HTP) that persists up to 400K was achieved, which was previously considered extremely difficult to attain due to the markedly increased molecular vibrations at elevated temperatures. This result attests to the strong rigidifying effect from the coordination bonding and the MOF matrix, which confirms our hypothesis (1). We also demonstrated that the heavier UiO-67 (Hf) framework is stiffer than the Zr counterpart, and hence is more effective at suppressing non-radiative decay and promoting phosphorescence emission, leading to longer-lived RTP and HTP. However, it was unclear yet if Hf imparts additional heavy atom effect than Zr. Future structural and photophysical

studies were suggested in Chapter 5 to elucidate hypothesis (2). Nevertheless, this work identified critical material design parameters and structural basis for organic phosphorescence of high brightness and desirable stability, opening a new design avenue to achieve efficient organic RTP and HTP toward practical photofunctional applications.

In summary, this dissertation covers both the fundamental and applied aspects of triplet excitons in purely organic RTP molecules (Figure 6.1). Novel material systems and platform technologies were developed to meet challenges in both biomedical and optoelectronic fields. The first section (Chapter 2 and 3) leverages triplet energy quenching by molecular oxygen and, in combination with nanoformulation, expanded the applications of organic RTP materials to addressing clinical problems of great importance yet lacking practical solutions. The second (Chapter 4) and third (Chapter 5) sections shed more light on the fundamental characteristics of triplet excitons and their interactions with electronic states of different spin multiplicity, and generated rational material design strategies to modulate triplet states and harvest energy more efficiently. Overall, this thesis work contributes to advancing the fundamental understanding of triplet exciton behaviors and the technological innovation in their utilizations in sensing, imaging, phototheranostics, and solid-state lighting.

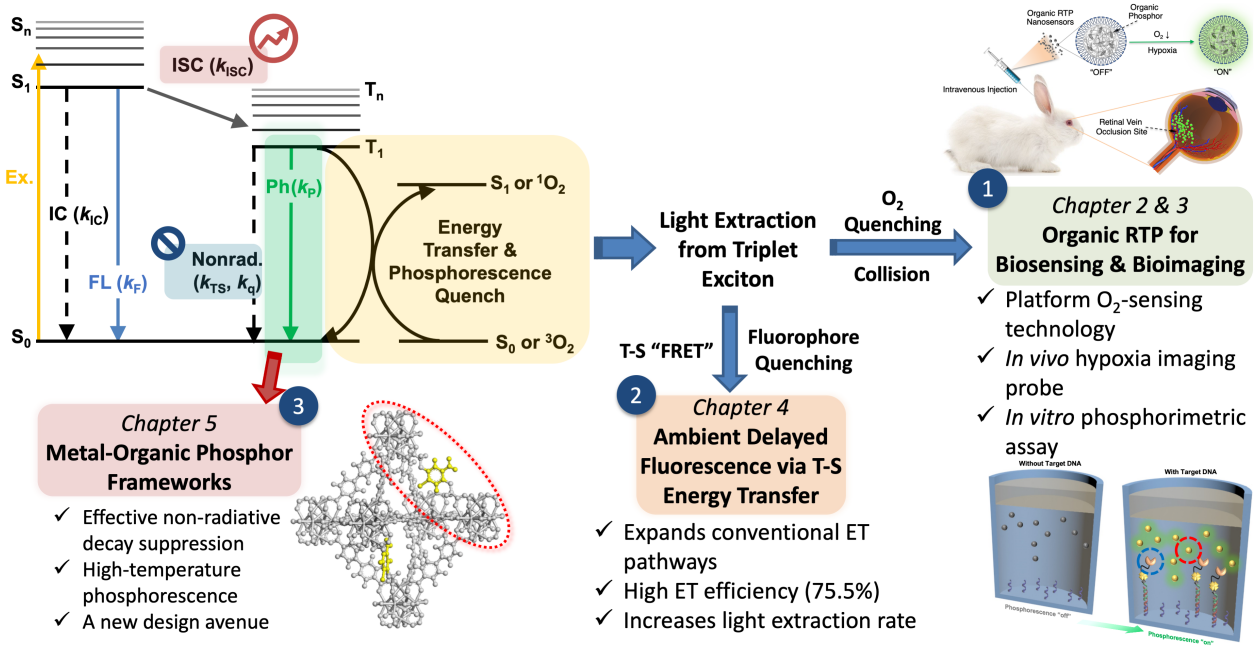

Figure 6.1 | Thesis summary. Triplet exciton modulations in organic room-temperature phosphorescence materials for applications in biosensors and optoelectronics.

6.2 Outlook of Organic Phosphorescence Field

The field of organic RTP materials has witnessed explosive growth over the past decade since the pioneering work from the Kim group[1] and the Tang group.[2] On the application front, three dimensions of organic phosphorescence—long lifetime, sensitive to molecular motion deactivation, and susceptible to oxygen quenching—have been extensively exploited for challenging photofunctions including afterglow bioimaging, hypoxia imaging, chemical sensing, and data encoding. Oxygen and thermal energy are ubiquitous and play crucial roles across the living and non-living systems. Precise and real-time measurement of their intensity and flux can be difficult yet critical. Organic RTP materials can potentially offer attractive and facile solutions to these problems. By integrating principles from adjacent disciplines such as life science, biomedical engineering, mechanical engineering, and electrical engineering, more meaningful and promising practical applications are coming to light every day.

The fourth exciting and emerging dimension of manipulating organic phosphorescence lies in circular polarization. As the next-generation light source, circularly polarized luminescence (CPL)[3-6] demonstrates great potentials in advanced technologies such as CP-OLEDs,[7,8] chiroptical sensing and patterning,[9-12] holography,[13] stem cell differentiation,[14] as well light detection and ranging (LIDAR) in autonomous vehicles.[15] The development of circularly polarized phosphorescence (CPP)[16-19] that couples the unique characteristic features of organic RTP and dissymmetry (chirality) from circular polarization could further enhance CPL performance in aforementioned technologies and beyond. Achieving organic CPP with high quantum efficiency and high dissymmetry factor is no easy feat, however, design strategies in circularly polarized fluorescence might be a good source of inspiration.[20,21]

On the theme of fundamental understanding and developing new organic RTP materials, however, by and large, the focus has been too centered than desirable on suppressing the adversary molecular motions to minimize nonradiative decay. The other equally important and perhaps more challenging factors in organic phosphorescence generation are the ISC of $S_1 \rightarrow T_n$ and SOC of the subsequent $T_1 \rightarrow S_0$. These areas of the field have been relatively less investigated, and lack a deep quantitative mechanistic understanding, which presents a major hurdle in developing efficient organic RTP molecules. Strong ISC of $S_1 \rightarrow T_n$ is a prerequisite for organic materials with high phosphorescence quantum efficiency in photoluminescence because it determines the population of available triplet excitons after photoexcitation. However, this alone does not guarantee material brightness. Strong SOC for $T_1 \rightarrow S_0$ is also required for phosphorescence decay to compete with kinetically favored non-radiative deactivation or triplet-triplet annihilation. This aspect is particularly important in phosphorescence OLEDs. By contrast, in materials where a long phosphorescence lifetime is desired, SOC for $T_1 \rightarrow S_0$ would then need to be tuned downed.

Moreover, although SOC is the dominant mechanism to facilitate ISC, there are other channels such as hyperfine coupling,[22,23] vibronic coupling,[24,25] and aggregation induced ISC.[26] Strong ISC for $S_1 \rightarrow T_n$ does not warrant strong SOC for $T_1 \rightarrow S_0$. Therefore, rational design of organic RTP materials with tailored applications calls for complicated multifaceted considerations yet the chemical structure-electronic structure-phosphorescence property relationships remain moderately elusive. Often, distinctive phosphorescence properties were discovered by chance than by choice. The organic phosphorescence field is in critical need of a comprehensive set of molecular design principles or material engineering approaches for modulating ISC and SOC strength and ultimately the fate of triplet excitons, which can only be collected through systematic investigation of fundamental photophysical processes in candidate organic RTP materials. This process can be labor-intensive and involves extensive trial and error. To accelerate it, integration of computational modeling such as time-dependent density functional theory[27] and Dalton[28] that calculate molecular electronic structures and SOC strength (SOC matrix element) into the workflow with experiments is recommended. The computational work predicts photophysical properties of lead organic phosphors and informs experimentalists the connection between chemical structures and phosphorescence performance. It is important to note that this bottom-up approach does carry risks and computational data can fail to explain experimental results. There is certainly room for continuous improvement regarding the accuracy and efficiency of simulation using quantum chemistry programs, particularly for aggregated or multi-component material systems. In parallel, a relatively more top-down strategy that engages deep learning technologies to identify molecular or system features (structural motifs) that are associated with specific performance characteristics could also assist in developing organic RTP materials through rational design. While this method might be especially useful for large material systems with hierarchical structures and long-range

orders, it would rely on a considerable amount of digitized experimental data of developed organic RTP materials to train the artificial neural networks. Building an up-to-date central organic RTP materials data bank accessible to the entire scientific community would be desirable. In a nutshell, progresses made in computational and experimental work will fuel the growth of each other and collectively the advancement in the field of designer organic RTP materials.

6.3 References

1. Bolton, O.; Lee, K.; Kim, H. J.; Lin, K. Y.; Kim, J. Activating efficient phosphorescence from purely organic materials by crystal design. *Nat. Chem.* **2011,** *3* (3), 205-10.

2. Yuan, W. Z.; Shen, X. Y.; Zhao, H.; Lam, J. W. Y.; Tang, L.; Lu, P.; Wang, C. L.; Liu, Y.; Wang, Z. M.; Zheng, Q.; Sun, J. Z.; Ma, Y. G.; Tang, B. Z. Crystallization-induced phosphorescence of pure organic luminogens at room temperature. *J Phys Chem C* **2010,** *114* (13), 6090-6099.

3. Hu, M.; Feng, H.-T.; Yuan, Y.-X.; Zheng, Y.-S.; Tang, B. Z. Chiral aiegens – chiral recognition, cpl materials and other chiral applications. *Coord. Chem. Rev.* **2020,** *416*, 213329.

4. Sang, Y.; Han, J.; Zhao, T.; Duan, P.; Liu, M. Circularly polarized luminescence in nanoassemblies: Generation, amplification, and application. *Adv. Mater.* **2019**, e1900110.

5. Sanchez-Carnerero, E. M.; Agarrabeitia, A. R.; Moreno, F.; Maroto, B. L.; Muller, G.; Ortiz, M. J.; de la Moya, S. Circularly polarized luminescence from simple organic molecules. *Chem. Eur. J.* **2015,** *21* (39), 13488-13500.

6. Brandt, J. R.; Salerno, F.; Fuchter, M. J. The added value of small-molecule chirality in technological applications. *Nature Reviews Chemistry* **2017,** *1* (6).

7. Kim, Y.-H.; Zhai, Y.; Lu, H.; Pan, X.; Xiao, C.; Gaulding, E. A.; Harvey, S. P.; Berry, J. J.; Vardeny, Z. V.; Luther, J. M.; Beard, M. C. Chiral-induced spin selectivity enables a room-temperature spin light-emitting diode. *Science* **2021,** *371* (6534), 1129.

8. Brandt, J. R.; Wang, X.; Yang, Y.; Campbell, A. J.; Fuchter, M. J. Circularly polarized phosphorescent electroluminescence with a high dissymmetry factor from pholeds based on a platinahelicene. *J. Am. Chem. Soc.* **2016,** *138* (31), 9743-6.

9. Zheng, H.; Ju, B.; Wang, X.; Wang, W.; Li, M.; Tang, Z.; Zhang, S. X.-A.; Xu, Y. Circularly polarized luminescent carbon dot nanomaterials of helical superstructures for circularly polarized light detection. *Adv. Optical Mater.* **2018,** *6* (23), 1801246.

10. Maeda, H.; Bando, Y.; Shimomura, K.; Yamada, I.; Naito, M.; Nobusawa, K.; Tsumatori, H.; Kawai, T. Chemical-stimuli-controllable circularly polarized luminescence from anion-responsive pi-conjugated molecules. *J. Am. Chem. Soc.* **2011,** *133* (24), 9266-9.

11. He, C.; Feng, Z.; Shan, S.; Wang, M.; Chen, X.; Zou, G. Highly enantioselective photo-polymerization enhanced by chiral nanoparticles and in situ photopatterning of chirality. *Nat Commun* **2020,** *11* (1), 1188.

12. Sethy, R.; Kumar, J.; Metivier, R.; Louis, M.; Nakatani, K.; Mecheri, N. M. T.; Subhakumari, A.; Thomas, K. G.; Kawai, T.; Nakashima, T. Enantioselective light harvesting with perylenediimide guests on self-assembled chiral naphthalenediimide nanofibers. *Angew Chem Int Ed Engl* **2017,** *56* (47), 15053-15057.

13. Kobashi, J.; Yoshida, H.; Ozaki, M. Circularly-polarized, semitransparent and double-sided holograms based on helical photonic structures. *Sci. Rep.* **2017,** *7* (1), 16470.

14. Qu, A.; Sun, M.; Kim, J. Y.; Xu, L.; Hao, C.; Ma, W.; Wu, X.; Liu, X.; Kuang, H.; Kotov, N. A.; Xu, C. Stimulation of neural stem cell differentiation by circularly polarized light transduced by chiral nanoassemblies. *Nat Biomed Eng* **2020**.

15. van der Laan, J. D.; Wright, J. B.; Kemme, S. A.; Scrymgeour, D. A. Superior signal persistence of circularly polarized light in polydisperse, real-world fog environments. *Appl. Opt.* **2018,** *57* (19), 5464-5473.

16. Chen, W.; Tian, Z.; Li, Y.; Jiang, Y.; Liu, M.; Duan, P. Long-persistent circularly polarized phosphorescence from chiral organic ionic crystals. *Chemistry (Easton)* **2018,** *24* (66), 17444-17448.

17. Xu, M.; Wu, X.; Yang, Y.; Ma, C.; Li, W.; Yu, H.; Chen, Z.; Li, J.; Zhang, K.; Liu, S. Designing hybrid chiral photonic films with circularly polarized room-temperature phosphorescence. *ACS Nano* **2020,** *14* (9), 11130-11139.

18. Li, H.; Li, H.; Wang, W.; Tao, Y.; Wang, S.; Yang, Q.; Jiang, Y.; Zheng, C.; Huang, W.; Chen, R. Stimuli-responsive circularly polarized organic ultralong room temperature phosphorescence. *Angew Chem Int Ed Engl* **2020,** *59* (12), 4756-4762.

19. Hirata, S.; Vacha, M. Circularly polarized persistent room-temperature phosphorescence from metal-free chiral aromatics in air. *J. Phys. Chem. Lett.* **2016,** *7* (8), 1539-45.

20. Kumar, J.; Nakashima, T.; Kawai, T. Circularly polarized luminescence in chiral molecules and supramolecular assemblies. *J. Phys. Chem. Lett.* **2015,** *6* (17), 3445-52.

21. Goto, T.; Okazaki, Y.; Ueki, M.; Kuwahara, Y.; Takafuji, M.; Oda, R.; Ihara, H. Induction of strong and tunable circularly polarized luminescence of nonchiral, nonmetal, low-molecular-weight fluorophores using chiral nanotemplates. *Angew Chem Int Ed Engl* **2017,** *56* (11), 2989-2993.

22. Buck, J. T.; Boudreau, A. M.; DeCarmine, A.; Wilson, R. W.; Hampsey, J.; Mani, T. Spin-allowed transitions control the formation of triplet excited states in orthogonal donor-acceptor dyads. *Chem* **2019,** *5* (1), 138-155.

23. Kuno, S.; Akeno, H.; Ohtani, H.; Yuasa, H. Visible room-temperature phosphorescence of pure organic crystals via a radical-ion-pair mechanism. *Phys. Chem. Chem. Phys.* **2015,** *17* (24), 15989-95.

24. Penfold, T. J.; Gindensperger, E.; Daniel, C.; Marian, C. M. Spin-vibronic mechanism for intersystem crossing. *Chem Rev* **2018,** *118* (15), 6975-7025.

25. Etherington, M. K.; Gibson, J.; Higginbotham, H. F.; Penfold, T. J.; Monkman, A. P. Revealing the spin-vibronic coupling mechanism of thermally activated delayed fluorescence. *Nat Commun* **2016,** *7*, 13680.

26. Yang, L.; Wang, X.; Zhang, G.; Chen, X.; Zhang, G.; Jiang, J. Aggregation-induced intersystem crossing: A novel strategy for efficient molecular phosphorescence. *Nanoscale* **2016,** *8* (40), 17422-17426.

27. de Souza, B.; Farias, G.; Neese, F.; Izsak, R. Predicting phosphorescence rates of light organic molecules using time-dependent density functional theory and the path integral approach to dynamics. *J. Chem. Theory Comput.* **2019,** *15* (3), 1896-1904.

28. Aidas, K.; Angeli, C.; Bak, K. L.; Bakken, V.; Bast, R.; Boman, L.; Christiansen, O.; Cimiraglia, R.; Coriani, S.; Dahle, P.; Dalskov, E. K.; Ekstrom, U.; Enevoldsen, T.; Eriksen, J. J.; Ettenhuber, P.; Fernandez, B.; Ferrighi, L.; Fliegl, H.; Frediani, L.; Hald, K.; Halkier, A.; Hattig, C.; Heiberg, H.; Helgaker, T.; Hennum, A. C.; Hettema, H.; Hjertenaes, E.; Host, S.; Hoyvik, I. M.; Iozzi, M. F.; Jansik, B.; Jensen, H. J.; Jonsson, D.; Jorgensen, P.; Kauczor, J.; Kirpekar, S.; Kjaergaard, T.; Klopper, W.; Knecht, S.; Kobayashi, R.; Koch, H.; Kongsted, J.; Krapp, A.; Kristensen, K.; Ligabue, A.; Lutnaes, O. B.; Melo, J. I.; Mikkelsen, K. V.; Myhre, R. H.; Neiss, C.; Nielsen, C. B.; Norman, P.; Olsen, J.; Olsen, J. M.; Osted, A.; Packer, M. J.; Pawlowski, F.; Pedersen, T. B.; Provasi, P. F.; Reine, S.; Rinkevicius, Z.; Ruden, T. A.; Ruud, K.; Rybkin, V. V.; Salek, P.; Samson, C. C.; de Meras, A. S.; Saue, T.; Sauer, S. P.; Schimmelpfennig, B.; Sneskov, K.; Steindal, A. H.; Sylvester-Hvid, K. O.; Taylor, P. R.; Teale, A. M.; Tellgren, E. I.; Tew, D. P.; Thorvaldsen, A. J.; Thogersen, L.; Vahtras, O.; Watson, M. A.; Wilson, D. J.; Ziolkowski, M.; Agren, H. The dalton quantum chemistry program system. *Wiley Interdiscip Rev Comput Mol Sci* **2014,** *4* (3), 269-284.